



저작자표시-비영리-변경금지 2.0 대한민국

이용자는 아래의 조건을 따르는 경우에 한하여 자유롭게

- 이 저작물을 복제, 배포, 전송, 전시, 공연 및 방송할 수 있습니다.

다음과 같은 조건을 따라야 합니다:



저작자표시. 귀하는 원저작자를 표시하여야 합니다.



비영리. 귀하는 이 저작물을 영리 목적으로 이용할 수 없습니다.



변경금지. 귀하는 이 저작물을 개작, 변형 또는 가공할 수 없습니다.

- 귀하는, 이 저작물의 재이용이나 배포의 경우, 이 저작물에 적용된 이용허락조건을 명확하게 나타내어야 합니다.
- 저작권자로부터 별도의 허가를 받으면 이러한 조건들은 적용되지 않습니다.

저작권법에 따른 이용자의 권리는 위의 내용에 의하여 영향을 받지 않습니다.

이것은 [이용허락규약\(Legal Code\)](#)을 이해하기 쉽게 요약한 것입니다.

[Disclaimer](#)

**Ph.D. DISSERTATION**

**Growth and characteristics of Ru based electrodes  
using RuO<sub>4</sub> precursor for DRAM capacitor**

by

**Cheol Hyun An**

**August 2019**

**DEPARTMENT OF MATERIALS SCIENCE AND ENGINEERING**

**COLLEGE OF ENGINEERING**

**SEOUL NATIONAL UNIVERSITY**

# **Growth and characteristics of Ru based electrodes using RuO<sub>4</sub> precursor for DRAM capacitor**

Advisor : Prof. Cheol Seong Hwang

by

Cheol Hyun An

A thesis submitted to the Graduate Faculty of Seoul National  
University in partial fulfillment of the requirements for the  
Degree of Doctor of Philosophy  
Department of Materials Science and Engineering

August 2019

Approved

by

Chairman of Advisory Committee : Ho Won Jang

Vice-chairman of Advisory Committee : Cheol Seong Hwang

Advisory Committee : Sang Bum Kim

Advisory Committee : Jeong Hwan Han

Advisory Committee : Woojin Jeon

## Abstract

---

Recently, scaling of the Dynamic Random Access Memory (DRAM) device, which is widely used in almost microelectronic fields, has been progressing. Thus, the further scaling of the capacitor in DRAM is also required for next generation DRAM device. However, a certain amount of capacitance,  $\sim 25\text{fF}$ , should be maintained to operate DRAM device but it is so challenging due to decreasing capacitance area and limit of patterning technology. Therefore, the improvement of performance via the introduction of new materials.

In recent studies, improving electrical performance using high-k materials such as  $\text{TiO}_2$  or  $\text{SrTiO}_3$  has been reported instead of  $\text{HfO}_2$  or  $\text{ZrO}_2$  based materials. The equivalent oxide thickness (EOT) could be lowered via introducing high-k materials, but adequate electrode should be selected to enhance the crystallinity of dielectric film and lower the leakage current following the low band gap energy.

Kinds of noble metal based materials such as Ru, Ir, Pt having been spotlighted as electrode materials of next generation DRAM capacitor. Among them, Ru has high work function ( $\sim 4.7\text{eV}$ ), low resistivity ( $\sim 7$

uohm-cm), high chemical stability so that many studies on Ru metal film are reported. Almost Ru thin film deposition methods use metal-organic precursors having large ligand size, low vapor pressure, and reactivity which make it difficult to adopt on DRAM capacitor devices.

In this study, therefore, growing Ru-based thin films and investigating the electrical performance of capacitors using RuO<sub>4</sub> precursor, which has high reactivity and vapor pressure, are reported. Depositing methods of Ru, RuO<sub>2</sub>, or SrRuO<sub>3</sub> materials using RuO<sub>4</sub> precursor have been reported but those are based on CVD reaction. Thus, the ALD growth of Ru based films is investigated to achieve better conformality.

Firstly, ALD of Ru metal films using RuO<sub>4</sub> precursor and reduction gas has been investigated. To prevent the thermal decomposition of RuO<sub>4</sub> precursor, the deposition was conducted at a lower temperature range than the previously reported CVD process. Ru metal films were grown on various oxide substrates, Ta<sub>2</sub>O<sub>5</sub>, ZrO<sub>2</sub>, and TiO<sub>2</sub>. On ZrO<sub>2</sub> and TiO<sub>2</sub> substrate, ordinary ALD-like growth behavior of Ru metal films was shown while unexpected growth behavior was shown on Ta<sub>2</sub>O<sub>5</sub> substrate. The deposition amount of Ru metal film showed 2 self-limited steps versus reduction gas feeding time, which was not reported before. From the physical and chemical analysis of the film in each step, only

pure Ru metal was deposited and any introduction of different phase like RuO<sub>2</sub> was not present. Through the detailed analysis, the mechanism based on the reduction and diffusion of Ta<sub>2</sub>O<sub>5</sub> substrate material was proposed to explain the extraordinary growth behavior. Despite its abnormal growth behavior, grown Ru films have low resistivity, low impurity and high step coverage. On ZrO<sub>2</sub> and TiO<sub>2</sub> surface, Ru metal film has good performance as on Ta<sub>2</sub>O<sub>5</sub> surface.

The high work function of Ru metal is expected to suppress the leakage current of high-k dielectric films, the improvement of electric characteristics of the capacitor with Ru top electrode was investigated. ZrO<sub>2</sub>/Al<sub>2</sub>O<sub>3</sub>/ZrO<sub>2</sub> (ZAZ) and TiN were used as dielectric film and a bottom electrode, respectively. Sputter-grown TiN top electrode was used for comparison. Since Ru top electrode was deposited via the ALD process, the patterning process of Ru film is required. The Ru metal films were oxidized to RuO<sub>4</sub> and etched, using O<sub>3</sub> gas in ALD chamber. Comparing the electric characteristics of the Ru/ZAZ/TiN capacitor and TiN/ZAZ/TiN capacitor, the leakage current issue was significantly improved. The physical thickness of ZAZ film could be reduced due to lowered leakage current so that the EOT of Ru/ZAZ/TiN capacitor shrank to 75% of TiN/ZAZ/TiN capacitor, at the leakage current level of DRAM capacitor, 10<sup>-7</sup> A/cm<sup>2</sup>. From the detailed analysis of leakage conduction mechanisms, it could be demonstrated that not only the high

work function of Ru metal but also the patterning process affected the improvement of leakage current issue. During the Ru top electrode patterning process, the introduced O<sub>3</sub> gas recovered the oxygen vacancies in ZAZ dielectric film and the charge conduction was suppressed.

Finally, the modified SrRuO<sub>3</sub> deposition process for improving step coverage is studied. The previous SrRuO<sub>3</sub> deposition process consists of ALD SrO cycles and CVD RuO<sub>2</sub> cycles. SrO layers show excessive growth behavior so that the step coverage is not that good in conventional process. Thus, to prevent the oxygen absorption from RuO<sub>2</sub> layer which induces the excessive growth of SrO layer, the reduction gas injection step is introduced after the RuO<sub>2</sub> deposition step. From the modified deposition process, SrRuO<sub>3</sub> layer shows step coverage about 95% on hole structure with 10:1 aspect ratio without any characteristic deterioration. Moreover, the surface roughness of SrRuO<sub>3</sub> film in modified process is also significantly improved.

---

**Keywords:** Ruthenium, Ruthenium tetroxide, Strontium Ruthenate, Dynamic

Random Access Memory, Atomic Layer Deposition, capacitor

**Student Number:** 2013-22478

Cheol Hyun An

# Table of Contents

---

|  |           |
|--|-----------|
| Abstract .....   | iii       |
| Table of Contents .....  | vii       |
| List of Figures .....  | x         |
| List of Abbreviations .....  | xix       |
| <b>1. Introduction .....</b>   | <b>1</b>  |
| 1.1. Overview and Issues on DRAM Materials .....   | 1         |
| 1.2. Atomic Layer Deposition for DRAM Capacitor.....   | 7         |
| 1.3. Growth of Ru-based Materials for DRAM Capacitor.....  | 11        |
| 1.4. Bibliography .....  | 22        |
| <b>2. Atomic Layer Deposition of Ru thin films using RuO<sub>4</sub><br/>Precursor and Substrate Effect on Growth<br/>Behavior .....</b> | <b>24</b> |
| 2.1. Introduction.....   | 24        |
| 2.2. Experimental .....  | 30        |
| 2.3. Results and Discussions.....  | 32        |
| 2.4. Summary .....   | 66        |

|   |            |
|---|------------|
| 2.5. Bibliography .....   | 68         |
| <b>3. Improving Electrical Performance of ZAZ/TiN based MIM capacitor adopting ALD-grown Ru Top Electrode .....</b> | <b>76</b>  |
| 2.1. Introduction.....  | 76         |
| 3.2. Experimental .....   | 80         |
| 3.3. Results and Discussions.....   | 84         |
| 3.4. Summary .....  | 101        |
| 3.5. Bibliography .....   | 103        |
| <b>4. Improving conformality of SrRuO<sub>3</sub> thin films via controlling CVD-like growth behavior.....</b>      | <b>107</b> |
| 4.1. Introduction.....  | 107        |
| 4.2. Experimentals .....  | 109        |
| 4.3. Results and Discussions.....   | 111        |
| 4.4. Summary .....  | 129        |
| 4.5. Bibliography .....   | 131        |
| <b>5. Conclusion.....</b>   | <b>133</b> |
| <b>Curriculum Vitae.....</b>  | <b>135</b> |
| <b>List of publications .....</b>   | <b>139</b> |

|                                   |            |
|-----------------------------------|------------|
| <b>Abstract (in Korean) .....</b> | <b>155</b> |
|-----------------------------------|------------|

# List of Figures

---

|  |    |
|--|----|
| Figure 1.1 Scheme of the DRAM cell structure.....  | 2  |
| Figure 1.2 Development of the dielectric materials for DRAM capacitor .....  | 5  |
| Figure 1.3 Scheme of the ALD process cycle .....   | 9  |
| Figure 1.4 Pulsed CVD growth of Ru film using RuO <sub>4</sub> precursor on various<br>substrates.....   | 13 |
| Figure 1.5 The SIMS depth profile of Ru films grown via ALD with DER<br>precursor and p-CVD with RuO <sub>4</sub> precursor.....                       | 13 |
| Figure 1.6 Growth of RuO <sub>2</sub> and Ru phases at different N <sub>2</sub> /H <sub>2</sub> feeding time ..  | 16 |
| Figure 1.7 Step coverage of RuO <sub>2</sub> films on hole structure of 10:1 aspect ratio<br>.....   | 16 |
| Figure 1.8 Improved leakage current characteristic of TiO <sub>2</sub> dielectric films<br>adopting RuO <sub>2</sub> electrode than Ru electrode. .... | 18 |
| Figure 1.9 Growth behavior of SrRuO <sub>3</sub> film via ALD/CVD combing deposition<br>method.....  | 20 |
| Figure 1.10 In-situ crystallization and dielectric property of SrTiO <sub>3</sub> dielectric   |    |

on SrRuO<sub>3</sub> electrode..... 21

Figure 2.1 (a) Growth behavior of the Ru films on a Ta<sub>2</sub>O<sub>5</sub> substrate as a function of the RuO<sub>4</sub> precursor injection time at 140, 165, and 200 °C. (b) Variation in the Ru areal density of the Ru films on the Ta<sub>2</sub>O<sub>5</sub>/Si substrate as a function of the deposition temperature. Inset figure (b) shows the Arrhenius plot of the variations of Ln (Ru areal density) as a function of the reciprocal deposition temperature..... 34

Figure 2.2 Ru 3d XP spectra of the Ru films grown on a Ta<sub>2</sub>O<sub>5</sub>/Si substrate at 140 °C..... 34

Figure 2.3 Variations of the Ru areal density on the Ta<sub>2</sub>O<sub>5</sub>/Si substrate grown at 165 °C as a function of the time per ALD pulse: (a) N<sub>2</sub>/H<sub>2</sub> mixed-gas injection time; (b) N<sub>2</sub>/H<sub>2</sub> gas purge time; (c) RuO<sub>4</sub> precursor injection time; and (d) RuO<sub>4</sub> precursor purge time. . . . . 36

Figure 2.4 (a) XRD patterns in glancing angle mode of the films grown on a Ta<sub>2</sub>O<sub>5</sub>/Si substrate with different N<sub>2</sub>/H<sub>2</sub> gas injection times: the 18 nm film in step S and the 12 nm film in step L. Inset figure (a)

shows the XRD patterns in  $\theta$ - $2\theta$  mode of the films, and figures (b) and (c) show the measured XRR curve and the fitted curve of the 18 nm Ru film in step S and the 12 nm Ru film in step L, respectively..... 39

Figure 2.5 (a) Ru 3d XP spectra of the Ru films grown on a Ta<sub>2</sub>O<sub>5</sub>/Si substrate with different N<sub>2</sub>/H<sub>2</sub> gas injection times. (b) Deconvoluted peaks of the Ru 3d XP spectra of the Ru film grown in step S. (c)-(d) SIMS depth profile of the Ru films grown on a Ta<sub>2</sub>O<sub>5</sub>/Si substrate in steps S and L, respectively.. ..... 43

Figure 2.6 O 1s XP spectra of the Ru films grown a Ta<sub>2</sub>O<sub>5</sub>/Si substrate with different N<sub>2</sub>/H<sub>2</sub> gas injection times..... 44

Figure 2.7 (a)-(b) SIMS depth profile of the Ru films grown on a Ta<sub>2</sub>O<sub>5</sub>/Si substrate in steps S and L, respectively. Ti passivation layers were deposited on each Ru film..... 44

Figure 2.8 Ta 4f XP spectra of the pristine Ta<sub>2</sub>O<sub>5</sub>/Si substrate..... 48

Figure 2.9 Ta 4f XP spectra of the Ru films grown on the same substrate with different N<sub>2</sub>/H<sub>2</sub> gas injection times and thicknesses: (a) 2.7 nm-

thick Ru film in step S without surface cleaning; (b) 3.5 nm-thick Ru film in step L without surface cleaning; (c) 15 nm-thick Ru film in step S without surface cleaning; (d) 15 nm-thick Ru film in step L without surface cleaning; (e) 15 nm-thick Ru film in step S after 3 nm etching; and (f) 15 nm-thick Ru film in step L after 3 nm etching..... 49

Figure 2.10 (a) Variations of the Ru areal density of the films grown on an Au substrate as a function of the  $N_2/H_2$  gas injection time. (b) Variations of the Ru areal density on the films grown on a  $Ta_2O_5/Si$  or Au substrate as a function of the number of ALD cycles..... 52

Figure 2.11 (a) Variation of the water droplet contact angle on the  $Ta_2O_5$  substrate as a function of  $N_2/H_2$  injection time; (b) the contact angle image of pristine  $Ta_2O_5$  substrate; (c) the contact angle image of  $Ta_2O_5$  substrate with 15s of  $N_2/H_2$  feeding; (d) the contact angle image of  $Ta_2O_5$  substrate with 25s of  $N_2/H_2$  feeding..... 57

Figure 2.12 Schematic diagram of the initial growth stage in (a) step S and (b) step L..... 59

Figure 2.13 (a) Variations of the reciprocal sheet resistance of the Ru films grown on a Ta<sub>2</sub>O<sub>5</sub>/Si substrate with different N<sub>2</sub>/H<sub>2</sub> gas injection times as a function of the film thickness. (b) RMS roughness of the Ru films grown on a Ta<sub>2</sub>O<sub>5</sub>/Si substrate with different N<sub>2</sub>/H<sub>2</sub> gas injection times, and the variations after annealing at 400-800 °C. Inset figure (b) shows the surface AFM images of the as-deposited and 800 °C-annealed Ru films grown in step S. (c) Cross-sectional TEM image of the Ru film grown on a ZrO<sub>2</sub>/TiN hole structure with a long N<sub>2</sub>/H<sub>2</sub> gas injection time (opening diameter: ~100 nm; aspect ratio: ~20:1). (d) Enlarged image of (c), where ZrO<sub>2</sub>/TiN layers were grown by ALD. .... 65

Figure 3.1 Scheme of the TE fabrication process: (a) TiN electrode; and (b) Ru electrode. .... 83

Figure 3.2 (a) Variations in  $J$  as a function of  $t_{ox}$  at a +0.8 V applied voltage. The solid lines were added for eye guidance. (b)  $J$ - $E$  characteristics of the MIM capacitors with different TEs. (inset)  $J$ - $E$  characteristics of the MIM capacitors with (opened) Pt TE and

(closed) Pt TE and employing O<sub>3</sub> treatment..... 87

Figure 3.3 (a, b) Temperature dependence of the  $J$ - $V$  characteristics of the MIM capacitors with TiN TE at (a) positive and (b) negative biases. (c, d) Replotted plots from (c) figure 3a and (d) figure 3b according to the equation (2) for calculating the trap depth ( $\phi_0$ ) and the optical dielectric constant ( $\epsilon_\infty$ ) in the Poole-Frenkel emission. (e) Temperature dependence of the  $J$ - $V$  characteristic of the MIM capacitors with Ru TE at positive bias. (f) Transformed  $J$ - $V$  data in (e) for fitting to Fowler-Nordheim tunneling mechanism... 91

Figure 3.4  $C/C_0$ - $V$  characteristics of the MIM capacitors with different TEs at 10 kHz..... 95

Figure 3.5 (a-d) Zr 3d angle-resolved XP spectra of the as-deposited (black) and O<sub>3</sub>-treated (red) Pt/Ru/ZAZ/TiN at different emission angle (a) 0°, (b) 30°, (c) 45° and (d) 60°. Deconvoluted peaks of the Zr 3d XP spectra of the (e) as-deposited Pt/Ru/ZAZ/TiN sample and (f) O<sub>3</sub>-treated Pt/Ru/ZAZ/TiN sample at 0° emission angle..... 98

Figure 3.6 Ti 2p XP spectra of the as-deposited (black square) and O<sub>3</sub>-treated

|  |     |
|--|-----|
| (red dot) Pt/Ru/ZAZ/TiN sample at 0° emission angle.....   | 100 |
| Figure 4.1 The deposition sequence of SrRuO <sub>3</sub> films in (a) original recipe (b)                    |     |
| N <sub>2</sub> /H <sub>2</sub> injected (modified) recipe.....   | 110 |
| Figure 4.2 Variation of SrO areal density in SRO films as a function of N <sub>2</sub> /H <sub>2</sub>       |     |
| gas injection time.....  | 112 |
| Figure 4.3 Variations of the SrO areal density in SRO films without or with                                  |     |
| N <sub>2</sub> /H <sub>2</sub> gas as a function of varying SrO:RuO <sub>2</sub> sub-cycle ratio. .          | 112 |
| Figure 4.4 The SIMS depth profile of SRO films grown on RuO <sub>2</sub> /Ta <sub>2</sub> O <sub>5</sub> /Si |     |
| substrate using (a) original recipe without H <sub>2</sub> (b) modified recipe                               |     |
| with H <sub>2</sub> .....  | 114 |
| Figure 4.5 The GAXRD patterns of SRO films grown on RuO <sub>2</sub> substrate using                         |     |
| recipes without or with H <sub>2</sub> , in as-deposited state and annealed state                            |     |
| .....  | 116 |
| Figure 4.6 The cross-sectional SEM images of SRO films grown on trench hole                                  |     |
| structure using (a) original recipe without H <sub>2</sub> (b) modified recipe                               |     |
| with H <sub>2</sub> . The aspect ratio and opening size of hole structure were                               |     |
| 10:1 and 100 nm, respectively.....   | 118 |

Figure 4.7 The plane view SEM images and the distribution of grain sizes of SRO films grown on RuO<sub>2</sub> substrate using (a) original recipe without H<sub>2</sub> (b) modified recipe with H<sub>2</sub>. ..... 119

Figure 4.8 (a) The XP spectra of Ru 3d orbital of as-deposited SRO films grown by both recipes. (b) Peak deconvolution of XP spectra in (a). (c) The XP spectra of Ru 3d orbital of annealed SRO films grown by both recipes. (d) Peak deconvolution of XP spectra in (c). . 121

Figure 4.9 The XP spectra of Sr 3d orbital and peak deconvolution of (a) as-deposited SRO film grown by original recipe without H<sub>2</sub> (b) as-deposited SRO film grown by modified recipe with H<sub>2</sub> (c) annealed SRO film grown by original recipe without H<sub>2</sub> (d) annealed SRO film grown by modified recipe with H<sub>2</sub>. ..... 123

Figure 4.10 Variation of the Sr cation composition in SRO films as a function of SrO:RuO<sub>2</sub> sub-cycle ratio. Inset figures showed the variation of SrO and Ru areal densities as a function of sub-cycle ratio. .... 125

Figure 5.11 Variation of the RMS roughness of SRO films grown on Pt substrate as a function of the number of SRO supercycles. The inset figure

showed the AFM image of the 2-supercycle SRO film grown on Pt substrate..... 125

Figure 4.12 (a) The GAXRD patterns of SRO films grown on Pt substrate, in as-deposited and annealed at 600 °C or 700 °C. (b) The AFM image of the 15 nm-SRO/Pt annealed at 700 °C. .... 126

Figure 4.13 The GAXRD patterns of as-deposited STO on SRO/Pt bimetal electrodes. The thickness of SRO layer varied from 0 nm to 3 nm.. ..... 126

Figure 4.14 Variation of the difference of work function with only Pt substrate as a function of SRO thickness on Pt substrate. .... 128

## List of Abbreviations

---

|      |                                  |
|------|----------------------------------|
| DRAM | Dynamic Random Access Memory     |
| EOT  | Equivalent Oxide Thickness       |
| ALD  | Atomic Layer Deposition          |
| CVD  | Chemical Vapor Deposition        |
| SRO  | SrRuO <sub>3</sub>               |
| STO  | SrTiO <sub>3</sub>               |
| XRD  | X-Ray Diffraction                |
| XRR  | X-Ray Reflectivity               |
| AFM  | Atomic Force Microscope          |
| XPS  | X-ray Photoelectron Spectroscopy |
| SIMS | Secondary Ion Mass Spectroscopy  |
| SEM  | Scanning Electron Microscope     |
| TEM  | Transmission Electron Microscope |
| PDA  | Post Deposition Annealing        |
| PMA  | Post Metallization Annealing     |
| TE   | Top Electrode                    |
| 4pp  | 4 point-probe                    |
| AES  | Auger Electron Spectroscopy      |

# **1. Introduction**

## **1.1. Overview and Issue on DRAM Materials**

Dynamic Random Access Memory (DRAM) is a kind of semiconductor devices consisting of one transistor and one capacitor. It is widely used in microelectronics such as PC, mobiles, servers, graphic cards, etc. The capacitor in DRAM device acts as charge storage, and “1” is written when charge is stored while “0” is written if charge is not stored. The transistor has a role as switch controlling charge from to or from capacitor in reading or writing operation.

DRAM device has advantage of scalability, high reliability and high endurance, but its volatility is challenging for further scaling of capacitor. During the operation of DRAM devices, the stored charge losses continuously so that the periodical refresh (rewrite) of data is inevitable.

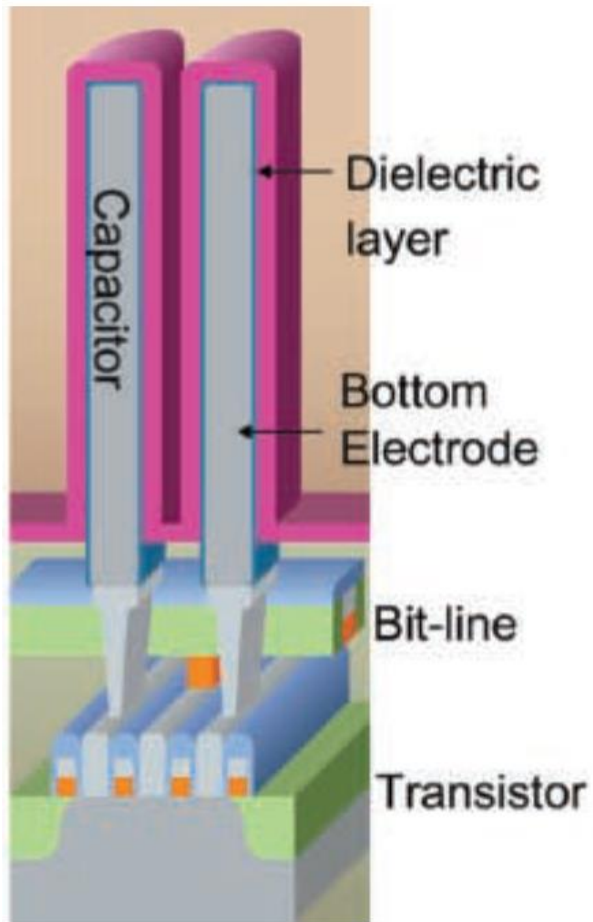


Figure 1.1 Scheme of the DRAM cell structure

Moreover, the scaling of DRAM devices is progressing so that the size of DRAM capacitor also is required to shrink. Although the size of capacitor becomes smaller, certain level of capacitance ( $\sim 25\text{fF}$ ) is required to be detected in sense amplifier comparing with capacitance of bit line<sup>[1]</sup>. The capacitance is described as below equation (1).

$$C = \epsilon_0 \epsilon_r \frac{A}{t}$$

Each symbols,  $\epsilon_0$ ,  $\epsilon_r$ ,  $A$ ,  $t$  is vacuum permittivity, dielectric constant, capacitance area, and dielectric film thickness, respectively. As the scaling of capacitor is progressing, the dielectric film should be thinner. However, the patterning process containing lithography or etching has reached to limit so that the height of capacitor cannot be increased anymore. Therefore, alternating the capacitor material to higher-k dielectric film is required, and several studies on promising materials have been reported.

In conventional DRAM devices,  $\text{ZrO}_2$ -based dielectric films which dielectric constant is about 40 is used as capacitor dielectric material<sup>[2,3]</sup>. To improve the performance of capacitor devices, dielectric films having higher dielectric constant such as  $\text{TiO}_2$  or  $\text{SrTiO}_3$  is required and having been studied<sup>[1,4-6]</sup>.  $\text{TiO}_2$ , which has different dielectric constant with crystalline structure, has high dielectric constant about 80 in rutile phase if it is grown on adequate bottom substrate.  $\text{SrTiO}_3$ , perovskite-structured material, has such higher dielectric constant about 300. The higher dielectric constant of these materials is expected

to enable further scaling of capacitor devices, but their low band gap energy around 3 eV also could be problematic for leakage current issue.

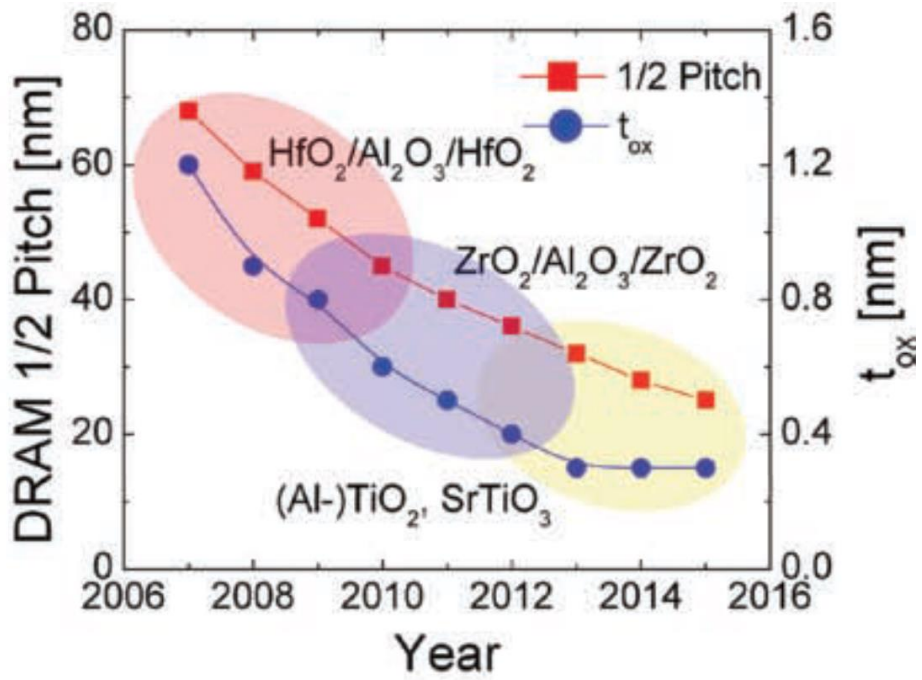


Figure 1.2 Development of the dielectric materials for DRAM capacitor<sup>[4]</sup>

Therefore, alternating electrode material not only dielectric material is also inevitable to improve the performance of capacitor. The electrode material in conventional capacitor is TiN, which has work function of 4.2 eV. It is suitable for electrode material in ZrO<sub>2</sub>-based capacitor, however, another electrode material which could suppress leakage current is required for higher-k film such as TiO<sub>2</sub> or STO. Among several noble metal-based candidates, Ru-based electrode materials are mostly promising. Ru metal has high work function of 4.7eV, low resistivity of 7 uohm-cm, and high chemical stability. Moreover, Ru metal has high oxidation resistivity so it would not be oxidized in following processes. If Ru metal is oxidized to RuO<sub>2</sub> phase, the RuO<sub>2</sub> is also conductive oxide and has higher work function of 5.0 eV, so that deterioration of capacitor performance via oxidation is not of interest. Ru metal could act as seed layer of in-situ crystallization of TiO<sub>2</sub> dielectric film into rutile phase.

SrRuO<sub>3</sub>, a kind of Ru-based materials, is also a candidate of next-generation electrode material. SRO has relatively high resistivity but it has significantly high work function about 5.2 eV. In fact, it is also perovskite-structured material like STO, and its lattice parameter is almost same with that of STO so that SRO could be seed layer for in-situ crystallization of STO dielectric film. Therefore, the development of SRO electrode is essential to adopt STO on DRAM capacitor devices.

## 1.2. Atomic Layer Deposition for DRAM Capacitor

The objective of this dissertation is to study on the NC phenomena in DE/FE bi-layer structures through both theoretical and experimental approaches.

As mentioned in previous section, aspect ratio of capacitor is significantly increased and its feature size shrinks lower than 20 nm as size of DRAM devices becomes smaller. To deposit very thin, conformal dielectric and electrode film about few nm on capacitor, growing films via ALD process is inevitable. Therefore, not only proper selection of materials, also ALD-based deposition methods are being studied to enhance the performance of DRAM capacitor devices<sup>[7]</sup>.

ALD is a thin film-depositing method which repeating cycles consisting of sequential feeding and purging of precursor and reaction gas. The conformal film growth and precise thickness controlling can be achieved from the characteristic self-limited growth behavior of ALD method. In detail, at precursor feeding step, injected precursors are adsorbed on the surface chemically and physical adsorption is followed onto other precursors. At precursor purging step, physically adsorbed precursors are blown out from the surface by inert gas and only chemically adsorbed precursors remained on surface. Since the adsorption site of surface is limited, the amount of chemically adsorbed precursors is kept constantly so that the self-limited growth behavior is shown. At following reaction gas feeding step, the ligands in precursors react

with reaction gas and removed, and the byproducts are blown out at purging step.

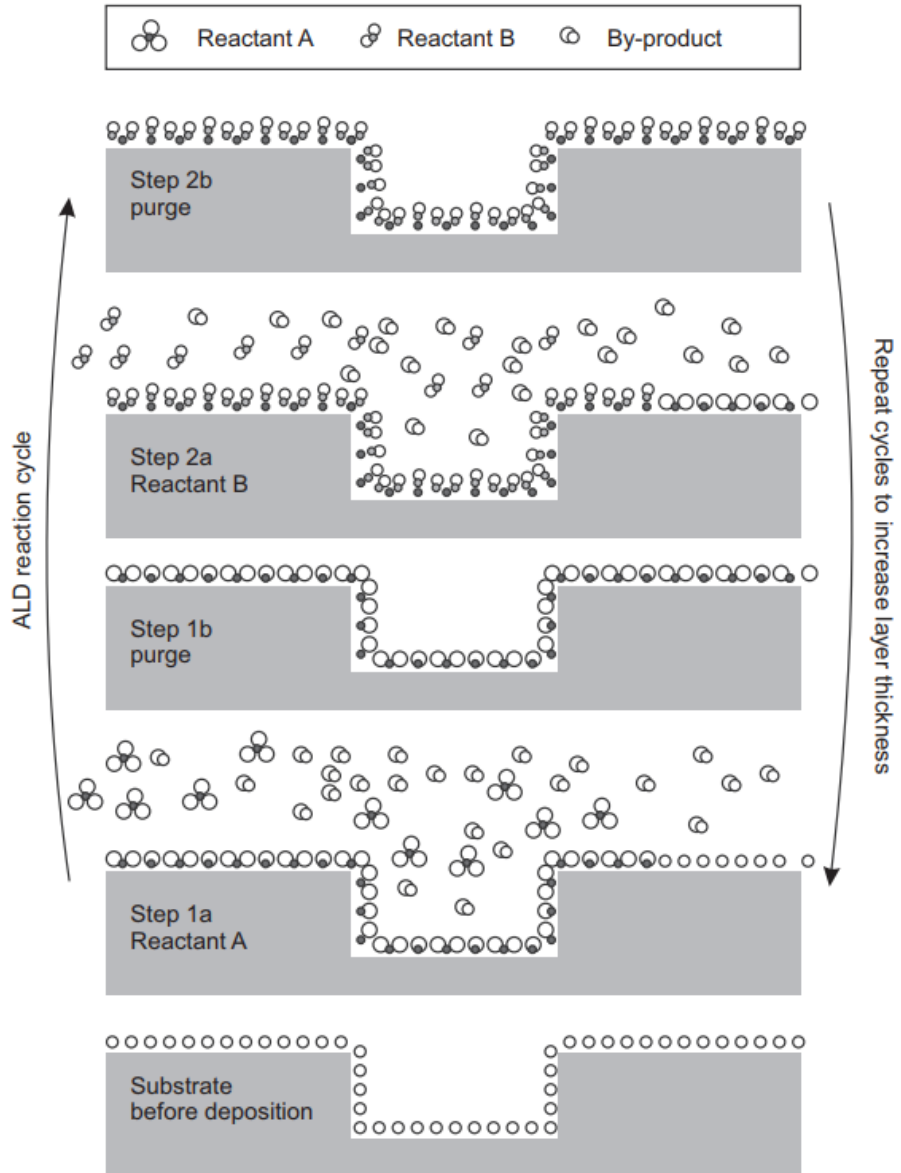


Figure 1.3 Scheme of the ALD process cycle<sup>[8]</sup>

ALD process could be adopted for fabrication of various materials, such as metals, oxides, nitrides, even sulfides. In addition, the process window of ALD varies depending on precursors and reactants so that it can have very wide range of process temperature.

The characteristic self-limited growth behavior of ALD process has temperature window, varying with precursor and reactant. At higher temperature, the precursor is thermally decomposed so that the growth rate increases. Otherwise, at lower temperature, the chemical reaction of ligands in precursor and reactant is inactive so that the growth rate decreases. Thus, the appropriate temperature range is required to adopt ALD process. Moreover, ALD process has substrate dependency since it is based on chemical reaction, and growth rate of one monolayer per one cycle is too slow so that it has disadvantages in economical aspect.

Although ALD process has aforementioned disadvantages, it is essential to deposit films on devices having small feature size and high aspect ratio. The low growth rate is not such problematic since only few nm of films would be deposited via ALD process.

### 1.3. Growth of Ru-based Materials for DRAM Capacitor

In recent papers, the growth behavior of Ru-based electrode materials has been reported by authors. Almost studies used the Metal-Organic precursors such as Ru(EtCp)<sub>2</sub>, RuCp<sub>2</sub>, etc, for Ru film growth<sup>[9-11]</sup>. In that studies, pure Ru film could be grown but the reactivity of precursors are that high, so that the growth rate is not high and tens of incubation cycle is shown. To improve the initial nucleation issue, the zero-valence Ru metal precursors has been investigated. Various kinds of ligands are used for zero-valence precursors and the improvement of inicial nucleation is enabled by those precursors. However, the ligands of zero-valence precursors are so bulky and complex so that it is not the preferred alternative till now.

Han et al., has reported the growth of Ru film via pulsed CVD method, using RuO<sub>4</sub> precursor which has high volatility and reactivity, very simple molecule structure<sup>[12]</sup>. The pulsed CVD means that the precursor and reactant are injected sequentially like ALD process, not simultaneously as conventional CVD process. In that study, pure Ru film was deposited on surface via thermal decomposition of RuO<sub>4</sub> precursor to RuO<sub>2</sub> and reduction to Ru metal by following N<sub>2</sub>/H<sub>2</sub> reductant. The p-CVD grown Ru metal film using RuO<sub>4</sub> has lower impurity concentration than ALD grown Ru metal film using 2,4-(dimethyl-pentadienyl)(ethylcyclopentadienyl)Ru (DER) precursor. Even though the RuO<sub>4</sub> precursor was thermally decomposed, it did not contain

carbon in ligands so that the carbon-free Ru metal film could be grown. Moreover, the initial incubation cycles were significantly decreased than other precursors. On TiN and Si substrate, only neglectable incubation cycles were observed, while just 20 incubation cycles were shown on SiO<sub>2</sub> substrate. In contrast, the DER precursor showed hundred of incubation cycles on SiO<sub>2</sub> substrate. The improved initial nucleation also enhanced the thermal stability of Ru film in higher temperature. Even though the Ru film growth was based on the CVD reaction, high step coverage of 90% was shown on 10:1 aspect ratio hole structure. It could be indicated that the high volatility of RuO<sub>4</sub> precursor enabled the conformal growth of Ru film on hole structure.

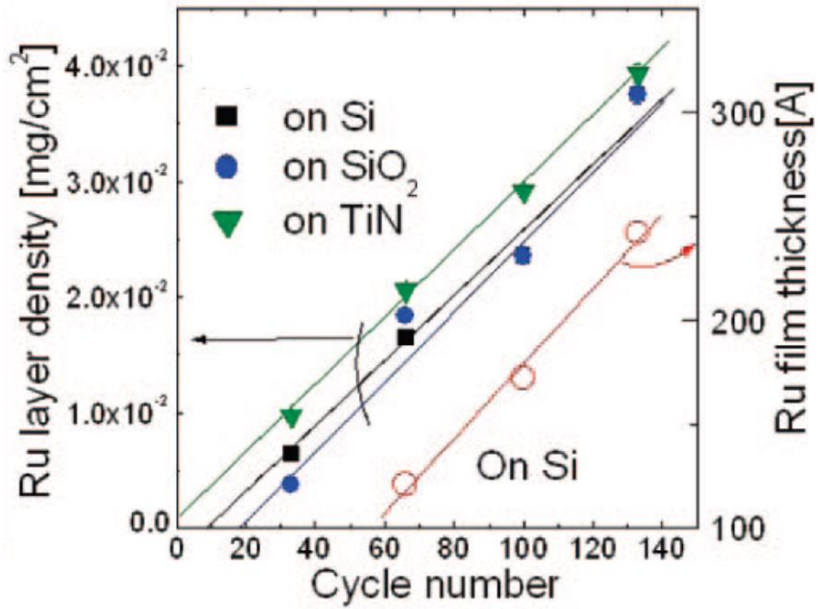


Figure 1.4 Pulsed CVD growth of Ru film using RuO<sub>4</sub> precursor on various substrates.<sup>[12]</sup>

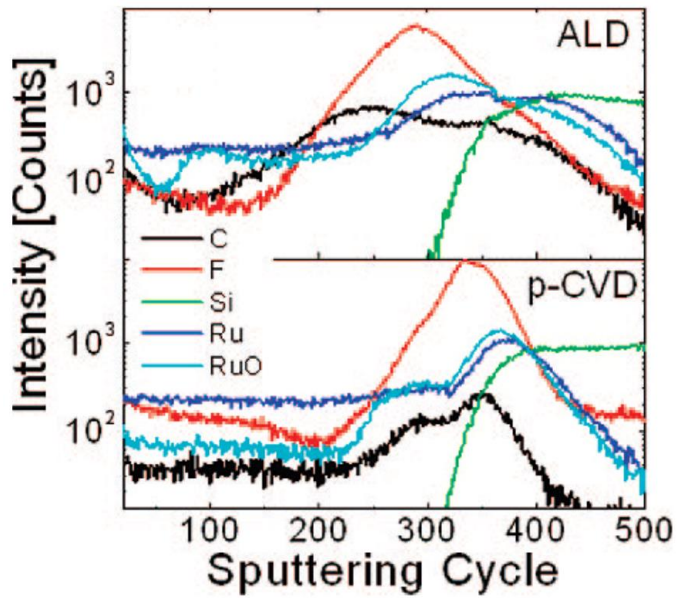


Figure 1.5 The SIMS depth profile of Ru films grown via ALD with DER precursor and p-CVD with RuO<sub>4</sub> precursor<sup>[12]</sup>

In pulsed CVD growth process of Ru metal film, the  $N_2/H_2$  gas had a very important role on the phase of film. Since the  $RuO_2$  film was firstly deposited and reduced in following steps, sufficiently long feeding time of  $N_2/H_2$  gas was required to deposit oxygen-free Ru metal film. Otherwise, the growth of  $RuO_2$  film via controlling  $N_2/H_2$  gas feeding time was also investigated by same authors<sup>[13]</sup>. In that study, rather than the simple trend that decomposed Ru precursors were reduced from  $RuO_2$  to Ru, specific growth behavior was observed. With increasing  $N_2/H_2$  injection time, the amount of deposited Ru atom increased and saturated in two stages. (Figure 1.6) The two plateau could be explained by the change of film change, from  $RuO_2$  to Ru. The phase of films in each stages was determined by the physical, electrical, and chemical analysis such as XRR, XRD, AES, 4pp, and XPS. The  $N_2/H_2$  reductant affected on not only the phase of film, but the growth behavior of films. During  $RuO_2$  film growth, the longer  $N_2/H_2$  gas injection enhanced the initial nucleation of  $RuO_2$  film on  $Ta_2O_5$  substrate.  $H_2$  played a critical role in enhancing the adsorption of  $RuO_4$  precursor on surface by forming hydroxyl group, which attracted the  $RuO_4$  molecule. The abrupt change of phase at certain  $N_2/H_2$  feeding time range was contributed from the self-catalytic effect and reverse-disproportionation reaction of Ru metal. If small amount of Ru metal was formed in  $RuO_2$  phase, it acted like catalyst and near  $RuO_2$  phase was fastly reduced to Ru phase. The pulsed CVD-grown  $RuO_2$  film showed higher step coverage than 90%, as the case of Ru metal film. It could be concluded that the

volatility of RuO<sub>4</sub> precursor was sufficiently high to deposit film on high aspect ratio structure.

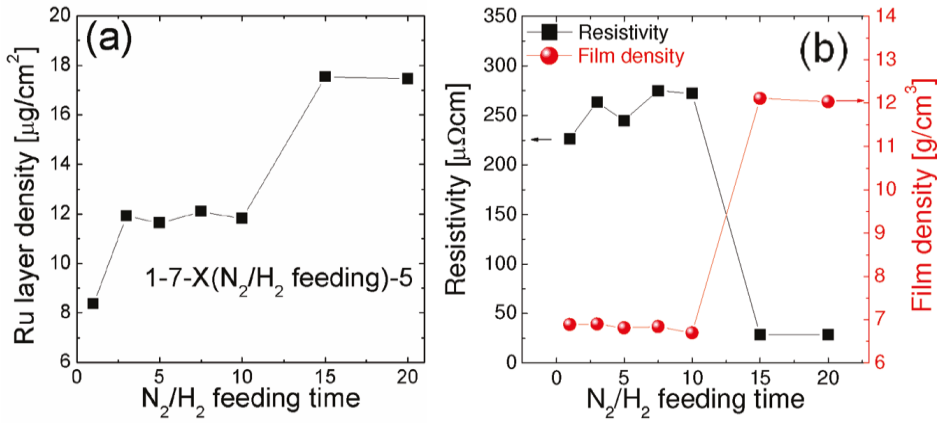


Figure 1.6 Growth of RuO<sub>2</sub> and Ru phases at different  $N_2/H_2$  feeding time<sup>[13]</sup>

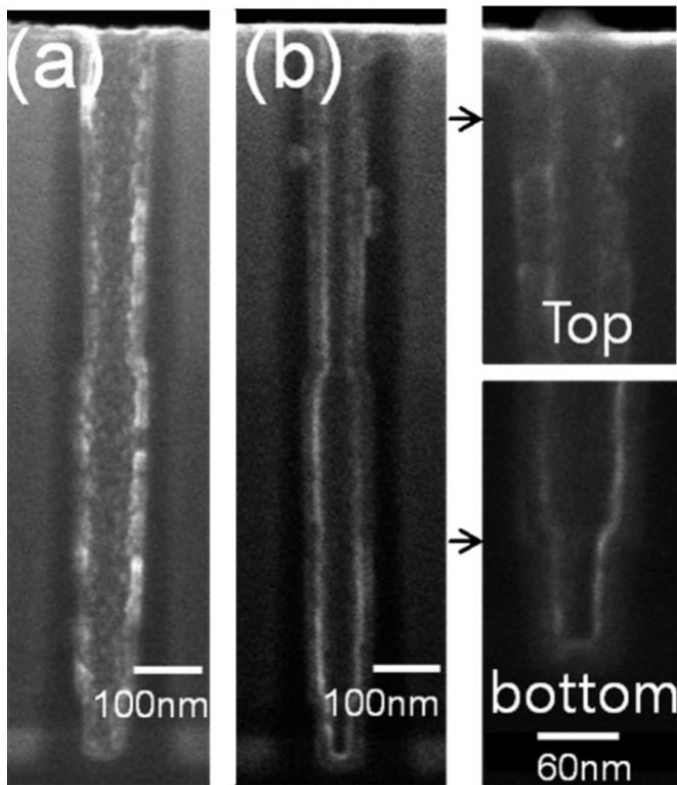


Figure 1.7 Step coverage of RuO<sub>2</sub> films on hole structure of 10:1 aspect ratio<sup>[13]</sup>

The RuO<sub>2</sub> film was adopted as bottom electrode of MIM capacitor with TiO<sub>2</sub> dielectric film<sup>[14]</sup>. Comparing with sputter-grown Ru bottom electrode, the leakage current was improved by adopting RuO<sub>2</sub> electrode. As on Ru electrode, TiO<sub>2</sub> and ATO films grown on RuO<sub>2</sub> electrode were also crystallized into rutile phase having lower leakage current. The minimum EOT of TiO<sub>2</sub>/RuO<sub>2</sub> capacitor was drastically improved than TiO<sub>2</sub>/Ru capacitor, from 0.8 nm to 0.56 nm. The origin of lowered leakage current was investigated by temperature dependency of I-V characteristics and XPS measurement. The high work function of RuO<sub>2</sub> increased the Schottky barrier height of TiO<sub>2</sub>/RuO<sub>2</sub> interface, 0.27 eV higher than TiO<sub>2</sub>/Ru interface.

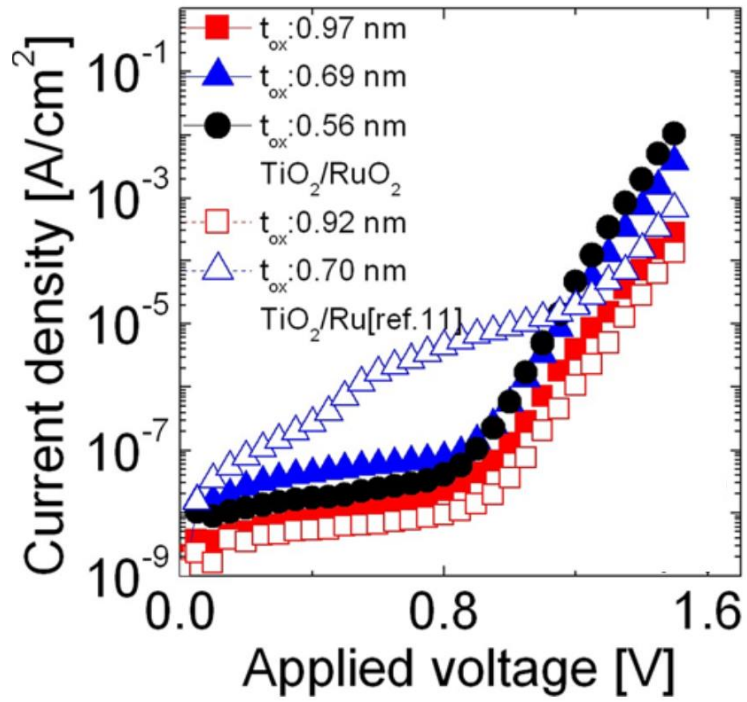


Figure 1.8 Improved leakage current characteristic of TiO<sub>2</sub> dielectric films adopting RuO<sub>2</sub> electrode than Ru electrode.<sup>[14]</sup>

SrRuO<sub>3</sub>, a kind of Ru-based electrode materials, also could be deposited by RuO<sub>4</sub> precursor<sup>[15]</sup>. The deposition process of SrRuO<sub>3</sub> film consisted of sequential ALD-grown SrO layers and CVD-grown RuO<sub>2</sub> layers. Sr(<sup>i</sup>Pr<sub>3</sub>Cp)<sub>2</sub> and O<sub>2</sub> were used as Sr precursor and oxidant for ALD process of SrO layer. In pulsed CVD process of RuO<sub>2</sub> layer, only RuO<sub>4</sub> precursor was used without any reactant gas. Although the SrO layer showed self-limited growth behavior on RuO<sub>2</sub> surface, the SrO layer showed enhanced growth rate in initial stage. The high growth rate in initial growth resulted from the oxygen-attracting nature of Sr precursor. During Sr precursor injection step, it absorbed the oxygen in RuO<sub>2</sub> layer and formed SrO layer without oxidant gas, and then, following O<sub>2</sub> gas reacted with adsorbed Sr precursors. If SrO layer on RuO<sub>2</sub> became thick, no more oxygen was absorbed from RuO<sub>2</sub> and the normal growth rate was observed. By adjusting the cycle ratio of SrO layers and RuO<sub>2</sub> layers, stoichiometric SrRuO<sub>3</sub> film could be deposited, and crystallized into perovskite structure via PDA process. The crystallized SrRuO<sub>3</sub> electrode enabled the in-situ crystallization of SrTiO<sub>3</sub> dielectric film, but the dielectric film was not fully crystallized and its dielectric constant was not as high as in other studies.

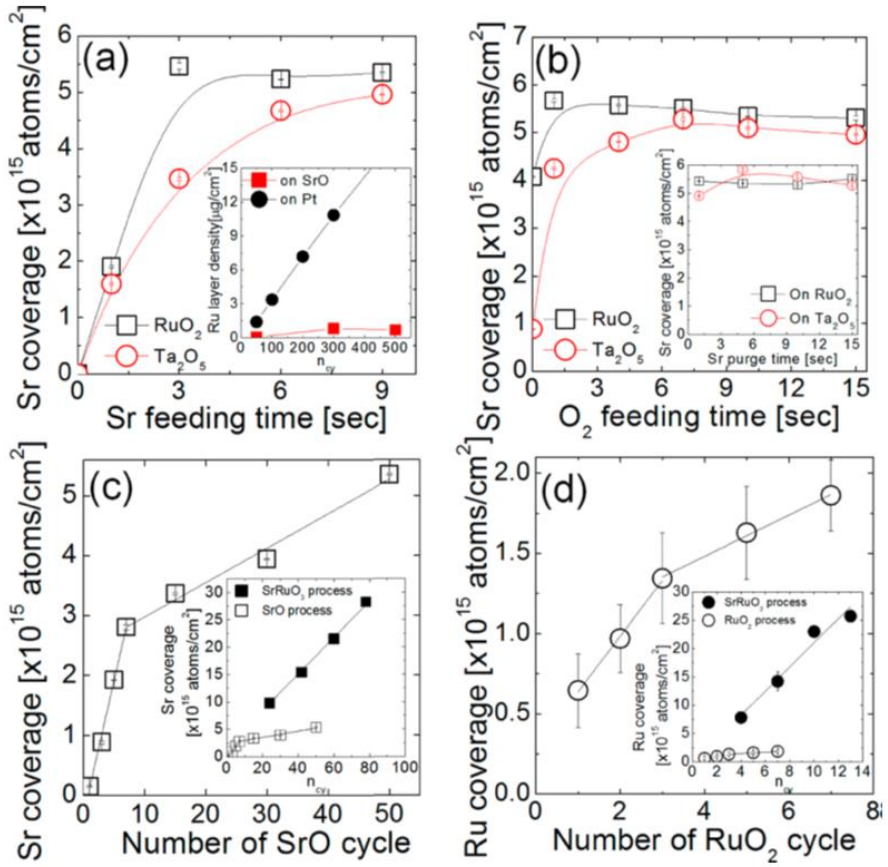


Figure 1.9 Growth behavior of SrRuO<sub>3</sub> film via ALD/CVD combing deposition method<sup>[15]</sup>

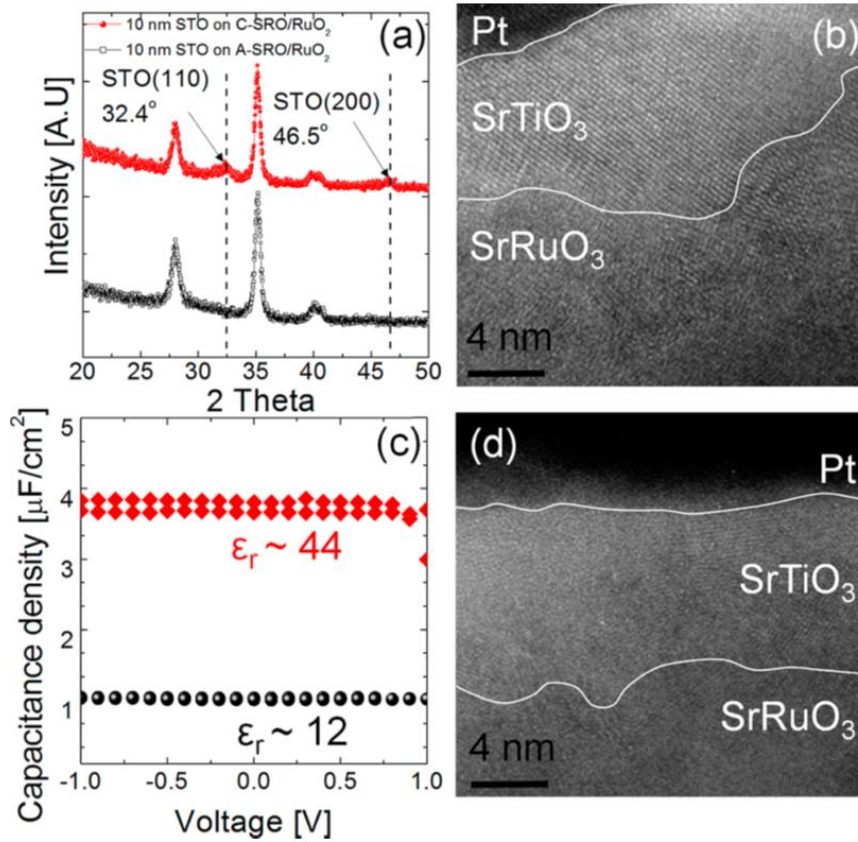


Figure 1.10 In-situ crystallization and dielectric property of SrTiO<sub>3</sub> dielectric on SrRuO<sub>3</sub> electrode.<sup>[15]</sup>

## 1.4. Bibliography

1. S. K. Kim, G. J. Choi, S. Y. Lee, M. Seo, S. W. Lee, J. H. Han, H. S. Ahn, S. Han, C. S. Hwang, *Adv. Mater.*, **2008**, 20, 1429
2. S. K. Kim, C. S. Hwang, *Electrochem. Solid-State Lett.*, **2008**, 11, G9
3. S. Knebel, U. Schroeder, D. Zhou, T. Mikolajick, G. Krautheim, *IEEE TRANSACTION ON DEVICE AND MATERIALS RELIABILITY*, **2014**, 14, 154
4. S. K. Kim, S. W. Lee, J. H. Han, B. Lee, S. Han, C. S. Hwang, *Adv. Funct. Mater.*, **2010**, 20, 2989
5. S. W. Lee, J. H. Han, S. Han, W. Lee, J. H. Jang, M. Seo, S. K. Kim, C. Dussarrat, G. Gatineau, Y.-S. Min, C. S. Hwang, *Chem. Mater*, **2011**, 23, 2227
6. W. Lee, J. H. Han, W. Jeon, Y. W. Yoo, S. W. Lee, S. K. Kim, C.-H. Ko, C. Lansalot-Matras, C. S. Hwang, *Chem. Mater*, **2013**, 25, 953
7. C. S. Hwang, “Atomic Layer Deposition for semiconductors”, Springer, **2013**.
8. V. Miikkulainen, M. Leskela, M. Ritala, R. L. Puurunen, *J. Appl. Phys.* **2013**, 113, 21301

9. T. Aaltonen, M. Ritala, K. Arstila, J. Keinonen, M. Leskelä, *Chem. Vap. Depos.* **2004**, 10, 215
10. S. K. Kim, S. Y. Lee, S. W. Lee, G. -Y. Choi, C. S. Hwang, J. W. Lee, H. Jeong, *J. Electrochem. Soc.* **2007**, 154, D95
11. T. Aaltonen, P. Alén, M. Ritala, M. Leskelä, *Chem. Vap. Depos.* **2003**, 9, 45
12. J. H. Han, S. W. Lee, G. -J. Choi, S. Y. Lee, C. S. Hwang, C. Dussarrat, J. Gatineau, *Chem. Mater*, **2009**, 21, 207
13. J. H. Han, S. W. Lee, S. K. Kim, S. Han, C. S. Hwang, C. Dussarrat, J. Gatineau, *Chem. Mater*, **2010**, 22, 5700
14. J. H. Han, S. Han, W. Lee, S. W. Lee, S. K. Kim, J. Gatineau, C. Dussarrat, C. S. Hwang, *Chem. Mater*, **2011**, 99, 022901
15. J. H. Han, W. Lee, W. Jeon, C. S. Hwang, *Chem. Mater*, **2012**, 24, 4686

## **2. Atomic Layer Deposition of Ru thin films using RuO<sub>4</sub> precursor and substrate effect on growth behavior**

### **2.1. Introduction**

The atomic layer deposition (ALD) process of the Ru metal thin film has been studied in various fields due to its excellent electrical properties and chemical stability. Ru metal has low resistivity ( $\sim 7 \mu\Omega \text{ cm}$ ), a high work function ( $\sim 4.7 \text{ eV}$ ), and catalytic capability. Based on these properties of Ru metal, the ALD of the Ru thin film is being studied for various purposes, such as for metallization in interconnect, as a barrier layer in Cu interconnect, and as a catalyst or sensor in electrochemistry or photovoltaics.<sup>1-3</sup> Among these, Ru metal is particularly advantageous as the electrode material of the dynamic random access memory (DRAM) capacitor. Ru is stable in its metallic state and is still electrically conducting even if oxidized to RuO<sub>2</sub> (resistivity:  $\sim 35 \mu\Omega \text{ cm}$ ); as such, its stable characteristics as an electrode material can be maintained in the DRAM capacitor fabrication post-process.<sup>4</sup> Also, accompanied by the scaling of the capacitor, Ru metal can be a solution to the leakage current issue. The high work function of Ru compared to the currently used TiN ( $\sim 4.2 \text{ eV}$ )

can mitigate the risk of increased leakage current caused by the small band gap of the next-generation DRAM dielectric films with a high dielectric constant ( $k$ ), such as  $\text{TiO}_2$  or  $\text{SrTiO}_3$ .<sup>5-11</sup> The leakage current issue can be further addressed when the surface of Ru is appropriately oxidized; this is because  $\text{RuO}_2$  has a higher work function ( $\sim 5.0$  eV) than Ru.<sup>4</sup>

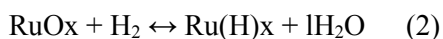
The Ru electrode can enhance the performance of the dielectric layer when adopted as the bottom electrode of the  $\text{TiO}_2$  dielectric film<sup>5-7</sup>. Previous studies showed that a thin rutile  $\text{RuO}_2$  surface layer could be formed on the Ru electrode during the ALD of the  $\text{TiO}_2$  film. This led to the growth of rutile  $\text{TiO}_2$ , whose dielectric constant is significantly higher ( $\sim 80-100$ ) than that of the more common anatase phase, whose dielectric constant is similar to that of the current  $\text{ZrO}_2$  ( $\sim 40$ ).<sup>5-7</sup> Therefore, Ru is an inevitable electrode material for the fabrication of the next-generation DRAM capacitor.

The development of the ALD process of the Ru metal film up to the mass-production-compatible level, however, has been hindered by a number of problems, such as the absence of an appropriate precursor, long incubation cycles, and substrate-type dependent growth behavior. While several metal-organic (MO) precursors, such as  $\text{Ru}(\text{C}_8\text{H}_{14}\text{O}_2)_3$  [ $\text{Ru}(\text{od})_3$ ],  $\text{Ru}(\text{C}_{11}\text{H}_{19}\text{O}_2)_3$  [ $\text{Ru}(\text{thd})_3$ ],  $\text{Ru}(\text{C}_5\text{H}_3)_2$  [ $\text{Ru}(\text{Cp})_2$ ],  $\text{Ru}(\text{C}_2\text{H}_5\text{C}_5\text{H}_4)_2$  [ $\text{Ru}(\text{EtCp})_2$ ], and 2,4-(dimethylpentadienyl)(ethylclopentadienyl)Ru [DER], have been extensively studied, they have carbon-containing ligands, involving the risk of

retaining the impurities in the grown film.<sup>12-16</sup> They showed the typical ALD growth rate of  $\sim 0.05$ - $0.1$  nm/cycle and tens of incubation cycles, whose precise numbers depend on the substrate type. The incubation cycles can be problematic when the Ru film is used as the top electrode of a DRAM capacitor. With a  $\sim 10$  nm design rule, the allowed gap between the neighboring capacitor nodes is only  $\sim 3$  nm after the deposition of the dielectric layer on the storage node, whose thickness is assumed to be  $\sim 3$  nm. A 3 nm-thick film requires only 30 cycles for an ALD process with a 0.1 nm/cycle growth rate. Therefore, ten incubation cycles constitute 1/3 of the total cycles, which can largely influence the repeatability of the process as the incubation cycles are usually less controllable than the normal growth cycles.<sup>16</sup> In addition to the reproducibility issue on account of the film thickness, the nucleation hindrance of an ALD process gives rise to the long incubation cycle issue, and such ALD process is prone to producing a rough film surface morphology. This may be a fatal issue in DRAM capacitor fabrication. Another probable concern is the relatively large molecule size ( $\sim 1$  nm) and low volatility of the MO precursors, which can be a critical problem when the Ru film is attempted to be used as the top electrode of the three-dimensional DRAM capacitor. This is because of the extremely narrow gap ( $\ll 3$  nm) and high aspect ratio ( $\sim 100$ ) of the capacitor structure where the Ru film has to be deposited. The large molecular size and low volatility can cause slow migration of the gaseous or surface-adsorbed molecules into the bottom portion of the extremely three-dimensional structure.

Therefore, an alternative Ru precursor that does not include carbon and has a small molecular size with a sufficiently high vapor pressure is necessary.

In this regard, the recently introduced carbon-free RuO<sub>4</sub> precursor is attracting a great deal of attention because it has a small molecular size compared with other MO precursors, and very high vapor pressure (10 Torr at 25 °C). The RuO<sub>4</sub> molecule has a tetrahedral structure with a 0.56 nm edge while the MO precursors generally have bulky ligands such as alkyl, cyclopentadienyl, or β-diketonate. As it does not have elements other than Ru and O, there is fundamentally no concern about carbonous contamination. Nonetheless, the strong oxidizing power of RuO<sub>4</sub> poses the risk of oxidation of the underlying layers in the integrated structure. Also, the Ru metal deposition from RuO<sub>4</sub> requires a reducing agent, typically molecular hydrogen (H<sub>2</sub>). Equations (1) and (2) shows a plausible ALD reaction mechanism, where n, m, and l are arbitrary numbers, and the subscript s represents the surface species.



The previous report showed that the pulsed chemical vapor deposition (CVD) process using the RuO<sub>4</sub> precursor and 95%N<sub>2</sub>/5%H<sub>2</sub> mixture gas could grow

the different phases of Ru and RuO<sub>2</sub> films depending on different reduction gas injection times for a given RuO<sub>4</sub> injection time.<sup>17,18</sup> The authors of Refs. 17 and 18 proposed that the Ru phase could catalyze the thermal decomposition of the adsorbed RuO<sub>4</sub> molecules into RuO<sub>2</sub> and eventually Ru. This could also be the case when the Ru film is grown via ALD, because the process is fundamentally dependent on the (multiple) reduction process of the RuO<sub>4</sub> molecules as represented by equation (1). Therefore, it can be expected that the ALD-type reaction of Ru may involve a complicated reaction pathway even if ALD can be achieved.

In the reported pulsed CVD Ru studies,<sup>17,18</sup> the thermal decomposition temperature of the RuO<sub>4</sub> molecule was identified to be ~150-170 °C, limiting the ALD temperature window to a low-temperature region. Indeed, the ALD-type growth behavior of the Ru deposition process was observed using RuO<sub>4</sub> on Si and Pt at a 100 °C substrate temperature.<sup>19,20</sup> As the low deposition temperature induced the insufficient reactivity of the precursor towards the diluted H<sub>2</sub> gas, the reduction gas was changed to pure H<sub>2</sub> gas<sup>19</sup> or H<sub>2</sub> plasma<sup>20</sup> to enhance the reactivity. These studies, however, provided limited information on the specific ALD growth behavior of the Ru film on the (transition) metal oxide substrate, except for the Al<sub>2</sub>O<sub>3</sub>. When the Ru film is adopted as the top electrode of the DRAM capacitor, it must be grown on high-k dielectric films, such as Ta<sub>2</sub>O<sub>5</sub> or ZrO<sub>2</sub> films.

In this study, the detailed ALD process of the Ru metal film on a Ta<sub>2</sub>O<sub>5</sub> thin-film substrate using the RuO<sub>4</sub> precursor and 95%N<sub>2</sub>/5%H<sub>2</sub> mixed reduction gas was examined. It was found that the Ta<sub>2</sub>O<sub>5</sub> thin film not only served as a passive substrate but also participated in the surface reaction on the growing Ru film surface, especially when it was reduced to Ta through its prolonged exposure to the N<sub>2</sub>/H<sub>2</sub> mixed reduction gas. This type of chemical interaction can significantly affect the growth of extremely thin films (<~3 nm) for DRAM capacitor application, which requires a highly detailed study. This work provides an in-depth understanding of this impending task especially by comparing the ALD behavior of the Ru film on a Ta<sub>2</sub>O<sub>5</sub> film substrate to that on a chemically inert Au thin-film substrate under identical conditions.

## 2.2. Experimental

Ru metal films were grown via ALD on a Ta<sub>2</sub>O<sub>5</sub>(5nm)/Si or Au(100nm)/Ti(5nm)/SiO<sub>2</sub>/Si substrate using the RuO<sub>4</sub> precursor (ToRuS, Air Liquide) and N<sub>2</sub>/H<sub>2</sub> (5% H<sub>2</sub>) mixed gas as the reduction gas. The RuO<sub>4</sub> precursor was dissolved in a carbon-fluorinated solvent with a 0.8 M density. Pure Ar (99.9999%) gas was used as the purge gas. The Ta<sub>2</sub>O<sub>5</sub>/Si substrate was prepared via CVD, using Ta(O(C<sub>2</sub>H<sub>5</sub>)<sub>5</sub>) and O<sub>2</sub> as the Ta precursor and oxygen source, at a ~400 °C substrate temperature. The Au/Ti/SiO<sub>2</sub>/Si substrate, on the other hand, was prepared via electron beam evaporation, using Au and Ti metal as the evaporation sources. The processing module was an 8-inch-diameter-wafer-scale showerhead-type instrument (CN-1, Plus-200). The ToRuS canister was kept at 17 °C to control its high vapor pressure, and carrier gas was not used to deliver the precursor into the chamber (vapor draw method). The temperature of the substrate was varied from 140 to 230 °C, and the working pressure of the chamber varied from 2.5 to 3 Torr due to the inevitably varying total gas flow rate. As the thickness of the metal film could not be estimated through an optical interference method such as ellipsometry, the film thickness and bulk density were investigated via X-ray reflectivity (XRR, PANalytical, X'pert Pro). The areal density of the Ru films was measured through X-ray fluorescence spectroscopy (XRF, Thermoscientific, ARL Quant'X), and their

crystalline structure was examined through X-ray diffraction (XRD, PANalytical, X'pert Pro), using Cu K $\alpha$  radiation. Here, areal density means the total amount of Ru atoms per area. The XRD analysis was performed in glancing angle mode (incident angle: 2°) and  $\theta$ -2 $\theta$  mode. The chemical states of the Ru 3d and Ta 4f orbitals were investigated through X-ray photoelectron spectroscopy (XPS, SIGMA PROBE, VG). The depth profile of the elements in the film was examined through secondary ion mass spectroscopy (SIMS, ION-TOF, TOF.SIMS-5), using accelerated Cs<sup>+</sup> as a sputtering ion. The bulk resistivity was calculated by combining the sheet resistance and thickness, which were measured through a four-point probe and XRR, respectively. The surface morphology and root-mean-squared (RMS) roughness of the Ru films were investigated through atomic force microscopy (AFM, JEOL, JSPM-5200). The Ru films were annealed for 2 minutes via rapid thermal annealing (RTA) at temperatures from 400 to 800 °C under N<sub>2</sub> atmosphere to examine their thermal stability. Cross-sectional transmission electron microscopy (TEM, JEOL, JEM-3000F) was used to investigate the three-dimensional step coverage of the Ru film on a hole-structured substrate with a 20:1 aspect ratio and a 100 nm opening diameter.

## 2.3. Results and Discussions

The self-limited growth behavior was investigated by varying the injection and purge times of the Ru precursor and N<sub>2</sub>/H<sub>2</sub> reduction gas to confirm the ALD behavior of the Ru film. Unless otherwise stated, all the experiments were performed on a Ta<sub>2</sub>O<sub>5</sub> film substrate. Before the ALD-specific saturation behavior was examined, the change in the Ru areal density according to the RuO<sub>4</sub> precursor injection time and at various temperatures was tested to confirm the temperature range at which the thermal decomposition of the Ru precursor did not occur. When the thermal decomposition of RuO<sub>4</sub> occurs, more Ru atoms will be deposited with increasing RuO<sub>4</sub> injection time in the CVD condition, contrary to the ALD case. In Figure 2.1(a), the variation of the Ru areal density was plotted vs. the precursor injection time at 140, 165, and 200 °C, respectively. The precursor purge time and the N<sub>2</sub>/H<sub>2</sub> reduction gas injection and purge times of the deposition sequence were 30, 10, and 10 s, respectively. As previously reported, saturation behavior was not observed at 200 °C, suggesting that this temperature corresponds to the CVD region.<sup>17</sup> The deposition amount, however, was saturated at 140 and 165 °C; as such, the film growths at these temperatures were of the ALD type. To more precisely determine the temperature dependency of the growth behavior, Ru films were deposited at a wider temperature range (140-230 °C), with an 8s-30s-10s-10s precursor injection-Ar

purge-reduction gas injection-Ar purge sequence. In Figure 2.1(b), the change in the Ru areal density vs. the deposition temperature is shown, and the Arrhenius plot is also shown in the inset of the same figure. The temperature dependency shows a different slope at the temperature below and above 180 °C, which can be more easily identified in the Arrhenius plot. The two different temperature regions show a linear relationship between the Ln (areal density) and 1/(growth temperature) plots in both temperature regions, and show slopes with the corresponding 0.25 and 0.45 eV activation energies at the low(<180 °C)- and high(>180 °C)-temperature regions, respectively. The intercept of the two linear-slope fittings indicates that the thermal decomposition temperature of RuO<sub>4</sub> is ~180 °C under the given deposition conditions. Thus, the subsequent ALD experiments were performed at 165 °C, sufficiently apart from the transition region. However, the film grown at 140 °C contained a considerable amount of RuO<sub>2</sub> phase, as confirmed via XPS in Figure 2.2. This result implies that the complete reduction of the adsorbed RuO<sub>4</sub> by the N<sub>2</sub>/H<sub>2</sub> reduction gas was not feasible at such a low temperature. Some of the authors previously reported that the same precursor had a ~150 °C thermal decomposition temperature,<sup>21,22</sup> which might have been incurred by different process pressure or state of reaction gases, suggesting that the growth conditions should be carefully controlled to achieve reliable growth behavior.

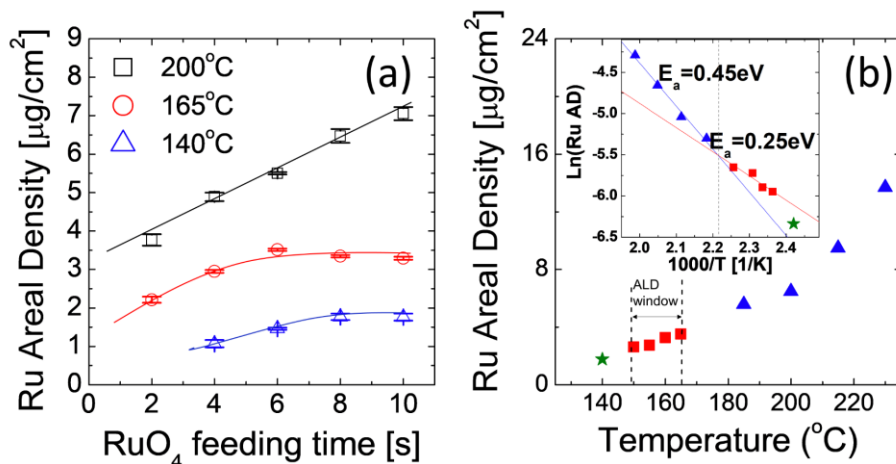


Figure 2.1 (a) Growth behavior of the Ru films on a Ta<sub>2</sub>O<sub>5</sub> substrate as a function of the RuO<sub>4</sub> precursor injection time at 140, 165, and 200 °C. (b) Variation in the Ru areal density of the Ru films on the Ta<sub>2</sub>O<sub>5</sub>/Si substrate as a function of the deposition temperature. Inset figure (b) shows the Arrhenius plot of the variations of Ln (Ru areal density) as a function of the reciprocal deposition temperature.

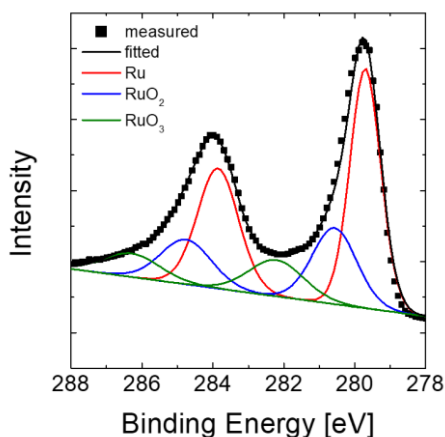


Figure 2.2 Ru 3d XP spectra of the Ru films grown on a Ta<sub>2</sub>O<sub>5</sub>/Si substrate at 140 °C.

The variations of the Ru areal density vs. the pulse and purge times of the N<sub>2</sub>/H<sub>2</sub> reduction gas and RuO<sub>4</sub> precursor at 165 °C when the total ALD cycle number was fixed at 15 are shown in Figure 2.3(a)-(d). Except for the varying parameters, the process times of RuO<sub>4</sub> injection, purge, N<sub>2</sub>/H<sub>2</sub> injection, and purge were fixed at 8, 30, 10 (step S, see below) or 20 (step L, see below), and 10 s, respectively. Apart from the expectation of achieving simple ALD-type saturation curves, the change in the Ru areal density vs. the injection time of the N<sub>2</sub>/H<sub>2</sub> reduction gas showed two saturation regions, as can be seen in Figure 2.3(a). For convenient discussion, the first and second saturation regions were named “step S” and “step L,” respectively, and the representative N<sub>2</sub>/H<sub>2</sub> reduction gas injection times of each step were set to 10 and 20 s. In Figure 2.3(b), it can be seen that no change occurred in the Ru areal density according to the N<sub>2</sub>/H<sub>2</sub> reduction gas purge time in steps S and L, which is a typical ALD behavior. In Figure 2.3(c), the deposition amounts of Ru as a function of the precursor injection time in steps S and L are shown. Both steps S and L showed saturated growth after 6s RuO<sub>4</sub> injection with different growth amounts (areal density), which was consistent with the deposition amounts shown in Figure 2.3(a). Both steps also showed saturation behaviors with the RuO<sub>4</sub> precursor purge time in Figure 2.3(d), after 30 s. From Figure 2.3(a)-(d), it can be concluded that there is a “two-step saturation” behavior (steps S and L) as a function of the N<sub>2</sub>/H<sub>2</sub> injection time, and the two processes showed ALD-specific self-limited growth behavior.

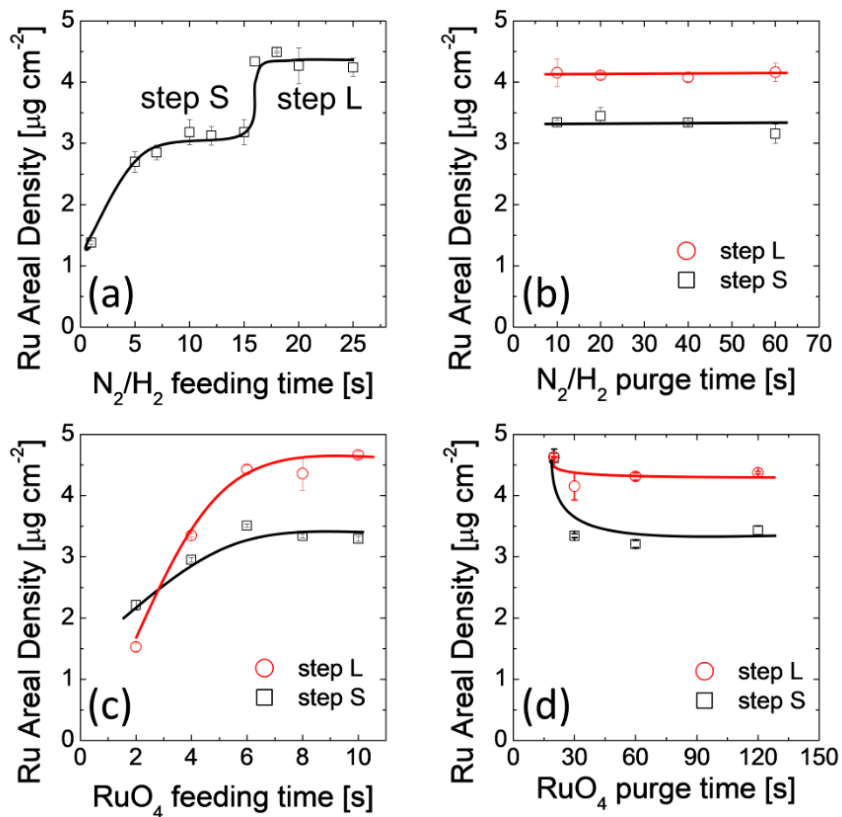


Figure 2.3 Variations of the Ru areal density on the  $\text{Ta}_2\text{O}_5/\text{Si}$  substrate grown at  $165^\circ\text{C}$  as a function of the time per ALD pulse: (a)  $\text{N}_2/\text{H}_2$  mixed-gas injection time; (b)  $\text{N}_2/\text{H}_2$  gas purge time; (c)  $\text{RuO}_4$  precursor injection time; and (d)  $\text{RuO}_4$  precursor purge time.

Such unusual two-step saturation behavior in the Ru thin-film ALD process has not yet been reported in both the CVD and ALD of Ru films. A previous study on the pulsed CVD growth reported a similar two-step saturation behavior according to the N<sub>2</sub>/H<sub>2</sub> gas injection time,<sup>18</sup> but it was due to the growth of the RuO<sub>2</sub> and Ru phases at low and high N<sub>2</sub>/H<sub>2</sub> gas injection times, respectively. Another study on the Ru ALD growth reported that the RuO<sub>2</sub> or Ru phase could be deposited according to the process conditions, such as the temperature or working pressure.<sup>23-25</sup> All the films which were shown in Figure 2, however, are metallic Ru films, as discussed below. Therefore, this work focused on the identification of such growth mechanism and the evaluation of the film properties grown in the two aforementioned steps.

Various methods were used to confirm the phases of the deposited films. First, XRD measurement of the 18 and 12 nm-thick Ru films in steps S and L was carried out to investigate the crystallinity of the films, which could be Ru or RuO<sub>2</sub> films or a mixture of these two. The films shown in Figure 2.3 are typically 3-4 nm thick, which are too thin to achieve reasonable XRD data; thus, a thicker film was grown for this experiment. As can be seen in the glancing angle XRD (GAXRD) spectra in Figure 2.4(a), clear peaks were observed at 38.5, 42.2, and 44.3° in both step S and L films. Such peaks corresponded to the (100), (002), and (101) planes of Ru metal, respectively, meaning that the deposited films were metal-phase Ru films, with minimal inclusion of RuO<sub>2</sub>. The preferred orientation of the films was also evaluated by the  $\theta$ -2 $\theta$  mode XRD

patterns shown in the inset of Figure 2.4(a). Similar to the GAXRD spectra, three peaks from the Ru metal film were detected in both cases, without the peaks of RuO<sub>2</sub>. The films grown by steps S and L showed more (101) (but more randomly than step L) and more (002) preferred growth behaviors, respectively. XRR measurements were performed to evaluate the physical densities of the films. Also shown in Figure 2.4(b) and (c) are the measured XRR curves and the fitted results of the films in steps S and L. The densities of the films, obtained through the fitting of the XRR curve, were 12.0 and 12.1 g cm<sup>-3</sup> in steps S and L, respectively, which were close to the bulk density of Ru metal (12.4 g cm<sup>-3</sup>).<sup>26</sup> The thicknesses obtained through the fitting of the XRR curves (18.4 and 12.1 nm) were similar to the thicknesses by areal density calculated through XRF areal density/bulk density via XRR (18.9 and 12.8 nm). There was a non-negligible difference, however, between the two films from steps S and L, which will be subsequently discussed in-depth, with additional analyses.

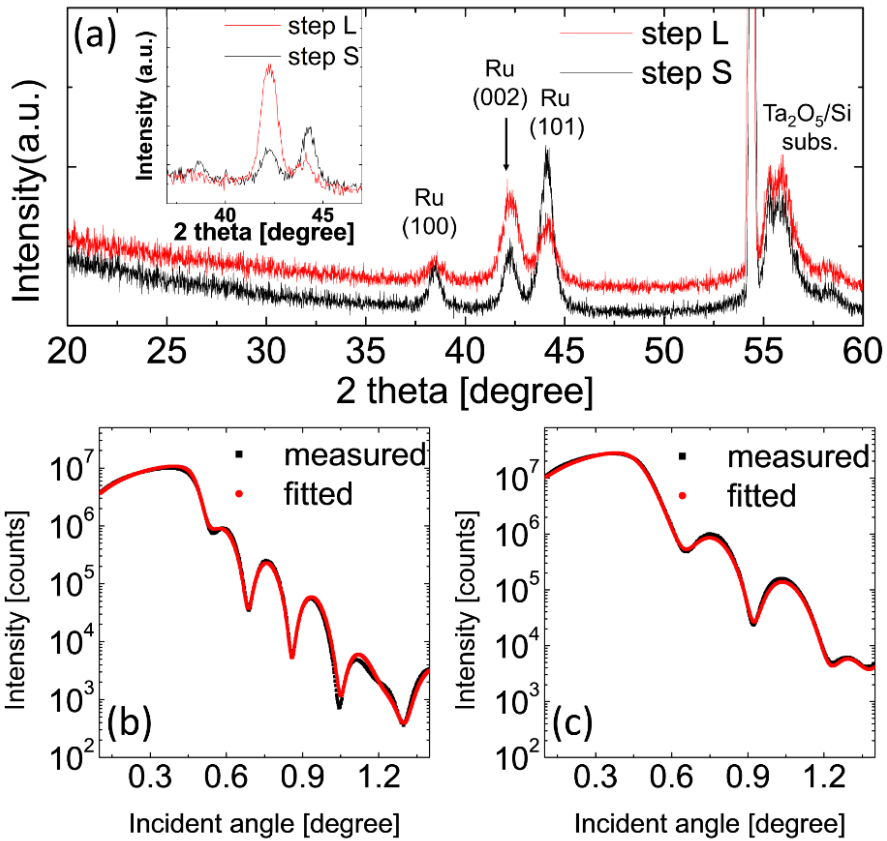


Figure 2.4 (a) XRD patterns in glancing angle mode of the films grown on a  $\text{Ta}_2\text{O}_5/\text{Si}$  substrate with different  $\text{N}_2/\text{H}_2$  gas injection times: the 18 nm film in step S and the 12 nm film in step L. Inset figure (a) shows the XRD patterns in  $\theta$ - $2\theta$  mode of the films, and figures (b) and (c) show the measured XRR curve and the fitted curve of the 18 nm Ru film in step S and the 12 nm Ru film in step L, respectively.

XPS was used to identify the oxidation state of the films further, as shown in Figure 2.5(a). Gentle Ar<sup>+</sup> ion etching (1 kV acceleration voltage) was conducted before XPS evaluation to remove the surface layer contaminated by exposure to air before the XPS measurement. As shown in Figure 2.5(a), the XP spectra of the Ru 3d orbital of the films with steps S and L precisely overlapped with each other, suggesting that the films had identical chemical states. Peak deconvolution was conducted to precisely identify the oxidation state of Ru, as shown in Figure 2.5(b). As the two films showed identical Ru 3d spectra, only the deconvolution results of the Ru spectra in step S are shown. An intense peak was observed at the 279.7 eV binding energy for Ru 3d<sub>5/2</sub> while weak peaks from the oxidized phases were found to be present at 280.8 eV for RuO<sub>2</sub> 3d<sub>5/2</sub> and at 282.1 eV for RuO<sub>3</sub> 3d<sub>5/2</sub>. As the C 1s bond overlapped with the Ru 3d spectra and was removed through Ar<sup>+</sup> ion etching, all the XPS spectra in such cases were aligned through Ru-Ru bonding at 279.7 eV. The atomic concentrations of oxygen, calculated based on the areal ratio of the XPS peaks, were 5.6 and 5.5% in steps S and L, respectively. The O 1s XP spectra of each film are shown in Figure 2.6. The unexpectedly high oxygen concentration can be ascribed to the surface sensitivity of the XPS method, and the surface oxide layer cannot be removed entirely even after the gentle in-situ Ar<sup>+</sup> ion etching.

SIMS measurement was employed to examine the depth profiles of each element, and the results of the Ru film in steps S and L are shown in Figure 2.5(c) and (d), respectively. Both Ru films showed sharp interfaces between the

grown Ru films and the Ta<sub>2</sub>O<sub>5</sub> substrates, and consistent profiles of the Ru and O elements along the direction of the film thickness. Carbon and oxygen impurities were detected only on the surfaces of the Ru films due to such films' exposure to air before the SIMS analysis. The surface carbon signal showed clearly higher intensity for the case of the step S film compared with the step L film. This is related to the different Ta-diffusion onto the film surface as discussed below. In the other ALD processes using MO precursors, carbon residue was found as a byproduct of the imperfect ALD reaction,<sup>17,24</sup> which could cause the deterioration of the electrical or physical properties of thin films. In this study, however, almost no carbon was detected from the bulk region of the Ru films, which could be confirmed from the consistent C signal level between the Ru film and Si substrate regions. The slight bump in the C signal near the Ta<sub>2</sub>O<sub>5</sub> film indicates the C contamination of such film because it was grown through another CVD using the Ta(OC<sub>2</sub>H<sub>5</sub>)<sub>5</sub> precursor and O<sub>2</sub>. The absence of C and O signals within the bulk regions of the Ru film suggests that the grown film was a highly pure Ru film for both steps S and L. Therefore, the unusual two-step saturation growth behavior vs. the reduction gas injection time did not originate from a phase change but from some other unknown factor.

The high and flat TaO<sup>2-</sup> signal intensities were detected at the interface between Ru and Si substrate showing the presence of the Ta<sub>2</sub>O<sub>5</sub> layer, and their distribution are almost identical in the two films. Interestingly, a clear TaO<sup>2-</sup> signal was detected on the sample surfaces in Figure 2.5 (c) and (d). SIMS can

have such an artifact that surface concentration of certain elements overestimated by matrix effect, which appears to be the case for  $^{18}\text{O}^-$ ,  $\text{Ru}^-$ , and  $\text{Si}^-$  in Figure 2.5 (c) and (d). Their ( $^{18}\text{O}^-$ ,  $\text{Ru}^-$ ,  $\text{Si}^-$ ) adverse effects are identical in both sample surfaces, suggesting that these effects can be ignored. However, this was not the case for the  $\text{TaO}^{2-}$  and  $\text{C}^-$ ; their intensities are obviously higher for the case of film with step S compared with step L. Also, the  $\text{TaO}^{2-}$  intensity was slightly higher inside the bulk Ru film with step S compared with step L, while the  $\text{C}^-$  intensities inside the two films are almost identical. Therefore, the higher  $\text{C}^-$  intensity on the surface of the step S film could be induced by the higher adsorption of the adventitious carbon from the atmosphere due to the high binding energy between Ta and C. The presence of higher Ta concentration on the step S Ru film surface compared with the step L Ru film was further confirmed by examining the SIMS depth profiles of the two Ru films with 15nm-thick sputtered Ti capping layer. This data were included in Figure 2.7. It was found that the  $\text{TaO}^{2-}$  signal was found on the Ti layer surface for the case of the step S film (albeit weaker than Figure 2.5 (c)), but it was negligible on the Ti layer surface on the step L Ru film. This data again confirmed the higher presence of the Ta on the step S Ru film surface as well as quite a high diffusion of Ta to the film surface. Since  $\text{Ta}_2\text{O}_5$  layer was deposited only before Ru growth,  $\text{TaO}^{2-}$  detection at the Ru layer surface indicates that Ta (or Ta-O) was diffused onto the growing film surface during the ALD of the Ru film.

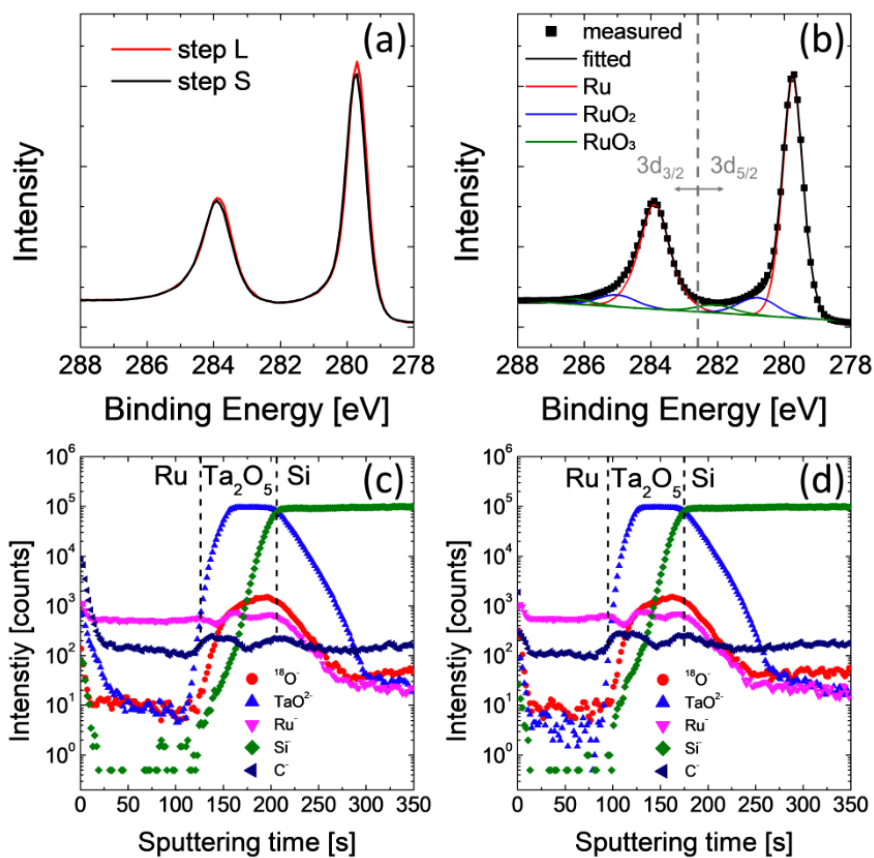


Figure 2.5 (a) Ru 3d XP spectra of the Ru films grown on a Ta<sub>2</sub>O<sub>5</sub>/Si substrate with different N<sub>2</sub>/H<sub>2</sub> gas injection times. (b) Deconvoluted peaks of the Ru 3d XP spectra of the Ru film grown in step S. (c)-(d) SIMS depth profile of the Ru films grown on a Ta<sub>2</sub>O<sub>5</sub>/Si substrate in steps S and L, respectively.

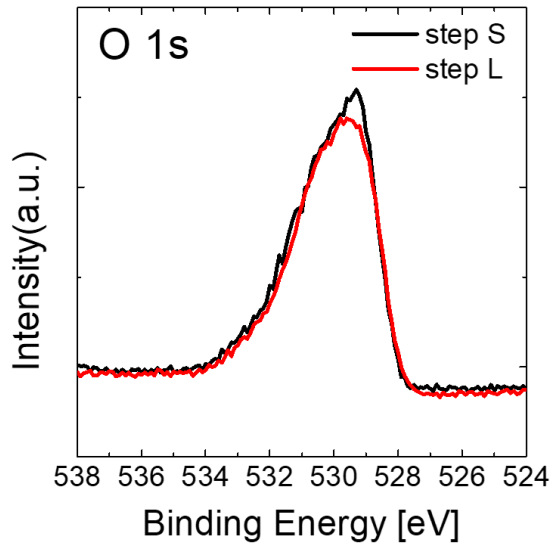


Figure 2.6 O 1s XP spectra of the Ru films grown a Ta<sub>2</sub>O<sub>5</sub>/Si substrate with different N<sub>2</sub>/H<sub>2</sub> gas injection times.

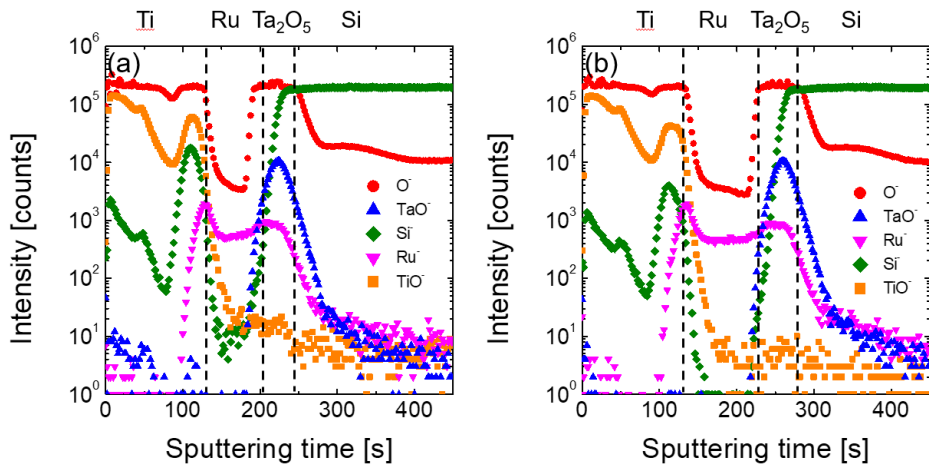


Figure 2.7 (a)-(b) SIMS depth profile of the Ru films grown on a Ta<sub>2</sub>O<sub>5</sub>/Si substrate in steps S and L, respectively. Ti passivation layers were deposited on each Ru film.

Further investigation of the detailed chemical states of the film surface and interface was performed via XPS to explain the surface  $\text{TaO}^{2-}$ . Here, the XPS Ta 4f signals were examined from three types of samples without surface etching: (i) a  $\text{Ta}_2\text{O}_5$  substrate film for inspecting the initial composition of the substrate; (ii) a Ru film (2.7 nm (for step S) and 3.5 nm (for step L)) thinner than the probing depth of XPS for the Ta 4f signal (~5-10 nm) on the  $\text{Ta}_2\text{O}_5$  substrate; and (iii) a thicker Ru film (15 nm), which would provide information only on the Ta atoms on the Ru film surface. The Ru films were delivered to the XPS chamber within 1 hour after deposition to minimize the effect of exposure to air on the deposited film surface. Figure 2.8 shows the spectrum from the  $\text{Ta}_2\text{O}_5$  substrate film. The binding energy was calibrated via C-C bonding at 284.5 eV. The XPS spectrum clearly showed that the film was largely composed of fully oxidized  $\text{Ta}_2\text{O}_5$  with a 25.5 eV binding energy, and also contained a peak from the O 2s orbital at a lower-binding-energy region. Figure 2.9(a) and (b) show the spectra from the thin Ru films grown by steps S and L, respectively. The spectra show much-decreased peak intensities due to the absorption of the photoelectrons by the thin Ru layer. Low film thickness was permitted, however, for examining the interfacial  $\text{Ta}_2\text{O}_5$  film state as well as the surface Ta atoms. Both XPS spectra were deconvoluted into peaks from the  $\text{Ta}^{5+}$ ,  $\text{Ta}^0$ , and O 2s species. The binding energy of the  $\text{Ta}^0$  and O 2s peaks were 20.3 and 20.8 eV, respectively. The peak intensity of the  $\text{Ta}^0$  signals was non-negligible with respect to the  $\text{Ta}^{5+}$  signals from the substrate. As a  $\text{Ta}^0$

signal was not shown in the pristine Ta<sub>2</sub>O<sub>5</sub> substrate (Figure 2.8), the Ta metal phase was formed during the Ru film deposition process through the partial reduction of Ta<sub>2</sub>O<sub>5</sub> to Ta by the H<sub>2</sub> molecules as shown in equation (3).



The high ratio between Ta<sup>0</sup> and Ta<sup>5+</sup> of the step S sample (2.7 nm-thick Ru) indicates that the Ta<sup>0</sup> signal can originate from the Ru surface rather than from the substrate considering (i) the attenuation effect of the signal from the underlying Ta<sub>2</sub>O<sub>5</sub> layer by the overlying Ru layer, and (ii) the nearly intact thickness of the Ta<sub>2</sub>O<sub>5</sub> layer after Ru deposition, as confirmed by the previous SIMS results. The comparison of the spectra before and after the surface etching of the thicker Ru films (15 nm) (Figure 2.9(c)-(f)) further supports the presence of Ta<sup>0</sup> on the Ru surface. Both the 15 nm films grown under the step S and L N<sub>2</sub>/H<sub>2</sub> injection conditions clearly showed the emergence of Ta<sup>0</sup> peaks without a Ta<sup>5+</sup> peak from the substrate before the surface etching. Although the XPS peak intensities were quite weak, the asymmetric peak shapes indicated that they did not represent single O 2s peak. The reproduction of the peak shape during the XPS peak deconvolution process required the inclusion of the Ta<sup>0</sup> components as shown in the figures. In fact, this was also the case when the deconvolution of the Ta peaks were attempted in Figure 2.9(a) and (b). Figure

2.9(e) and (f) show that the peaks disappeared after the  $\text{Ar}^+$  ion etching of the  $\sim 3$  nm film surface for steps S and L, respectively.

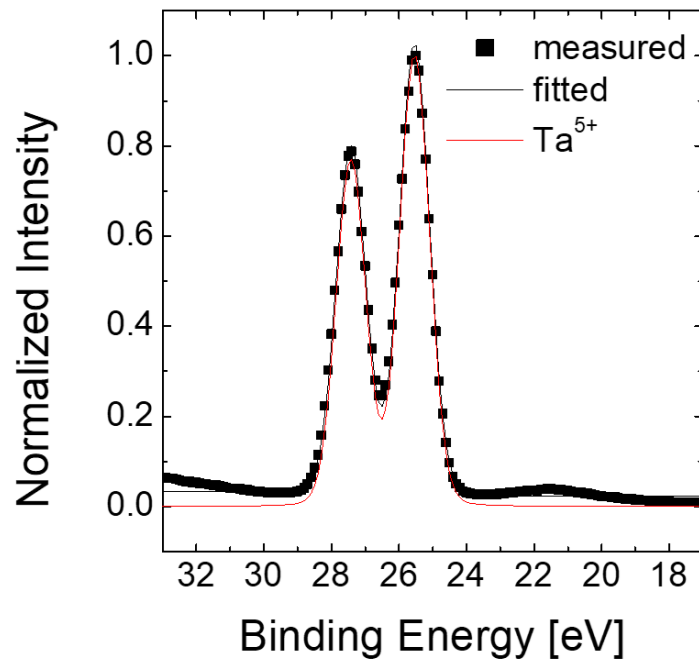


Figure 2.8 Ta 4f XP spectra of the pristine Ta<sub>2</sub>O<sub>5</sub>/Si substrate

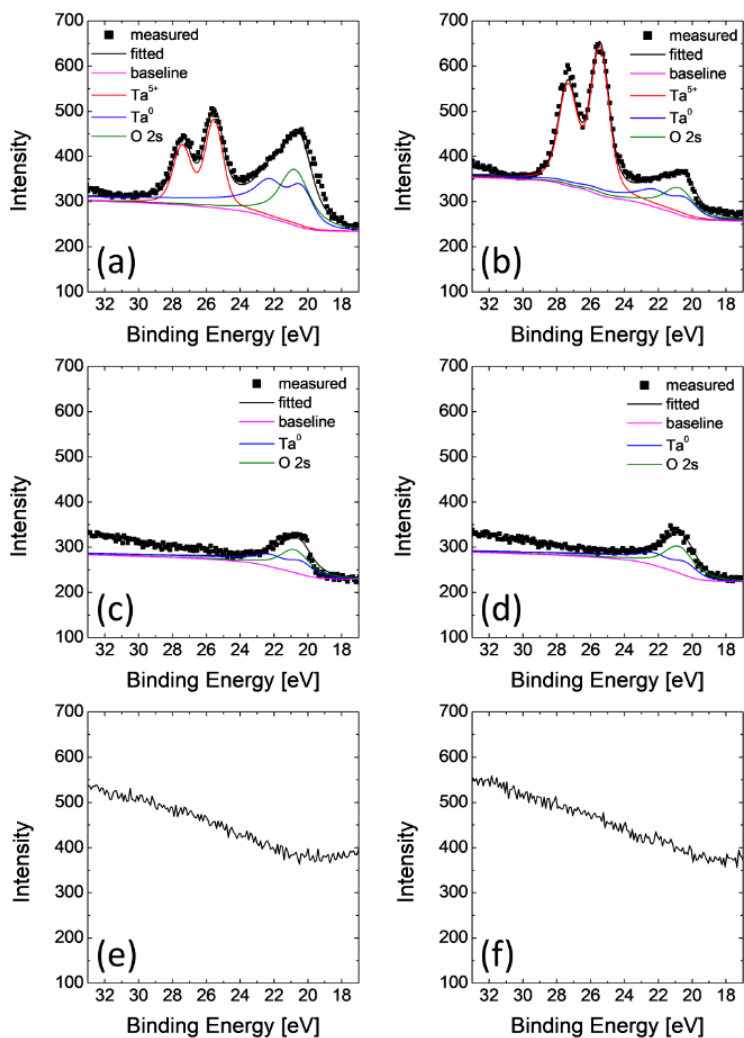


Figure 2.9 Ta 4f XP spectra of the Ru films grown on the same substrate with different N<sub>2</sub>/H<sub>2</sub> gas injection times and thicknesses: (a) 2.7 nm-thick Ru film in step S without surface cleaning; (b) 3.5 nm-thick Ru film in step L without surface cleaning; (c) 15 nm-thick Ru film in step S without surface cleaning; (d) 15 nm-thick Ru film in step L without surface cleaning; (e) 15 nm-thick Ru film in step S after 3 nm etching; and (f) 15 nm-thick Ru film in step L after 3 nm etching.

ALD-grown films which included bottom layer materials at the top surface were already reported in the previous studies. Popovici et al. reported that Ti was segregated to the surface of ALD-grown Ru film when it was deposited on TiN film.<sup>27</sup> The segregated Ti elements on film surface affected the growth rate and film properties of Ru film. Ti elements were concentrated on the film surface rather than inside the Ru layer. Song et al. reported that a thin WO<sub>x</sub> layer was consistently formed and ‘floated’ on the NiO film during the NiO ALD process when NiO was grown on a W film. The floating surface W species increased the ALD growth rate by enhancing the chemical adsorption of the Ni precursor.<sup>28</sup> These previous studies show very analogous results with the current study. It was expected that the floated substrate material (Ta or Ta-O) affected the Ru film growth behavior in this study.

For the detailed investigation of the possible influence of floated Ta elements on the surface, Ru films were grown on chemically inert Au/Ti/SiO<sub>2</sub>/Si substrate. In Figure 2.10(a), the variation of Ru areal density as a function of N<sub>2</sub>/H<sub>2</sub> injection was shown. The RuO<sub>4</sub> precursor injection time, precursor purge time, and N<sub>2</sub>/H<sub>2</sub> gas purge time were fixed at 8, 30, and 10 s, respectively, and 15 ALD cycles were conducted, as in the case shown in Figure 2.3. Contrary to the case of the Ru films on a Ta<sub>2</sub>O<sub>5</sub> substrate, the typical saturation behavior in the normal ALD process was observed in this case.

The variations of the Ru areal density as a function of the deposition cycle number on the Ta<sub>2</sub>O<sub>5</sub> (steps S and L) and Au substrates (10 s N<sub>2</sub>/H<sub>2</sub> feeding time), and the results are shown in Figure 2.10(b). From the slopes of the best-linear-fitted graphs of the experiment data (symbols), the saturated growth rate per cycle (GPC) could be estimated as 0.37 nm/cycle in step S on Ta<sub>2</sub>O<sub>5</sub>, 0.26 nm/cycle in step L on Ta<sub>2</sub>O<sub>5</sub>, and 0.22 nm/cycle on Au. There were eight and two incubation cycles for steps S and L, respectively, whereas almost no incubation cycle was required for the Au substrate. The enhancement of nucleation and the non-involvement of the incubation cycles in the Ru ALD on the Au surface using DER were also reported elsewhere.<sup>29</sup>

The standard formation energy of gold oxide phase (Au<sub>2</sub>O<sub>3</sub>) is 75.5 kJ/mol, which means that the oxidation of Au metal is improbable.<sup>30</sup> The conventional self-limited behavior and lower GPC of Ru film grown on Au substrate suggest that the characteristic growth on Ta<sub>2</sub>O<sub>5</sub> substrate must be ascribed to the involvement of the floated Ta species during ALD.

The growth rate of 0.22 nm/cycle of the ALD Ru film on the Au layer was already over two times higher growth rate compared with the values from the previous studies using metal-organic Ru-precursors, which could be ascribed to the smaller molecular size of the RuO<sub>4</sub> precursor of this study. The monolayer thickness of the (002) plane of hexagonal Ru is 0.22 nm, so 0.22 nm/cycle of growth rate indicated the full monolayer growth per cycle in this ALD process.

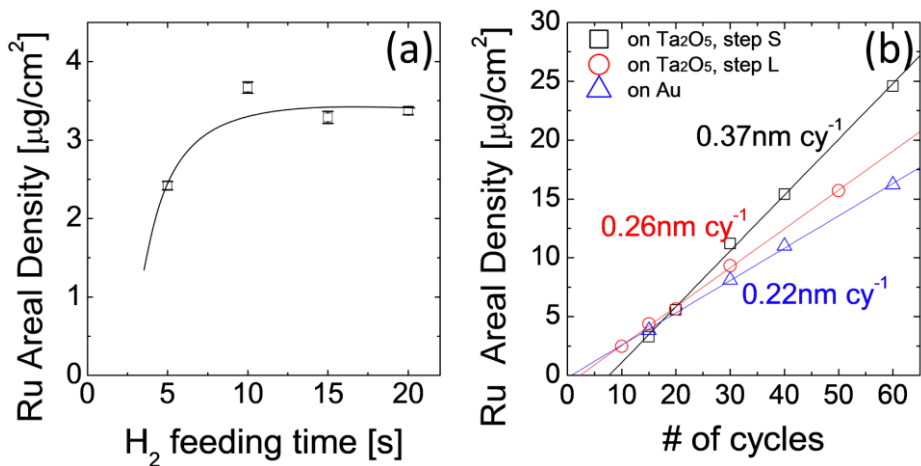


Figure 2.10 (a) Variations of the Ru areal density of the films grown on an Au substrate as a function of the  $\text{N}_2/\text{H}_2$  gas injection time. (b) Variations of the Ru areal density on the films grown on a  $\text{Ta}_2\text{O}_5/\text{Si}$  or Au substrate as a function of the number of ALD cycles.

As the higher GPC of Ru film on Ta<sub>2</sub>O<sub>5</sub> substrate than Au substrate must be resulted from the surface Ta species, the following Ta-mediated RuO<sub>4</sub> adsorption reaction (equation (4)) is possible owing to the thermodynamically favorable formation of Ta<sub>2</sub>O<sub>5</sub> by the reaction. (The standard formation energy of Ta<sub>2</sub>O<sub>5</sub> and RuO<sub>2</sub> are -2088.573 and -201.190 kJ/mol,<sup>31,32</sup> respectively, which correspond to -417.72 and -100.60 kJ per molar oxygen.)



This large oxidation propensity of Ta compared with Ru is also the fundamental reason for the Ta diffusion onto the surface. That is, as RuO<sub>4</sub> is the oxygen source, Ta moves towards the surface to be oxidized.

The subsequent injection of the reduction gas converts Ta<sub>2</sub>O<sub>5</sub> and RuO<sub>2</sub> to metal Ta and Ru, respectively, according to equation (5) below.



These combined reactions indicate that one surface Ta atom results in the deposition of 1.25 Ru atoms during one ALD cycle. This may correspond to the surface-Ta-enhanced ALD mechanism for steps S and L on the Ta<sub>2</sub>O<sub>5</sub> film substrate, explaining the exceptionally high GPC of 0.37 nm/cycle for step S.

In contrast, the pure Ru surface may proceed with ALD reaction via the inverse disproportionation reaction of equation (6) and the reduction of the produced RuO<sub>2</sub> to the final Ru and H<sub>2</sub>O according to equation (7).<sup>18,22</sup>



An alternative reaction can be represented by equations (8) and (9) below.



, where (s) represents the surface species. Both reaction schemes (equations (6)/(7) and (8)/(9)) result in the same Ru film growth. In this case, one Ru atom results in the deposition of one Ru atom after the completion of one ALD cycle because one of the two Ru atoms (or Ru-4H(s)) on the righthand side of equation (7) (or equation (9)) is the original surface Ru atom (or Ru-4H(s)). Therefore, the GPC may be lower than that in the case mediated by the Ta atoms. This corresponds to the case where ALD proceeded on the Au substrate. In both cases, the growing film surfaces recovered the Ta+Ru (for the Ta<sub>2</sub>O<sub>5</sub> substrate) and Ru (for the Au substrate) surface configurations, respectively, after the

purge step of the reduction gas, which also removed the H<sub>2</sub>O byproduct. By this mechanism, the substrate-dependent GPC could be well explained by the existence of Ta diffusion to the surface.

Although the deposition amount of Ru was increased in step L than in step S when the N<sub>2</sub>/H<sub>2</sub> gas injection time increased, the saturated GPC was much higher in step S case than in step L case. This was understood by the difference in the incubation cycle of two processes, mentioned above. (eight vs. two cycles) Since the ALD cycle in Figure 2.3 was just 15 cycles, the effect of nucleation delay was still presented in Figure 2.3. The genuine growth rate in bulk Ru film region is higher in step S case than in step L case. The low GPC and short incubation cycle of step L compared to step S could also be explained by the floating Ta model. The calculated areal density of the Ru films grown by 15 cycles under the step S and L conditions from the estimated incubation cycle numbers and bulk film growth rate was ~3.2 and ~4.4 μg/cm<sup>2</sup>, respectively, which are consistent with the data shown in Figure 2.3(a).

The shorter nucleation delay of step L than step S could be induced by the different N<sub>2</sub>/H<sub>2</sub> exposure time of Ta<sub>2</sub>O<sub>5</sub> layer and subsequent reduction before Ru film growth. Generally, hydroxyl(-OH) groups are present in metal oxide surface, and its amount can be controlled by H<sub>2</sub> reduction gas.<sup>33-36</sup> During the incubation cycle, the Ta<sub>2</sub>O<sub>5</sub> substrate was not fully covered by Ru nucleus and exposed to N<sub>2</sub>/H<sub>2</sub> reactant gas. The total N<sub>2</sub>/H<sub>2</sub> injection times during the

incubation cycle were calculated as 80 s (10 s X 8 cy) and 40 s (20 s X 2 cy) for step S and step L, respectively. Increasing reactant gas exposure time before Ru growth induced more hydroxyl group, which is a significant factor of the number of adsorption sites of RuO<sub>4</sub> precursor. It is likely to have more hydroxyl group and more metal Ta which was reduced from Ta<sub>2</sub>O<sub>5</sub> in step S case before the Ru fully covered the Ta<sub>2</sub>O<sub>5</sub> film. Since the direct in-situ measurement of the hydroxyl group density on the Ta<sub>2</sub>O<sub>5</sub> substrate was not applicable, the water contact angle (WCA) method was conducted to compare the variation of hydroxyl group density. The results were shown in Figure 2.11. As shown in Figure 2.11, the contact angle increased with longer N<sub>2</sub>/H<sub>2</sub> time, which indicated that the surface of Ta<sub>2</sub>O<sub>5</sub> film became more hydrophilic. It proved that more hydroxyl groups were formed on the Ta<sub>2</sub>O<sub>5</sub> substrate. The two flat regions in Figure 2.11 coincides with the two-step saturation of the growth rate shown in Figure 2.3(a). The abrupt change of contact angle at around 17 s of N<sub>2</sub>/H<sub>2</sub> treat time is believed to be caused by another reaction involvement such as the appearance of completely reduced Ta or catalytic reduction enhancement to the adjacent Ta<sub>2</sub>O<sub>5</sub> materials by the formed Ta metal.

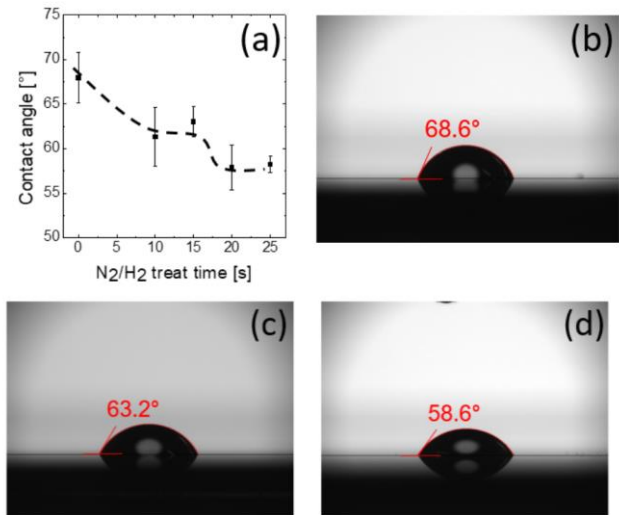


Figure 2.11 (a) Variation of the water droplet contact angle on the Ta<sub>2</sub>O<sub>5</sub> substrate as a function of N<sub>2</sub>/H<sub>2</sub> injection time; (b) the contact angle image of pristine Ta<sub>2</sub>O<sub>5</sub> substrate; (c) the contact angle image of Ta<sub>2</sub>O<sub>5</sub> substrate with 15s of N<sub>2</sub>/H<sub>2</sub> feeding; (d) the contact angle image of Ta<sub>2</sub>O<sub>5</sub> substrate with 25s of N<sub>2</sub>/H<sub>2</sub> feeding.

The schematic diagrams of initial growth mechanisms of step S and step L were summarized in Figure 2.12 (a) and (b), respectively. In the first and second rows, step S which had shorter exposure of Ta<sub>2</sub>O<sub>5</sub> to N<sub>2</sub>/H<sub>2</sub> had less hydroxyl group on surface and the nucleation of Ru was retarded compared to step L. The higher Ta concentration for step S can be explained by the larger uncovered portion of the Ta<sub>2</sub>O<sub>5</sub> substrate during the N<sub>2</sub>/H<sub>2</sub> gas injection for the first several ALD cycles. The larger incubation cycle for step S compared to step L supports the less surface coverage for step S because Ta<sub>2</sub>O<sub>5</sub> reduction was less likely under the Ru nuclei. The third row of Figure 2.12 describes this process. Therefore, step S could have induced greater Ta<sub>2</sub>O<sub>5</sub> reduction, and the produced Ta atoms tended to diffuse onto the growing Ru film surface compared with the step L case because the latter process more rapidly covers the Ta<sub>2</sub>O<sub>5</sub> with a Ru layer, making Ta<sub>2</sub>O<sub>5</sub> reduction less likely compared with the other case. Thus, the higher GPC of the step S sample compared with the step L sample can be attributed to the higher Ta portion on the Ru film surface.

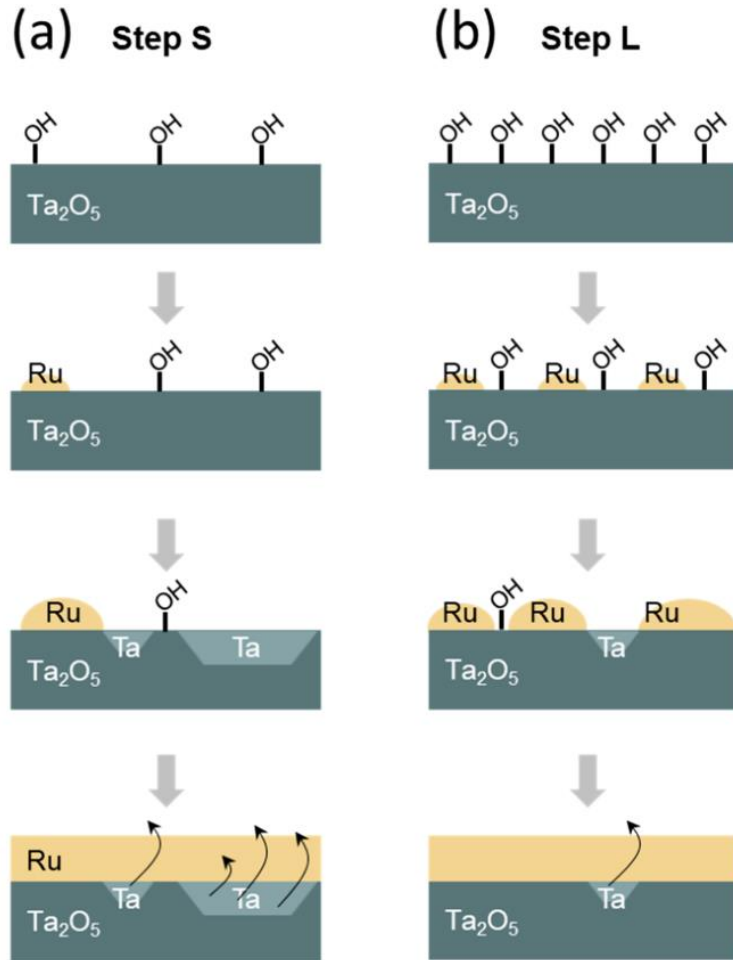


Figure 2.12 Schematic diagram of the initial growth stage in (a) step S and (b) step L.

The exceptionally high growth rates of ALD in this study need further discussion. The Ru atom has a 0.13 nm radius and a 0.22 nm monolayer thickness along the c-axis of its hexagonal close-packed crystal structure, which corresponds to 1 Ru atom per 0.059 nm<sup>2</sup> unit cell area. The 0.22 nm/cycle GPC on the Au substrate thus well coincides with the ideal monolayer growth rate along the z-axis. Meanwhile, the 0.22 nm monolayer thickness of Ru crystal suggests that a more-than-one-monolayer-thick Ru layer grows on the Ta<sub>2</sub>O<sub>5</sub> substrate. The achieved 0.37 nm/cycle GPC and the 0.26 nm/cycle GPC for the case of steps S and L correspond to 1.68 and 1.18 monolayer growth per cycle, respectively. As discussed above, such an abnormally high growth rate can be attributed to the Ta-induced growth enhancement. As only 1.25 Ru atoms can be deposited per Ta atom according to equations (3) and (4), however, the very high GPC of 0.37 nm/cycle cannot be explained even if the surface density of Ta is identical to that of Ru. In fact, the Ta atomic surface density is even lower for the body-centered cubic-structured Ta crystal, where two Ta atoms with a 0.17 nm atomic radius reside within 0.218 nm<sup>2</sup> of the unit cell area than that for the Ru crystal. This surface density of Ta is approximately half that of Ru; as such, the Ta monolayer must result in a ~0.15 nm/cycle (0.22 nm/cycle × 1.25 × 0.54) GPC. Therefore, the only feasible explanation for such an exceptionally high GPC is the multiple-layer adsorption of the RuO<sub>4</sub> molecules through the reactions with the multiple Ta layers (two to three atomic layers) on the Ru film surface. For example, when two layers of Ta atoms reside on the growing film

surface, the adsorbing  $\text{RuO}_4$  reacts with the first layer of Ta, forming a  $\text{RuO}_2$  layer according to equation (4). As there remain unreacted Ta atoms underneath the just-formed  $\text{RuO}_2/\text{Ta}_2\text{O}_5$  monolayer, further  $\text{RuO}_4$  adsorption can occur via the same reaction (equation (4)) through the just-formed  $\text{RuO}_2/\text{Ta}_2\text{O}_5$  monolayer. The slightly lower growth rate for step L can be similarly explained when a lower available Ta concentration on the surface is considered. The higher Ta signals on the film surface in SIMS and XPS corroborate such interpretation.

Another mechanism for the extraordinary growth behavior could be considered based on the different preferred crystallographic orientation of the step and step L Ru films. As mentioned in the inset of Figure 2.4(a), Ru films in step L has 002-preferred orientation while Ru films in step S are more randomly orientated. Different GPCs with regards to the film orientation have been previously reported.<sup>37</sup> In that report, the close-packed (002) plane hindered the oxygen diffusion from the subsurface region, which could enhance the adsorption of the precursor by oxidative dissociation of the ligands. However, the  $\text{RuO}_4$  precursor of this study is already with the fully (or over-) oxidized form, so its adsorption would not be enhanced on the oxygen-giving surface. Also, it was not guaranteed that the surfaces of the 002-preferred grains had (002) surface planes. Therefore, preferred-orientation-dependent growth behavior may not be applied in this study.

Next, the physical properties of the two film types (steps S and L) were evaluated. To evaluate the conductive property of Ru films in both steps, the bulk resistivity of the Ru film was calculated by plotting the sheet resistance estimated through the four-point probe method, and the thickness according to the  $(\text{sheet resistance})^{-1} = (\text{bulk resistivity})^{-1} \times \text{thickness}$  relation (Figure 2.13(a)). From the slopes of the best-linear-fitted graphs, the bulk resistivities, excluding the interface resistance, were determined to be 23.8 and 22.8  $\mu\Omega \text{ cm}$  for steps S and L, respectively. The resistivity values lower than 30  $\mu\Omega \text{ cm}$  were similar to the previous results of the Ru thin films,<sup>1,14,15,38</sup> and the two almost identical values suggested the insignificant influence of the remaining Ta on the surface on the electrical property. Another notable finding is that the linear tendency was retained down to the thinnest film ( $\sim 2.5 \text{ nm}$ ), suggesting that such thin film possessed a degree of electrical conductivity identical to that of the thicker film. This is a critically important aspect of these films considering their application to the top electrode of the DRAM capacitor, whose thickness must be  $< \sim 3 \text{ nm}$ .

The thermal stability of Ru films was also tested because the very thin metal film had an agglomerating tendency, which could increase the surface roughness through an annealing process. The rough surface could result in electric field concentration, and could increase the leakage current of the capacitor; as such, the high thermal stability of the Ru thin film as an electrode material should be ensured.<sup>39</sup> The Ru films were annealed in  $\text{N}_2$  atmosphere for 2 minutes through the RTA process, and the surface roughness was investigated

via AFM, as shown in Figure 2.13(b). In the as-deposited state, the Ru film in both steps showed an RMS roughness value smaller than 0.5 nm, as corroborated by the XRR results shown in Figure 2.4(b) and (c). As a result of the annealing process, the RMS roughness of the Ru films in step S was stable up to 500 °C but increased abruptly thereafter. The surface morphologies of the Ru films in step S in the as-deposited and annealed (at 800 °C) states are shown in the inset of Figure 2.13(b). Contrary to the film in the as-deposited state, the annealed Ru film had larger grains, which were formed through agglomeration. Unlike in the case of step S, in the case of step L, the RMS roughness was stable even at the 600 °C annealing temperature, and only slightly increased (to 0.7 nm) at 800 °C. Such difference in thermal stability might have been induced by the more random and 002-preferred growth directions of the two films. For the random film, the film may agglomerate or may be deformed by the thermal energy to gain the minimum surface energy state. In contrast, the 002-preferred-growth-direction film already had the most stable surface energy configuration; as such, the driving force for the minimum surface energy configuration should be lower to ensure better thermal stability.

Finally, the step coverage of the 10 nm-thick Ru film deposited on a hole-structured substrate with a 100 nm opening diameter and a 20:1 aspect ratio was examined from the cross-sectional TEM image in Figure 2.13(c). The dark-contrast layer was the Ru film, which was deposited on the previously deposited ZrO<sub>2</sub>/TiN layer (polycrystalline contrast); it showed a high step coverage of

~95%. The rough-looking contrast was from the polycrystalline image from the differently oriented grains of the Ru layer. When a part of the Ru layer is enlarged, as in Figure 2.13(d), the very smooth and uniform interface and surface structure can be confirmed. For this step coverage test, the Ta<sub>2</sub>O<sub>5</sub> layer cannot be used as the underlayer because the CVD Ta<sub>2</sub>O<sub>5</sub> cannot provide sufficiently high step coverage. In contrast, the ZrO<sub>2</sub> and TiN layers, both grown via ALD by a semiconductor device company, showed sufficient step coverage in the hole structure, as can be confirmed from the TEM images.

When the thickness uniformity across the 8-inch-diameter wafer was estimated using an identical showerhead-type process chamber, the ALD Ru film showed 5.6% non-uniformity, much lower than the 12.5% non-uniformity of the films with the same deposition recipe (8s-30s-10s-10s) in the pulsed CVD temperature region (data not shown).

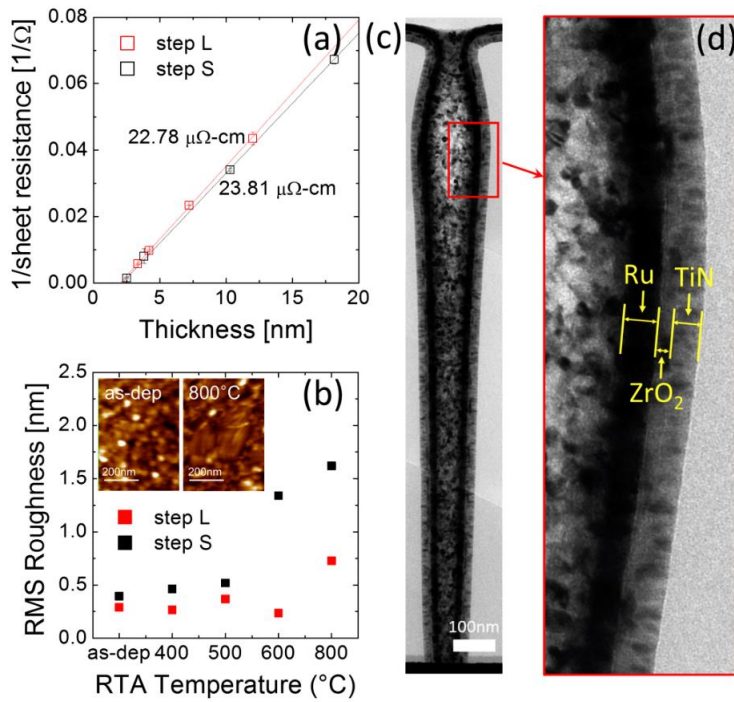


Figure 2.13 (a) Variations of the reciprocal sheet resistance of the Ru films grown on a Ta<sub>2</sub>O<sub>5</sub>/Si substrate with different N<sub>2</sub>/H<sub>2</sub> gas injection times as a function of the film thickness. (b) RMS roughness of the Ru films grown on a Ta<sub>2</sub>O<sub>5</sub>/Si substrate with different N<sub>2</sub>/H<sub>2</sub> gas injection times, and the variations after annealing at 400-800  $^{\circ}\text{C}$ . Inset figure (b) shows the surface AFM images of the as-deposited and 800  $^{\circ}\text{C}$ -annealed Ru films grown in step S. (c) Cross-sectional TEM image of the Ru film grown on a ZrO<sub>2</sub>/TiN hole structure with a long N<sub>2</sub>/H<sub>2</sub> gas injection time (opening diameter:  $\sim$ 100 nm; aspect ratio:  $\sim$ 20:1). (d) Enlarged image of (c), where ZrO<sub>2</sub>/TiN layers were grown by ALD.

## 2.4. Summary

Ru thin films were grown on Ta<sub>2</sub>O<sub>5</sub> and Au thin-film substrates through the ALD process, using the RuO<sub>4</sub> precursor and N<sub>2</sub>/H<sub>2</sub> mixed gas as the reducing agent. The influence of the substrate on the initial nucleation of Ru and the potential chemical reaction between the substrate and the incoming precursor or reducing gas were carefully examined. The most promising ALD temperature for stable Ru film growth was determined to be 165 °C for the given precursor and reactant. At temperatures higher than ~180 °C, the precursor decomposes thermally, and at an excessively low temperature (e.g., 140 °C), the chemical reactivity between RuO<sub>4</sub> and N<sub>2</sub>/H<sub>2</sub> gas will deteriorate, and a Ru-RuO<sub>2</sub> mixture film was obtained. Despite the general assumption of the inactive role of the stable oxide bottom layer (Ta<sub>2</sub>O<sub>5</sub>), such layer showed critical catalytic activity for RuO<sub>4</sub> adsorption and Ru film formation during ALD in this study. The Ta<sub>2</sub>O<sub>5</sub> film was reduced by its prolonged exposure to the N<sub>2</sub>/H<sub>2</sub> gas pulse, and the produced Ta atoms migrated towards the growing Ru film surface. In this system, two saturated growth region was observed with increasing the N<sub>2</sub>/H<sub>2</sub> gas injection time when the other ALD steps showed general self-limited growth behavior. The shorter (10 s) pulse time (the first saturation region, step S) of the N<sub>2</sub>/H<sub>2</sub> gas resulted in an insufficient OH- group concentration on the Ta<sub>2</sub>O<sub>5</sub> surface, which induced a long incubation period of eight cycles. This was accompanied by a more significant reduction of the Ta<sub>2</sub>O<sub>5</sub> layer during the subsequent ALD cycles, and by the induction of further

Ta atom migration, which finally resulted in a very high saturated bulk growth rate of 0.37 nm/cycle. The longer (20 s) pulse (the second saturation region, step L) produced a higher hydroxyl group concentration on the Ta<sub>2</sub>O<sub>5</sub> surface, which was accompanied by an incubation period of only two cycles. Therefore, rapid nucleation was achieved, which protected the Ta<sub>2</sub>O<sub>5</sub> layer from further reduction, and the Ta atom migration was less significant. As a result, a lower saturated bulk growth rate of 0.26 nm/cycle was achieved under this condition. These findings indicate that the involvement of the incubation cycles and the bulk growth rate must be carefully considered especially when an extremely thin film has been deposited. Such a peculiar growth behavior was not observed when the Au thin film was used as the substrate, which yielded no incubation cycles and a 0.22 nm/cycle bulk growth rate. These abnormal growth behaviors, however, did not influence the electrical properties of the film, and resistivity as low as 23 μΩ cm was achieved. Such a promising electrical property can be maintained down to an extremely low thickness of ~2.5 nm, which can be ascribed to the near-non-involvement of impurities such as carbon in the film.

## 2.5. Bibliography

- (1) Choi, S. -H.; Cheon. T.; Kim. S. -H.; Kang. D. -H.; Park. G. -S.; Kim. S. Thermal Atomic Layer Deposition (ALD) of Ru Films for Cu Direct Plating. *J. Electrochem. Soc.* **2011**, 158, D351-D356.
- (2) Mun, K. -Y.; Hong. T. E.; Cheon. T.; Jang, Y.; Lim. B. -Y.; Kim. S.; Kim. S.-H. The effects of nitrogen incorporation on the properties of atomic layer deposited Ru thin film as a direct-plateable diffusion barrier for Cu interconnect. *Thin Solid Films.* **2014**, 562, 118-125.
- (3) Jeong. H. J.; Kim. J. W.; Jang, D. Y.; Shim, J. H. Atomic layer deposition of ruthenium surface-coating on porous platinum catalysts for high-performance direct ethanol solid oxide fuel cells. *J. Power Sources.* **2015**, 291, 239-245.
- (4) Han, J. H.; Han, S.; Lee, W.; Lee, S. W.; Kim, S. K.; Gatineau, J.; Dussarrat, C.; Hwang, C. S. Improvement in the leakage current characteristic of metal-insulator-metal capacitor by adopting RuO<sub>2</sub> film as bottom electrode. *Appl. Phys. Lett.* **2011**, 99, 022901.
- (5) Kim, S. K.; Kim, W. -D.; Kim, K. -M.; Hwang, C. S. High dielectric constant TiO<sub>2</sub> thin films on a Ru electrode grown at 250°C by atomic-layer deposition. *Appl. Phys. Lett.* **2004**, 85, 4112-4114.

- (6) Kim, S. K.; Hwang, G. W.; Kim, W. -D.; Hwang, C. S. Transformation of the Crystalline Structure of an ALD TiO<sub>2</sub> Film on a Ru Electrode by O<sub>3</sub> Pretreatment. *Electrochem. Solid-State Lett.* **2006**, *9*, F5-F7.
- (7) Kim, S. K.; Lee, S. Y.; Seo, M.; Choi, G. -Y.; Hwang, C. S. Impact of O<sub>3</sub> feeding time on TiO<sub>2</sub> films grown by atomic layer deposition for memory capacitor applications. *J. Appl. Phys.* **2007**, *102*, 024109.
- (8) Kim, S. K.; Lee, S. W.; Han, J. H.; Lee, B.; Han, S.; Hwang, C. S. Capacitors with an Equivalent Oxide Thickness of < 0.5 nm for Nanoscale Electronic Semiconductor Memory. *Adv. Funct. Mater.* **2010**, *20*, 2989-3003.
- (9) Lee, S. W.; Han, J. H.; Han, S.; Lee, W.; Jang, J. H.; Seo, M.; Kim, S. K.; Dussarrat, C.; Gatineau, J.; Min, Y. -S.; Hwang, C. S. Atomic Layer Deposition of SrTiO<sub>3</sub> Thin Films with Highly Enhanced Growth Rate for Ultrahigh Density Capacitors. *Chem. Mater.* **2011**, *23*, 2227-2236.
- (10) Lee, W.; Jeon, W.; An, C. H.; Chung, M. J.; Kim, H. J.; Eom, T.; George, S. M.; Park, B. K.; Han, J. H.; Kim, C. G.; Chung, T.-M.; Lee, S. W.; Hwang, C. S. Improved Initial Growth Behavior of SrO and SrTiO<sub>3</sub> Films Grown by Atomic Layer Deposition Using {Sr(demamp)(tmhd)}<sub>2</sub> as Sr-Precursor. *Chem. Mater.* **2015**, *27*, 3881–3891.

- (11) Popovici, M.; Swerts, J.; Redolfi, B.; Kaczer, B.; Aoulaiche, M.; Radu, I.; Clima, S.; Everaert, J. -L.; Van Elshocht, S.; Jurczak, M. Low leakage Ru-strontium titanate-Ru metal-insulator-metal capacitors for sub-20nm technology node in dynamic random access memory. *Appl. Phys. Lett.* **2014**, 104, 082908.
- (12) Lee, J. -H.; Kim, J. -Y.; Rhee, S. -W.; Yang, D. Y.; Kim, D. -H.; Yang, C. -H.; Han, Y. -K.; Hwang, C. -J. Chemical vapor deposition of Ru thin films by direct liquid injection of Ru(OD)<sub>3</sub> (OD=octanedionate). *J. Vac. Sci. Technol., A* **2000**, 18, 2400-2403.
- (13) Aaltonen, T.; Ritala, M.; Arstila, K.; Keinonen, J.; Leskelä, M. Atomic Layer Deposition of Ruthenium Thin Films from Ru(thd)<sub>3</sub> and Oxygen, *Chem. Vap. Depos.* **2004**, 10, 215-219.
- (14) Aaltonen, T.; Alén, P.; Ritala, M.; Leskelä, M. Ruthenium Thin Films Grown by Atomic Layer Deposition. *Chem. Vap. Depos.* **2003**, 9, 45-49.
- (15) Yim, S. -S.; Lee, D. -J.; Kim, K. -S.; Kim, S. -H.; Yoon, T. -S.; Kim, K. -B. Nucleation kinetics of Ru on silicon oxide and silicon nitride surfaces deposited by atomic layer deposition. *J. Appl. Phys.* **2008**, 103, 113509.
- (16) Kim, S. K.; Lee, S. Y.; Lee, S. W.; Choi, G. -Y.; Hwang, C. S.; Lee, J. W.; Jeong, J. Atomic Layer Deposition of Ru Thin Films Using 2,4-

- (Dimethylpentadienyl)(ethylcyclopentadienyl)Ru by a Liquid Injection System. *J. Electrochem. Soc.* **2007**, 154, D95-D101.
- (17) Han, J. H.; Lee, S. W.; Choi, G. -J.; Lee, S. Y.; Hwang, C. S.; Dussarrat, C.; Gatineau, J. Chemical Vapor Deposition of Ru Thin Films with an Enhanced Morphology, Thermal Stability, and Electrical Properties Using a RuO<sub>4</sub> Precursor. *Chem. Mater.* **2009**, 21, 207-209.
- (18) Han, J. H.; Lee, S. W.; Kim, S. K.; Han, S.; Hwang, C. S.; Dussarrat, C.; Gatineau, J. Growth of RuO<sub>2</sub> Thin Films by Pulsed-Chemical Vapor Deposition Using RuO<sub>4</sub> Precursor and 5% H<sub>2</sub> Reduction Gas. *Chem. Mater.* **2010**, 22, 5700-5706.
- (19) Minjauw, M. M.; Dendooven, J.; Capon, B.; Schaekers, M.; Detavernier, C. Atomic layer deposition of ruthenium at 100°C using the RuO<sub>4</sub>-precursor and H<sub>2</sub>. *J. Mater. Chem. C.* **2015**, 3, 132-137.
- (20) Minjauw, M. M.; Dendooven, J.; Capon, B.; Schaekers, M.; Detavernier, C. Near room temperature plasma enhanced atomic layer deposition of ruthenium using the RuO<sub>4</sub>-precursor and H<sub>2</sub>-plasma. *J. Mater. Chem. C.* **2015**, 3, 4848-4851.
- (21) Gatineau, J.; Yanagita, K.; Dussarrat, C. A new RuO<sub>4</sub> solvent solution for pure ruthenium film depositions. *Microelectron. Eng.* **2006**, 83, 2248-2252.

- (22) Yuan, Z.; Puddephatt, R. J.; Low-Temperature Chemical Vapor Deposition of Ruthenium Dioxide from Ruthenium Tetroxide: A Simple Approach to High-Purity RuO<sub>2</sub> Films. *Chem. Mater.* **1993**, *5*, 908-910.
- (23) Methaapanon, R.; Geyer, S. M.; Lee, H. -B. -R.; Bent, S. F. The low temperature atomic layer deposition of ruthenium and the effect of oxygen exposure. *J. Mater. Chem.* **2012**, *22*, 25154-25160.
- (24) Jung, H. J.; Han, J. H.; Jung, E. A.; Park, B. K. Hwang, J. -H.; Son, S. U.; Kim, C. G.; Chung, T. -M.; An, K. -S. Atomic Layer Deposition of Ruthenium and Ruthenium Oxide Thin Films from a Zero-Valent (1,5-Hexadiene)(1-isopropyl-4-methylbenzene)ruthenium Complex and O<sub>2</sub>. *Chem. Mater.* **2014**, *26*, 7083-7090.
- (25) Austin, D. Z.; Jenkins, M. A.; Allman, D.; Hose, S.; Price, D.; Dezelah, C. L.; Conley, J. F. Jr. Atomic Layer Deposition of Ruthenium and Ruthenium Oxide Using a Zero-Oxidation State Precursor. *Chem. Mater.* **2017**, *29*, 1107-1115.
- (26) Greenwood, N. N.; Earnshaw, A. *Chemistry of the Elements*, 2nd edition; Butterworth-Heinemann, **1997**.
- (27) Popovici, M.; Groven, B.; Marcoen, K.; Phung, Q. M.; Dutta, S.; Swerts, J.; Meersschaut, J.; Van Den Berg, J. A.; Franquet, A.; Moussa, A.; Vanstreels, K.; Lagrain, P.; Bender, H.; Jurczak, M.; Van Elshocht, S.;

- Delabie, A.; Adelman, C. Atomic Layer Deposition of Ruthenium Thin Films from (Ethylbenzyl)(1-Ethyl-1,4-cyclohexadienyl) Ru: Process Characteristics, Surface Chemistry, and Film Properties. *Chem. Mater.*, **2017**, *29*, 4654-4666.
- (28) Song, S. J.; Lee, S. W.; Kim, G. H.; Seok, J. Y.; Yoon, K. J.; Yoon, J. H.; Hwang, C. S.; Gatineau, J.; Ko, C. Substrate Dependent Growth Behaviors of Plasma-Enhanced Atomic Layer Deposited Nickel Oxide Films for Resistive Switching Application. *Chem. Mater.* **2012**, *24*, 4675-4685.
- (29) Kim, S. K.; Han, J. H.; Kim, G. H.; Hwang, C. S. Investigation on the Growth Initiation of Ru Thin Films by Atomic Layer Deposition. *Chem. Mater.* **2010**, *22*, 2850-2856.
- (30) Ashcroft, S. J.; Schwarzmann, E. Standard Enthalpy of Formation of Crystalline Gold(III) Oxide. *J. Chem. Soc., Faraday Trans. 1.* **1972**, *68*, 1360-1361.
- (31) Chase, M. W. Jr. NIST-JANAF Thermochemical Tables, Fourth Edition, *J. Phys. Chem. Ref. Data*, Monograph 9. **1998**, 1-1951.
- (32) Barin, I. *Thermochemical Data of Pure Substances*, Part II; VCH: Weinheim, Germany, **1989**.

- (33) Wöll, C. Hydrogen adsorption on metal oxide surfaces: a reinvestigation using He-atom scattering. *J. Phys.: Condens. Matter.* **2004**, 16, S2981-S2994.
- (34) C, Y. -J.; Li, K.-C.; Lin, Y.-C.; Pan, F. -M.; A mechanistic study of hydrogen gas sensing by PdO nanoflake thin films at temperatures below 250°C. *Phys. Chem. Chem. Phys.*, **2015**, 17, 3039.
- (35) Vasilopoulou, M. The effect of surface hydrogenation of metal oxides on the nanomorphology and the charge generation efficiency of polymer blend solar cells. *Nanoscale.* **2014**, 6, 13726.
- (36) Kogler, M.; Köck, E. -M.; Bielz, T.; Pfaller, K.; Klötzer, B.; Schmidmair, D.; Perfler, L.; Penner, S. Hydrogen Surface Reactions and Adsorption Studied on Y<sub>2</sub>O<sub>3</sub>, YSZ, and ZrO<sub>2</sub>. *J. Phys. Chem. C.* **2014**, 118, 8435-8444.
- (37) Kim, S. K.; Han, S.; Kim, G. H.; Jang, J. H.; Han, J. H.; Hwang, C. S. Local Epitaxial Growth of Ru Thin Films by Atomic Layer Deposition at Low Temperature. *J. Electrochem. Soc.* **2011**, 158, D477-D481.
- (38) Knaut, M.; Junige, M.; Albert, M.; Bartha, J. W. In-situ real-time ellipsometric investigations during the atomic layer deposition of ruthenium: A process development from [(ethylcyclopentadienyl)(pyrrolyl)ruthenium] and molecular oxygen. *J. Vac. Sci. Technol., A.* **2012**, 01A151.

- (39) Hwang, C. S.; Joo, S. H. Variations of the leakage current density and the dielectric constant of Pt/(Ba,Sr)TiO<sub>3</sub>/Pt capacitors by annealing under a N<sub>2</sub> atmosphere. *J. Appl. Phys.* **1999**, 85, 2431-2436.

### **3. Improving electrical performance of ZAZ/TiN based MIM capacitor adopting ALD-grown Ru top electrode**

#### **3.1. Introduction**

Many high-dielectric-constant ( $k$ ) materials have been examined for capacitor application in the next-generation dynamic random access memory (DRAM). The most important requirements for a capacitor dielectric have been a higher dielectric constant for higher capacitance and a lower leakage current density ( $J$ ) to suppress the charge loss. In this regard, several high- $k$  materials, including  $\text{TiO}_2$ , Al-doped  $\text{TiO}_2$  (ATO), and  $\text{SrTiO}_3$  (STO), have been extensively studied as a promising candidate for the successor of the currently used  $\text{ZrO}_2/\text{Al}_2\text{O}_3/\text{ZrO}_2$  (ZAZ) dielectric film.<sup>[1-6]</sup> Improved electrical properties, such as low equivalent oxide thickness ( $t_{\text{ox}}$ ) and leakage current, can be achieved with the high- $k$  materials, but a relatively high physical thickness is inevitable due to their smaller bandgap, which results in generally lower band offsets with metal electrodes. This is a critical drawback of such high- $k$  materials because physical thickness ( $\sim 5$  nm) also became a critical requirement for the use of the dielectric layer in the extremely narrow gap between the storage nodes in DRAMs with a  $< 20$  nm design rule. Therefore, at present, finding another solution for the further scaling of the DRAM capacitor

with the conventional ZAZ dielectric material is strongly required. The most straightforward approach in this regard is further decreasing the ZAZ dielectric film thickness. The leakage current issue, however, which is accompanied by the reduction of the film thickness, is a critical obstacle to the adoption of this approach. This problem can be addressed by the use of several methods, including increasing the metal-insulator barrier height and reducing the trap density in the bulk and interface, which have been proven to be effective for reducing the  $J$  of the metal-insulator-metal (MIM) structure.<sup>[4,7-11]</sup>

Therefore, in this study, the electrical properties of the MIM structure with Ru adopted as a top electrode (TE) instead of the conventional TiN electrode were evaluated. The Ru metal is favorable for metal electrode application due to its relatively high work function ( $\sim 4.7$  eV, whereas that of the TiN is  $\sim 4.2 - 4.5$  eV depending on Ti:N ratio) and low resistivity ( $\sim 7 \mu\Omega \text{ cm}$ ). Moreover, Ru has better oxidation resilience than the conventional TiN electrode, and its oxidized phase,  $\text{RuO}_2$ , also conducts oxide, with an even higher work function ( $\sim 5.1$  eV).<sup>[12]</sup> Therefore, adopting Ru as a TE will be a feasible solution for the DRAM capacitor scaling with the conventional ZAZ dielectric material.

In this regard, the authors recently reported a detailed study on the comparison of the sputtered TiN, Ru, and TiN/Ru bilayer TEs on the electrical performance of the ZAZ film grown via atomic layer deposition (ALD).<sup>[9]</sup> It was reported that the Ru electrode suppressed the leakage current under both

bias conditions. The bilayer electrode further enhanced the film performance by scavenging the undesirable  $\text{TiO}_x$  layer at the BE interface, which increased the capacitance density. All the TEs, however, were grown through the sputtering method, which is not compatible with the three-dimensional structure of the DRAM capacitor. Therefore, in this work, the high functionality of Ru TE was further confirmed by adopting the production-worthy ALD process of the Ru film, which adopts  $\text{RuO}_4$  and  $\text{N}_2/\text{H}_2$  mixed gas as the Ru precursor and reactant gas, respectively. As the ALD method is based on the chemical reaction of the surface-absorbed precursor and reactant gas, it can affect the bulk or interface characteristics of MIM capacitors. Although  $\text{N}_2/\text{H}_2$  mixed gas can potentially reduce the absorbing  $\text{RuO}_4$  molecules and can adversely affect the ZAZ dielectric layer,  $\text{RuO}_4$  itself is a strong oxidizer, which makes the reduction negligible.<sup>[12-14]</sup> ALD-grown ZAZ films adopting  $\text{O}_3$  as the oxygen source, however, usually induces the formation of the undesirable  $\text{TiO}_x$  layer at the BE interface, and strong oxidizing molecules such as  $\text{RuO}_4$  can degrade the performance of the MIM capacitor. Also, the sputtered TE can be easily patterned into disc shapes to measure the electrical properties using a metal shadow mask, but ALD-grown Ru cannot be patterned into a TE using a simple method due to the precursor molecules' penetration of the area underneath the mask layer. In this case, the ALD-grown Ru layer must be chemically etched using plasma or  $\text{O}_3$  gas with the appropriate hard mask.<sup>[15]</sup> This utilizes the high volatility of the  $\text{RuO}_3$  and  $\text{RuO}_4$  byproducts of the reaction

between the thin Ru film and the highly reactive O<sub>3</sub> gas. These chemical reactions involved in the Ru TE fabrication process, however, can change the electrical properties of the ZAZ films. Therefore, this work examined the influences of all these chemical processes for fabricating Ru TE on the dielectric performances of the ZAZ thin film, through electrical and chemical analyses.

## 3.2. Experimental

ZAZ and TiN thin films were used as a dielectric layer and the BE of MIM capacitors, respectively. A 10-nm-thick TiN BE film was deposited on a 100-nm-thick SiO<sub>2</sub>/Si substrate through the reactive sputtering of the Ti target under the N<sub>2</sub>-plasma condition, using a commercial mass-production-worthy machine (Endura, Applied Materials, USA). Then the ZrO<sub>2</sub> and Al<sub>2</sub>O<sub>3</sub> layers were deposited on the substrate through thermal ALD, with tetrakis-ethylmethylamino-zirconium (Zr(N-(CH<sub>3</sub>)(C<sub>2</sub>H<sub>5</sub>))<sub>4</sub>, TEMAZ) and trimethylaluminum ((CH<sub>3</sub>)<sub>3</sub>Al, TMA) as the Zr and Al precursors, respectively, and O<sub>3</sub> as an oxygen source. The wafer temperature was set to 250°C for the ALD of both the ZrO<sub>2</sub> and Al<sub>2</sub>O<sub>3</sub> layers. The physical thickness of the ZAZ dielectric film in this figure was varied from 3.0 to 7.0 nm while the total Al<sub>2</sub>O<sub>3</sub>:ZrO<sub>2</sub> thickness ratio was kept constant at 5-7 % to optimize both capacitance and leakage current characteristics. More details about ZAZ films can be found elsewhere.<sup>[9]</sup> However, these films were either too insulating at the thicker thickness or too leaky at the thinner thickness to study the leakage current mechanism. Therefore, ZAZ film with Al<sub>2</sub>O<sub>3</sub>:ZrO<sub>2</sub> thickness ratio of 1-2 % was also deposited with a thickness of 8 nm to investigate the leakage current mechanism more accurately. A Ru electrode was grown through thermal ALD, using RuO<sub>4</sub> and 95% N<sub>2</sub>/5% H<sub>2</sub> as the Ru precursor and reduction gas, respectively, and the substrate temperature during the Ru ALD was 165°C. The

optimized ALD conditions were Ru precursor injection 8 s, Ar gas purge 30 s, 95% N<sub>2</sub>/5% H<sub>2</sub> gas injection 20 s, and Ar gas purge 10 s.<sup>[16]</sup> Under this condition, the Ru film growth rate was 0.26 nm/cycle, and 15 ALD cycles were performed to deposit a 3-nm-thick Ru film on the ZAZ films. The 3-nm-thick TiN TE film was deposited through reactive sputtering, using a pure Ti target and N<sub>2</sub> gas (CDS 5000, SNTTEK). An additional 50-nm-thick Pt TE was deposited onto the TE as a capping and contact layer via DC sputtering, using a pure Pt target, through a metal shadow mask with 300- $\mu$ m-nominal-diameter holes. While the patterning of the TiN/Pt TE can be readily achieved by adopting the just-mentioned shadow mask, the conformal nature of the ALD-grown Ru film did not allow it. Therefore, the blanket Ru film was dry-etched using O<sub>3</sub> as the etching gas (density: 250 gm<sup>-3</sup>) at a 250°C substrate temperature, where the Pt dots mentioned above were used as the hard mask for the O<sub>3</sub> etching process. Under this condition, 3 s was sufficient to remove the Pt-uncovered 3-nm-thick Ru layer. For the safe removal of the Ru layer, however, a 10 s O<sub>3</sub> etching time was adopted. For identifying the O<sub>3</sub> etching time effect, a sample with a 3 s O<sub>3</sub> etching time was also prepared. The schematic diagram of the Ru TE fabrication process is shown in Figure 3.1. Post-metallization annealing (PMA) of the MIM capacitor with a sputter-grown TiN TE was performed at 400°C for 30 minutes, at a 95% N<sub>2</sub>/5% O<sub>2</sub> atmosphere, using a tube furnace so that the MIM capacitor could recover from the damage it had incurred due to the sputtering process. The MIM capacitor with an ALD-grown Ru TE was also

annealed under the same condition, for comparison. The electrical characteristics of the MIM capacitor were measured using Hewlett-Packard 4140B and 4194A, for the capacitance-voltage ( $C-V$ ) and leakage current density-voltage ( $J-V$ ) curves, respectively. The  $t_{\text{ox}}$  value was calculated from the estimated capacitance of each sample ( $C_m$ ) using the  $t_{\text{ox}}=3.9\epsilon_0(A/C_m)$  relationship, where  $A$  is the TE area, whose precise value was estimated using an optical microscope. During the measurement of the electrical characteristics, a positive or negative voltage was applied to the TE while the BE was grounded. The interface of the dielectric and electrode layers was investigated via X-ray photoelectron spectroscopy (XPS, SIGMA PROBE, VG).

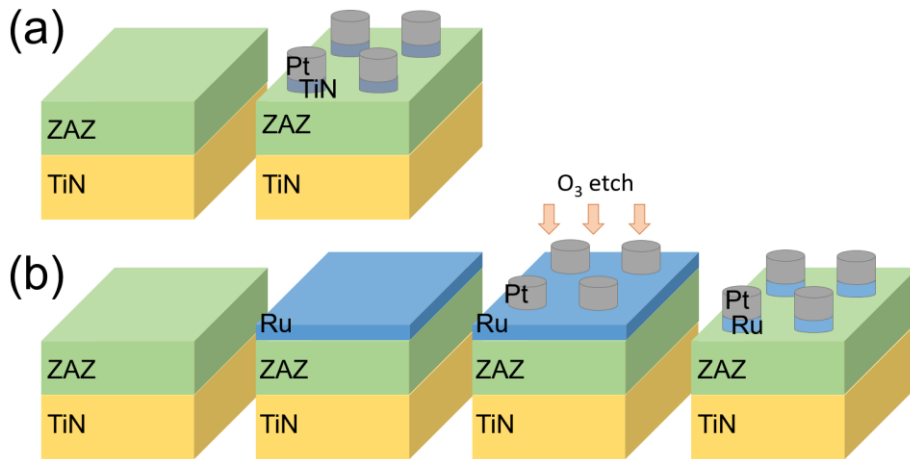


Figure 3.1 Scheme of the TE fabrication process: (a) TiN electrode; and (b) Ru electrode.

### 3.3. Results and Discussions

The leakage current density at +0.8 V vs. equivalent oxide thickness ( $J$ - $t_{\text{ox}}$ ) curve (Figure 3.2(a)) was evaluated in the MIM capacitors with a TiN or Ru TE. The  $t_{\text{ox}}$  values for the TiN and Ru TE samples were almost identical at the same physical thickness of the ZAZ film, and the calculated dielectric constants of the ZAZ layer were 24.8 and 23.6 with the TiN and Ru TEs, respectively. A significant improvement of the  $J$  value was observed, however, in the sample with a Ru TE compared to that with a TiN TE for the case of the 4.6-nm-thick ZAZ film. The  $J$  value at +0.8 V of the Ru TE sample was  $8.0 \times 10^{-9} \text{ A cm}^{-2}$ , which is  $>10^2$  times lower than that of the TiN TE sample ( $1.3 \times 10^{-6} \text{ A cm}^{-2}$ ). As a consequence, the minimum  $t_{\text{ox}}$  value of  $\sim 0.90 \text{ nm}$  was achieved with the Ru TE whereas that of the TiN TE sample was  $\sim 1.2 \text{ nm}$  from the interpolation where the  $J$  value could meet the required value for stable DRAM operation,  $<10^{-7} \text{ A cm}^{-2}$  at +0.8 V. Improvement in the leakage current property, however, obviously appeared only at the  $\sim 4.6 \text{ nm}$  ZAZ thickness. When the ZAZ film was 7.0 nm thick, the estimated leakage current was close to the detection limit of the equipment ( $\sim 0.1 \text{ pA}$ ) for both TE types, making the possible difference undetectable. When the ZAZ film was too thin ( $<4 \text{ nm}$ ), the excessively high leakage current via the tunneling-related mechanism also veiled the subtle difference; as such, the apparent difference in leakage was observed only near the  $\sim 4.6 \text{ nm}$  ZAZ thickness. The variations of  $J$  as a function of the applied

electrical field ( $J$ - $E$ ) characteristics of MIM capacitors were investigated to clarify the origin of the improved leakage current characteristic for the Ru TE case. Since the ALD Ru top electrode fabrication process was based on chemical reaction, any potential change could be present and influence on the electrical characteristics elsewhere so that the precise leakage current analysis is required.

Figure 3.2(b) shows the  $J$ - $E$  curves of the Ru/ZAZ/TiN and TiN/ZAZ/TiN samples for both the negative and positive bias regions. For this specific experiment, a slightly thicker ZAZ film (8.0 nm) with low Al<sub>2</sub>O<sub>3</sub> concentration was adopted to obtain the adequate current conduction level to analyze the current conduction mechanism. Additionally, the thinner ZAZ films in Figure 3.2(a) did not show sufficient reliability to repeatedly achieve the  $J$ - $E$  curves at various temperatures for analyzing the conduction mechanism. The leakage current analysis results achieved from this thicker film, however, can be applied to the case of thinner films (4.6 nm) as long as they are not too thin (<4 nm). The current density of the Ru/ZAZ/TiN sample was much lower than that of the TiN/ZAZ/TiN sample in both the negative and positive bias regions, but the difference was more evident in the positive bias region. In the negative bias region, the current density values of the Ru and TiN TE samples at an absolutely low-field region (<-0.4 MV cm<sup>-1</sup>) were similar. The current density of the TiN TE sample, however, started to increase rapidly from -0.4 MV cm<sup>-1</sup> whereas the current density of the Ru TE sample increased by less than one order of

magnitude up to  $-2.5 \text{ MV cm}^{-1}$ . This difference in  $J$  is supposed to have resulted from the difference in work function between the two TE layers because electrons were injected from the TE to the ZAZ layer in the negative-bias-applying condition; that is, the higher work function of Ru decreased the electron injection. The improvement of the ZAZ film itself, however, through the adoption of the Ru TE, had a critical contribution to the improvement, as discussed below.

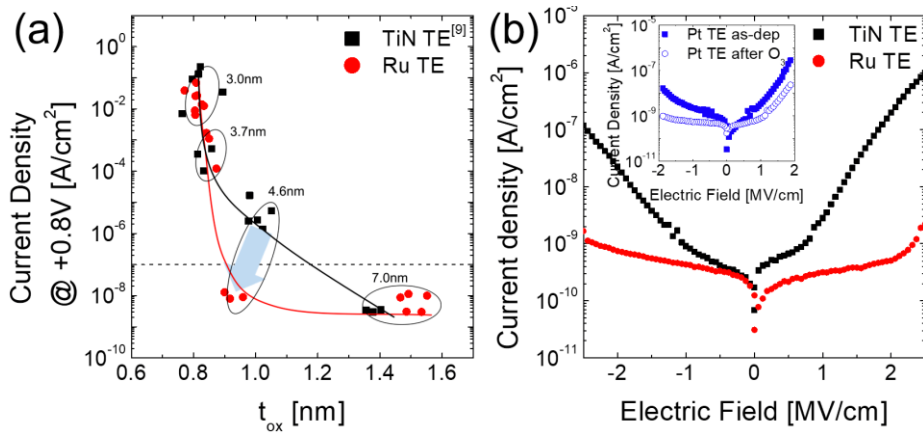


Figure 3.2 (a) Variations in  $J$  as a function of  $t_{ox}$  at a +0.8 V applied voltage. The solid lines were added for eye guidance. (b)  $J$ - $E$  characteristics of the MIM capacitors with different TEs. (inset)  $J$ - $E$  characteristics of the MIM capacitors with (opened) Pt TE and (closed) Pt TE and employing  $O_3$  treatment.

To investigate the leakage conduction mechanism in the 1-2 MV cm<sup>-1</sup> electric field region, which is the relevant region for the most critical 4.6 nm-thick films near 0.8 V, the  $J$ - $V$  characteristics of the TiN TE sample under both positive and negative biases were measured at temperatures (T) ranging from 303 to 363 K, and the results are shown in Figure 3.3(a) and (b). It can be seen that the TiN TE sample showed a large increase in  $J$ , with the increasing T suggesting the operation of a certain thermionic-emission mechanism, such as the Poole-Frenkel (P-F) emission or Schottky conduction mechanism.<sup>[17-22]</sup> The  $J$ - $V$  curves of the TiN TE sample were replotted according to P-F emission equation (1). From the best-linear-fitting of the variations in  $\ln (J/E)$  as a function of  $1000/T$  (K) at each T, the activation energy ( $E_a$ ) was calculated, and the values were plotted as a function of  $E^{1/2}$  in Figure 2.3(c) and (d). The data can be best-linear-fitted again according to equation (2), where the y-axis intercept of the extrapolated line corresponds to the trap depth ( $\varphi_0$ ) in the ZAZ film, and the slope gives the information of the optical dielectric constant ( $\epsilon_\infty$ ) of the ZAZ film.

$$J \propto E \exp \left( \frac{-\varphi_0 + \sqrt{\frac{3}{\pi\epsilon_0\epsilon_\infty} \frac{q^2 E}{kT}}}{kT} \right) = E \exp(-E_a/kT)$$

(1)

$$E_a = \varphi_0 - \sqrt{\frac{q^3/2E}{\pi\epsilon_0\epsilon_\infty}}$$

(2)

The abbreviations,  $q$ ,  $\epsilon_0$ ,  $k$ , and  $E_a$  were elemental charge, vacuum permittivity, Boltzmann constant, and activation energy, respectively. The obtained  $\phi_0$  and  $\epsilon_\infty$  from Figure 3.3(c) and (d) were 0.63 eV and 7.15 for the positive-bias-applying case, and 0.73 eV and 6.85 for the negative-bias-applying case. The optical dielectric constant were slightly higher than the theoretical value but were still consistent with the previous studies.<sup>[17-19, 21, 22]</sup> The same  $J$ - $V$  data were also fitted to the Schottky emission mechanism, but the extracted barrier height and optical dielectric constant values were unreasonable (1.79 eV and 0.57, respectively.) defying the correctness of the Schottky mechanism. These findings suggest that the ZAZ film with the TiN TE and BE contained a high density of defects, which might mediate the leakage current flow.

The temperature dependence of  $J$  of the Ru TE sample was similarly analyzed. Because the leakage current was very low within the voltage region from -2 V to 2 V, the  $J$ - $V$  curves were measured with a slightly higher maximum voltage (2.5 V) as shown in Figures 3.3 (e) and (f). The negative bias region  $J$ - $V$  still showed too low leakage current to apply any meaningful mechanism analysis, so only positive bias region data are presented. Although there was a temperature dependent current increase, both P-F and Schottky fitting failed to produce meaningful barrier height and dielectric constant. Instead, as shown in

Figure 3.3 (f), the  $J$ - $V$  data measured at 30 °C showed a feasible fitting to the Fowler-Nordheim tunneling mechanism at voltages higher than  $\sim 1.6$  V. This is critical evidence that the high defect density in the  $ZrO_2$  layer near the TiN BE was well cured by the  $O_3$  effect, and the Schottky barrier was increased at the BE interface. If the leakage current decrease effect was only due to the high work function of Ru TE compared with the TiN TE, such a large improvement in the leakage current under the positive bias region, which represents the property of the BE interface, could not be achieved. Besides, the very low leakage current under the negative bias region is a result of the combined effects of the high work function of Ru and defect curing.

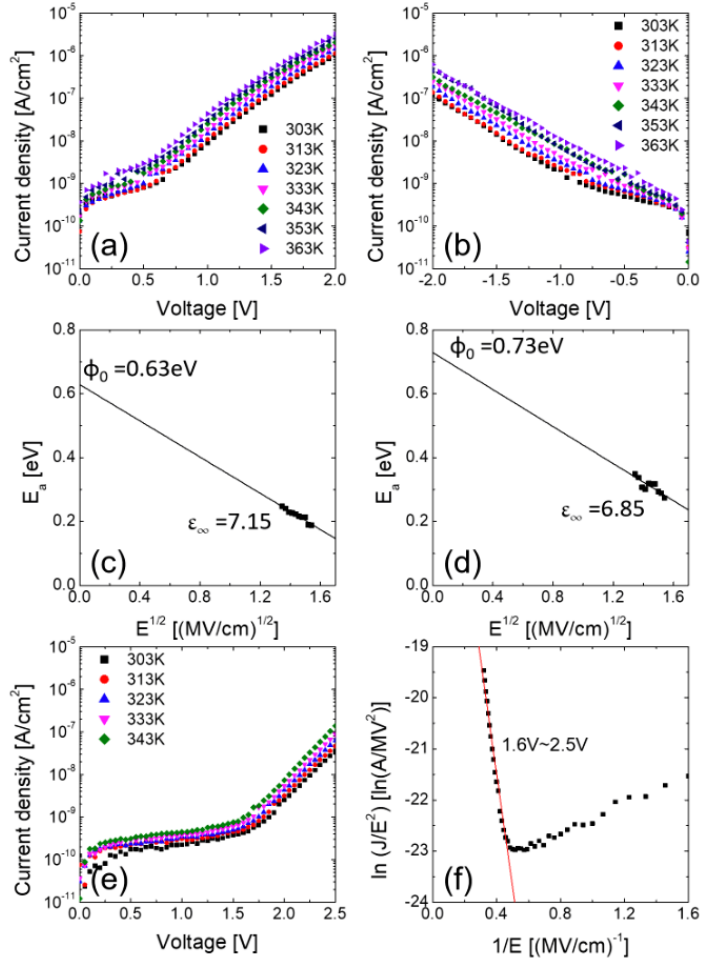


Figure 3.3 (a, b) Temperature dependence of the  $J$ - $V$  characteristics of the MIM capacitors with TiN TE at (a) positive and (b) negative biases. (c, d) Replotted plots from (c) figure 3a and (d) figure 3b according to the equation (2) for calculating the trap depth ( $\phi_0$ ) and the optical dielectric constant ( $\epsilon_\infty$ ) in the Poole-Frenkel emission. (e) Temperature dependence of the  $J$ - $V$  characteristic of the MIM capacitors with Ru TE at positive bias. (f) Transformed  $J$ - $V$  data in (e) for fitting to Fowler-Nordheim tunneling mechanism.

Although the leakage current at entire field region would be reduced by the high work function of Ru metal<sup>[9]</sup>, the results in Figure 3.3 implies that the defects, most probably oxygen vacancies ( $V_O$ ) inside the ZAZ layer, were cured during the Ru TE fabrication process. It will be shown that the  $O_3$  etching process decreased the  $V_O$  density especially near the BE interface by diffusion of oxygen atoms through the Pt/Ru TE layer. To further confirm the oxygen diffusion through the Pt/Ru TE layer and involvement of the defect curing effect, single layer Pt TE was fabricated using the same shadow mask. Since there was no Ru ALD layer was deposited, no  $O_3$ -etching process was necessary. However, to mimic the  $O_3$ -treatment and possible oxygen diffusion, the Pt/ZAZ/TiN sample was also treated under the identical  $O_3$  condition for 10 s. As shown in inset of Figure 3.2(b), the as-fabricated Pt/ZAZ/TiN sample showed high leakage current, which is only slightly lower than that of the TiN/ZAZ/TiN, but the  $O_3$ -treated Pt/ZAZ/TiN sample showed a much lower leakage current. This is clear evidence that the oxygen atoms have been penetrated through the Pt layer and cured the oxygen vacancies in the ZAZ layer. This experiment, in fact, indicated that the defect curing ( $V_O$  decrease) has an even higher significance than the work function of the electrode, given the fact that Pt has the highest work function among all the metals. The Ru layer underneath the Pt layer could have been oxidized to  $RuO_4$ , which must be the case for the Ru layer within the region which were not covered with Pt<sup>[23]</sup>, but this could not happen due to the coverage of the Pt. It seems that only limited

amount of dissociated oxygen atoms diffused through the 50 nm-thick Pt layer and reached the very thin Ru layer during the short etching time. If these oxygen atoms oxidized the Ru to RuO<sub>4</sub>, the void or pores from the covering Pt layer should be seen, which was not the case. It appears that most of the small amount of diffused oxygen atoms was consumed to fill in the oxygen vacancies in the ZrO<sub>2</sub> layer because the oxidation potential of Zr is much higher than that of Ru. Please note that the Ru layer was only 3 nm-thick making it very vulnerable to oxygen diffusion.

For further investigation of the variation in trap density according to the TE fabrication process, relative capacitance density vs. voltage ( $C/C_0-V$ ) characteristics was measured. In this case, all the ZAZ films were 8 nm thick. Figure 3.4 shows the  $C/C_0-V$  characteristics of capacitors with different TEs. The symmetrical TiN/ZAZ/TiN sample showed a highly asymmetric curve, but the asymmetrical Ru/ZAZ/TiN sample showed a symmetrical curve shape. In the ideal dielectric film, the capacitance should not vary with the applied voltage, but if the dielectric film of the MIM structure has a considerable amount of traps, the MIM structure will exhibit severe asymmetry or nonlinearity in the  $C/C_0-V$  curve.<sup>[24,25]</sup> The increasing capacitance with increasing dc bias is attributed to the increased contribution by the trap-detrap behavior at the defect near the interface between TiN BE and lower ZrO<sub>2</sub> layer. Under this circumstance, the electrons are trapped under the positive dc bias condition. These trapped electrons can respond to the ac inputs for the

capacitance measurement making the estimated capacitance increased. Under the negative bias, the trapped electrons strongly detrapped (or repelled) from the trap sites compared with no dc and positive dc bias case, making such contribution to the capacitance eliminated. Therefore, the capacitance under negative bias region decreases. If the top TiN/ZrO<sub>2</sub> interface contained a similar trap density, the top interface must trap electrons under the negative dc bias condition, which would increase the capacitance again. This was not the case, which confirms that only the bottom interface contains a high defect density. This is also consistent with the XPS results discussed below. In contrast, the Ru/ZAZ/TiN sample showed no such asymmetry, which corroborates the symmetrically low leakage current of the sample.

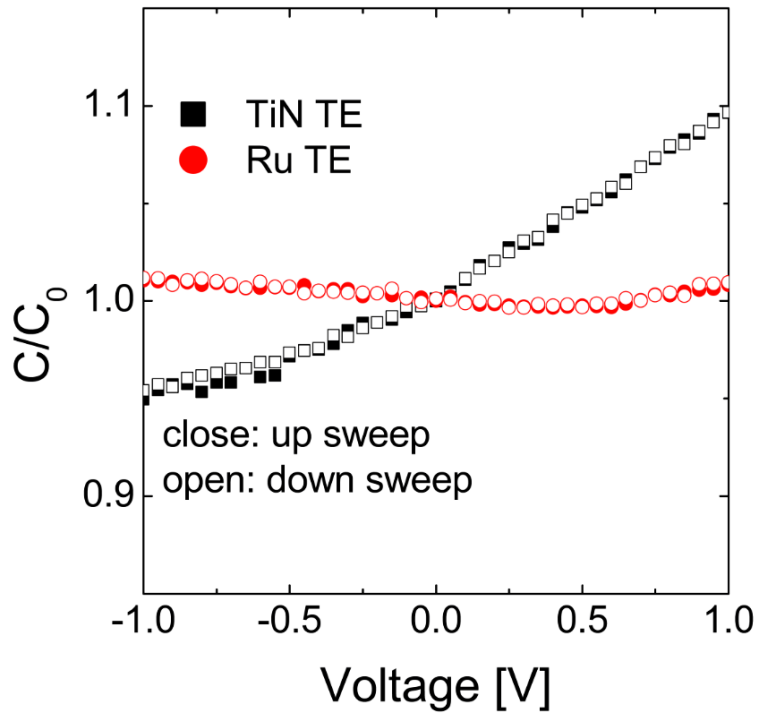


Figure 3.4  $C/C_0$ - $V$  characteristics of the MIM capacitors with different TEs at 10 kHz.

To investigate the influence of the Ru ALD and O<sub>3</sub> etching process on the chemical structure of the MIM capacitor, XPS analysis was performed. For this purpose, 2-nm-thick-Pt/3-nm-thick Ru stacked layer was grown on the 8-nm-thick ZAZ layer. The thickness of the Pt layer was decreased from 50 nm to 2 nm to avoid excessively long etching time in the XPS analysis chamber, which may damage the underlying ZAZ layer too much. Then, the sample was treated under the O<sub>3</sub> etching condition for 10 s, where the Ru layer was not etched away by the presence of the Pt cover layer. The untreated sample (as-deposited) was also examined by the XPS as the reference.

After the samples were loaded into the XPS chamber, the covering Pt/Ru layer and 1-2 nm of the top portion of the ZAZ layer was in-situ etched by the Ar<sup>+</sup> ion sputtering (with an acceleration voltage of 1 kV). The Zr 3d and Ti 2p XP spectra were achieved for the emission angles (0, 30, 45, and 60°). The ‘emission angle’ is the angle between the detector and the normal direction to the film surface. In this regard, the XP spectrum obtained in higher emission angle exhibits more surface sensitive result. Figure 3.5(a) – (d) show the Zr 3d XP spectra of the samples with the emission angles of 0, 30, 45, and 60°, where the black square and red dot symbols correspond to the as-deposited and the O<sub>3</sub>-treated samples, respectively. The two Zr 3d XPS spectra of the two samples with the 0° emission angle were deconvoluted as shown in Figures 3.5(e) and (f). Three kinds of peaks (ZrO<sub>2</sub>, oxygen-deficient ZrO<sub>2</sub> phase (ZrO<sub>2-x</sub>), and metallic Zr) were observed in both spectra at the 182.2, 180.9, and 179.4 eV

binding energies, respectively. The highly insulating properties of the ZAZ films with the Ru TE suggests that the involvement of metallic Zr in the Zr 3d XP spectra could originate from the sputtering process of the XPS analysis.<sup>[19,20]</sup> Therefore, this peak must be disregarded for both spectra. In contrast, the oxygen-deficient  $ZrO_{2-x}$  phase was induced by the reaction between the TiN BE and the lower  $ZrO_2$  layer during the ALD process of ZAZ dielectric.<sup>[26,27]</sup> Interestingly, the  $ZrO_{2-x}$  peak intensity was much lower for the  $O_3$ -treated sample compared with the as-deposited sample. When the emission angle was  $60^\circ$ , i.e., it is the most surface sensitive condition in this measurement, the intensities of the peaks other than  $ZrO_2$  largely decreased, with even more decrease for the case of the  $O_3$ -treated sample. These XPS analysis results indicated that the ZAZ film near the TiN BE had a higher density of defects (oxygen vacancies), which could be partially cured by the  $O_3$ -treatment. The formation of the oxygen vacancies could be most probably induced by the chemical reaction between the ZAZ layer and the TiN layer during ALD (or even after the film growth). The presence of  $ZrO_{2-x}$  is related to the presence of  $V_O$ , which can act as the traps within the ZAZ film.<sup>[28]</sup>

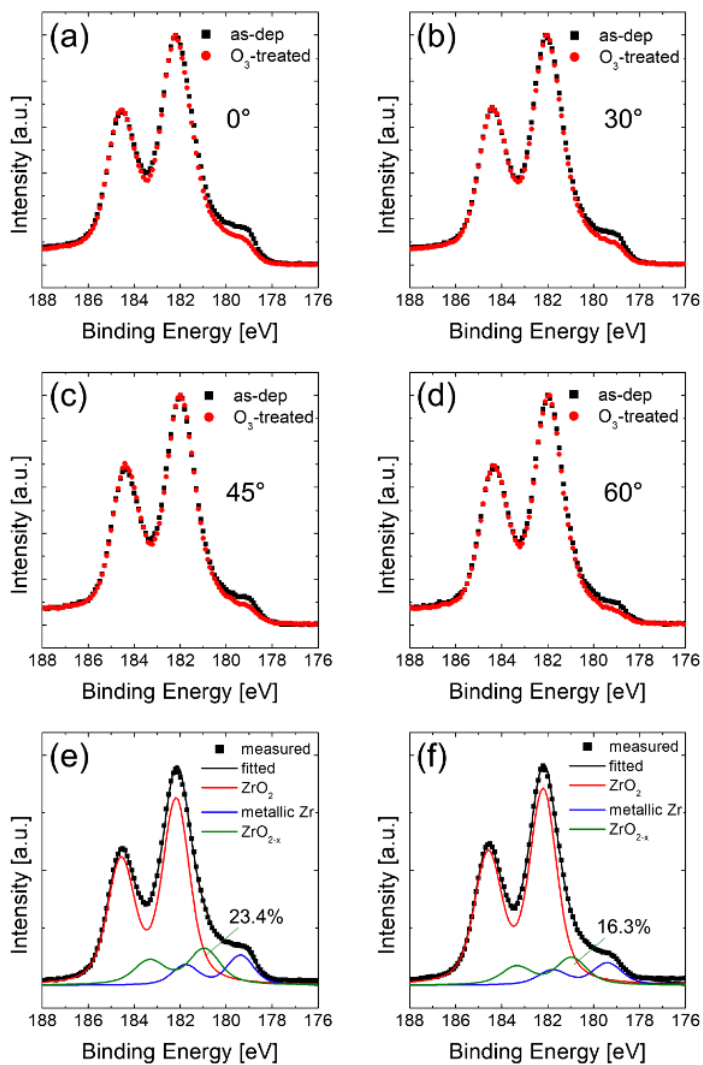


Figure 3.5 (a-d) Zr 3d angle-resolved XP spectra of the as-deposited (black) and O<sub>3</sub>-treated (red) Pt/Ru/ZAZ/TiN at different emission angle (a) 0°, (b) 30°, (c) 45° and (d) 60°. Deconvoluted peaks of the Zr 3d XP spectra of the (e) as-deposited Pt/Ru/ZAZ/TiN sample and (f) O<sub>3</sub>-treated Pt/Ru/ZAZ/TiN sample at 0° emission angle.

This could be supported by the Ti 2p XP spectra from the TiN BE of the two samples. Figure 3.6 shows the Ti 2p spectra from the two samples obtained at the 0° emission angle, where the black square and red dot symbols correspond to the as-deposited and the O<sub>3</sub>-treated samples, respectively. Due to the involvement of contributions from the Ti-N, Ti-O-N, and Ti-O bindings, the peak shapes were quite complicated, making the quantitative deconvolution tricky. However, the increased peak intensity near the binding energy of ~457.4 eV, which corresponds to the Ti-O bindings, of the O<sub>3</sub>-treated sample indicated that the TiN BE was slightly more oxidized. This finding corroborates the curing of the oxygen vacancy defects in the ZAZ layer shown in Figure 3.5. Therefore, the Ru ALD and the subsequent O<sub>3</sub> etching effectively filled in the V<sub>O</sub> with the oxygen atoms within the bulk of the ZAZ film. This is consistent with the findings from the electrical tests that were performed, especially from the *J-E* analysis, as shown in Figure 3.3.

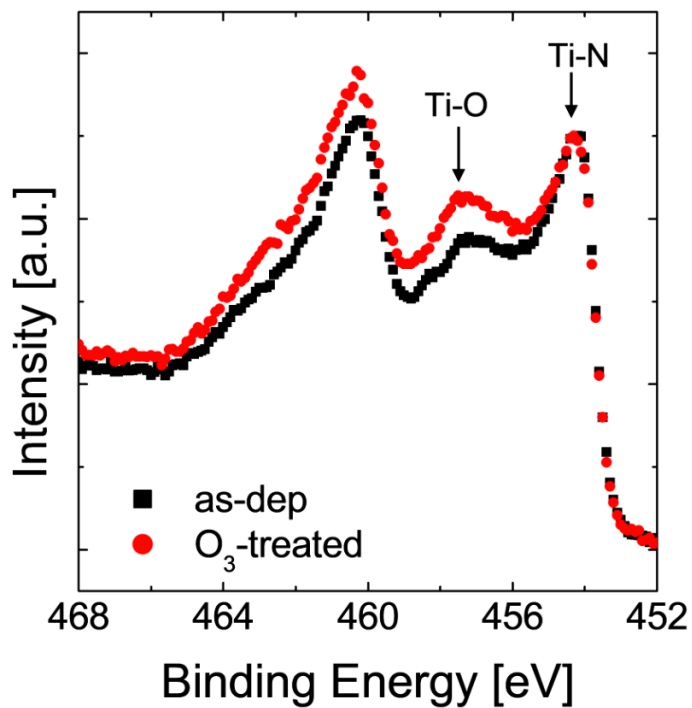


Figure 3.6 Ti 2p XP spectra of the as-deposited (black square) and O<sub>3</sub>-treated (red dot) Pt/Ru/ZAZ/TiN sample at 0° emission angle.

### 3.4. Summary

The electrical property changes of metal-insulator-metal (MIM) capacitors with a different top electrode (TE), atomic layer deposition (ALD)-grown Ru, or sputtered TiN but identical ZrO<sub>2</sub>/Al<sub>2</sub>O<sub>3</sub>/ZrO<sub>2</sub> (ZAZ) dielectric layers and TiN bottom electrodes (BEs), and their mechanism were investigated. In the leakage current density vs. equivalent oxide thickness ( $J$ - $t_{\text{ox}}$ ) curve, an improved minimum  $t_{\text{ox}}$  value (0.9 nm) was achieved with the Ru TE sample whereas it was 1.2 nm for the TiN TE sample, mainly due to the significant decrease in the leakage current for the specific thickness of ZAZ film of 4.6 nm. The higher work function of Ru compared with that of TiN can readily explain the leakage decrease in the entire electric field region. An even higher improvement in the leakage current performance, however, was achieved from the Ru TE sample in the specific electric field region of 1-2 MV cm<sup>-1</sup>, which is the region where the significant leakage current reduction of 4.6 nm-thick ZAZ film was achieved. The detailed conduction mechanism analysis of the TiN TE sample revealed that the current conduction in this region was mediated by the Poole-Frenkel mechanism, suggesting the presence of a high density of traps, which were most probably oxygen vacancies. The Ru etching processes using O<sub>3</sub> gas during the Ru TE fabrication decreased the defect concentration by filling in the V<sub>O</sub> with oxygen atoms. These were corroborated by the capacitance-voltage, and detailed X-ray photoelectron spectroscopy (XPS) analyses of the

Pt/Ru/ZAZ/TiN thin film stack before and after O<sub>3</sub>-treatment step. The fact that the enhancement in the MIM capacitor with ZAZ dielectric film achieved by the active oxygen effect can provide insightful viewpoints for the further scaling of next-generation DRAM device.

### 3.5. Bibliography

- [1] S. K. Kim, G. -J. Choi, S. Y. Lee, M. Seo, S. W. Lee, J. H. Han, H. -S. Ahn, S. Han, C. S. Hwang, *Adv. Mater.* **2008**, 20, 1429.
- [2] S. K. Kim, S. W. Lee, J. H. Han, B. Lee, S. Han, C. S. Hwang, *Adv. Funct. Mater.* **2010**, 20, 2989.
- [3] W. Lee, J. H. Han, W. Jeon, Y. W. Yoo, S. W. Lee, S. K. Kim, C. -H. Ko, C. Lansalot-Matras, C. S. Hwang, *Chem. Mater.* **2013**, 25, 953.
- [4] W. Jeon, S. H. Rha, W. Lee, Y. W. Yoo, C. H. An, K. H. Jung, S. K. Kim, C. S. Hwang, *ACS Applied Materials and Interfaces*, **2014**, 6, 7910.
- [5] W. Jeon, S. Yoo, H. K. Kim, W. Lee, C. H. An, M. J. Chung, C. J. Cho, S. K. Kim, C. S. Hwang, *ACS Applied Materials and Interfaces*, **2014**, 6, 21632.
- [6] M. J. Chung, W. Jeon, C. H. An, S. H. Kim, Y. K. Lee, W. Lee, C. S. Hwang, *ACS Applied Materials and Interfaces*, **2018**, 14, 8836.
- [7] S. A. Vitale, J. Kedzierski, P. Healey, P. W. Wyatt, C. L. Keast, *IEEE Trans. Electron Devices.* **2011**, 58, 419.
- [8] J. H. Han, S. Han, W. Lee, S. W. Lee, S. K. Kim, J. Gatineau, C. Dussarrat, C. S. Hwang, *Appl. Phys. Lett.* **2011**, 99.

- [9] W. Lee, C. H. An, S. Yoo, W. Jeon, M. J. Chung, S. H. Kim, C. S. Hwang, *Phys. Status Solidi RRL*. DOI: 10.1002/pssr.201800356.
- [10] M. Pešić, S. Knebel, K. Cho, C. Jung, J. Chang, H. Lim, N. Kolomiets, V. V. Afanas'ev, T. Mikolajick, U. Schroeder, *Solid-State Electronics*. **2016**, 115, 133.
- [11] W. Jeon, S. H. Rha, W. Lee, C. H. An, M. J. Chung, S. H. Kim, C. J. Cho, S. K. Kim, C. S. Hwang, *Phys. Status Solidi RRL*. **2015**, 9, 210.
- [12] J. H. Han, S. W. Lee, S. K. Kim, S. Han, C. S. Hwang, C. Dussarrat, J. Gatineau, *Chem. Mater.* **2010**, 22, 5700.
- [13] J. H. Han, S. W. Lee, G. -J. Choi, S. Y. Lee, C. S. Hwang, C. Dussarrat, J. Gatineau, *Chem. Mater.* **2009**, 21, 207.
- [14] J. H. Han, S. W. Lee, S. K. Kim, S. Han, W. Lee, C. S. Hwang, *Chem. Mater.* **2012**, 24, 1407.
- [15] M. Nakahara, S. Tsunekawa, K. Watanabe, T. Arai, T. Yunogami, K. Kuroki, *J. Vac. Sci. Technol. B*, **2001**, 19, 2133.
- [16] to be submitted
- [17] W. Weinreich, A. Shariq, K. Seidel, J. Sundqvist, A. Paskaleva, M. Lemberger, A. J. Bauer, *J. Vac. Sci. Technol.* **2013**, 31, 01A109

- [18] S. Knebel, U. Schroeder, D. Zhou, T. Mikolajick, G. Krautheim, *IEEE Trans. Device Mater. Rel.* **2014**, 14, 154.
- [19] W. Jeon, Y. Kim, C. H. An, C. S. Hwang, P. Gonon, C. Vallée, *IEEE Trans. Electron Devices.* **2018**, 65, 660.
- [20] W. Weinreich, R. Reiche, M. Lemberger, G. Jegert, J. Müller, L. Wilde, S. Teichert, J. Heitmann, E. Erben, L. Oberbeck, U. Schröder, A.J. Bauer, H. Ryssel, *Microelectronic Engineering.* **2009**, 86, 1826.
- [21] D. Martin, M. Grube, W. Weinreich, J. Müller, W. M. Weber, U. Schröder, H. Riechert, T. Mikolajick, *J. Appl. Phys.* **2013**, 113, 194103.
- [22] D. Zhou, U. Schroeder, J. Xu, J. Heitmann, G. Jegert, W. Weinreich, M. Kerber, S. Knebel, E. Erben, T. Mikolajick, *J. Appl. Phys.* **2010**, 108, 124104.
- [23] W. Jeon, W. Lee, Y. W. Yoo, C. H. An, J. H. Han, S. K. Kim, C. S. Hwang, *J. Mater. Chem. C.* **2014**, 2, 9993.
- [24] P. Gonon, M. Mougnot, C. Vallée, C. Jorel, V. Jousseau, H. Grampeix, F. El Kamel, *J. Appl. Phys.* **2010**, 107, 074507.
- [25] O. Khaldi, P. Gonon, C. Vallée, C. Mannequin, M. Kassmi, A. Sylvestre, F. Jomni, *J. Appl. Phys.* **2014**, 116, 084104.

- [26] S. Y. Lee, J. Chang, J. Choi, Y. Kim, H. J. Lim, H. Jeon, H. Seo, *Current Applied Physics*. **2017**, 17, 267.
- [27] A. Sinhamahapatra, J. -P. Jeon, J. Kang, B. Han, J. -S. Yu, *Sci. Rep.* **2016**, 6, 27218.
- [28] A. Paskaleva, W. Weinreich, A. J. Bauer, M. Lemberger, L. Frey, *Materials Science in Semiconductor Processing*, **2015**, 29, 124
- [29] P. Yang, D. Chao, C. Zhu, X. Xia, Y. Zhang, X. Wang, P. Sun, B. K. Tay, Z. X. Shen, W. Mai, H. J. Fan, *Adv. Sci.* **2016**, 3, 1500299.
- [30] S. Oktay, Z. Kahraman, M. Urgan, K. Kazmanli, *Applied Surface Science*, **2015**, 328, 255.

## **4. Improving conformality of SrRuO<sub>3</sub> thin films via controlling CVD-like growth behavior**

### **4.1. Introduction**

The deposition of perovskite-structured film has been studied in recent decades due to its various applications as functional oxide material, especially in electric, magnetic, energy field. Perovskite is a pseudocubic structure which has two kinds of cations, and the combination of two cations induce various perovskite materials, such as BaTiO<sub>3</sub>, CaRuO<sub>3</sub>, SrTiO<sub>3</sub>, etc. Among them, and SrRuO<sub>3</sub> (SRO) are nominated as electrode layer of next-generation DRAM capacitor with its high work function about 5.3eV, which is quite higher than conventional TiN electrode. Moreover, SRO has small lattice parameter mismatch with SrTiO<sub>3</sub> dielectric material, which has very high dielectric constant, so that it could be used as seed layer for in-situ crystallization of SrTiO<sub>3</sub> layer, as reported in previous reports<sup>[1-3]</sup>. In most studies, perovskite films are grown by Physical Vapor Deposition (PVD) method, especially Molecular Beam Epitaxy (MBE) or Pulsed Laser Deposition (PLD) since the purity and crystallinity of perovskite films are important on the functional properties of them<sup>[4-6]</sup>. By those methods, pure and well-crystallized films could be deposited, but they have limits on quite slow growth rate and poor conformality. Recently, most devices require smaller size and 3-dimensional structure, especially in DRAM capacitor, so that the method for conformal

growth of perovskite film should be developed. However, few studies about CVD or ALD growth of perovskite films have been reported. In case of SRO, the authors have studied the deposition method of SRO film by alternating ALD-grown SrO layers and CVD-grown RuO<sub>2</sub> layers<sup>[2]</sup>. Stoichiometric and crystallized SRO films with low impurity content could be deposited, but abnormal growth of SrO layers was also observed. The unintended growth behavior was induced from the oxygen-attracting nature of Sr precursor, as already reported. The CVD-like abnormal growth mechanism with Sr precursor could result in poor conformality, rough surface and low density so that it should be suppressed to gain conformal films. In studies about the growth of STO, various ideas such as insertion of barrier layer or variation of precursor were applied to lower the reactivity of Sr precursor and successfully controlled the growth behavior. However, unlike STO which abnormal growth behavior was observed in only initial stages, SRO film showed the CVD-like growth over the whole deposition process. In this study, the N<sub>2</sub>/H<sub>2</sub> gas injection step is added right after RuO<sub>2</sub> deposition step to reduce the amount of oxygen atom in RuO<sub>2</sub> layer, which are absorbed by following Sr precursor.

In addition, SRO/Pt bimetal electrodes were fabricated by growing SRO on Pt substrate. In previous study, bimetal electrode using Ru thin film was reported<sup>[7,8]</sup>. In that study, the thin Ru film could induce the in-situ crystallization of TiO<sub>2</sub> dielectric film, and the work function of bimetal electrode was modified with the thickness of Ru film.

## 4.2. Experimentals

The SrRuO<sub>3</sub> (SRO) films were grown on RuO<sub>2</sub> substrate, via alternating ALD-grown SrO layers and pulsed CVD-grown RuO<sub>2</sub> layers at growth temperature of 230°C. Sr(<sup>i</sup>Pr<sub>3</sub>Cp)<sub>2</sub> and O<sub>2</sub> gas were used as Sr precursor and reactant gas for depositing SrO layers while RuO<sub>4</sub> was used as Ru precursor for depositing RuO<sub>2</sub> layers. The Sr and Ru precursor canisters were kept at 110°C and 3°C, respectively. The SRO film was grown by repeating the super-cycles which consists of several SrO sub-cycles and RuO<sub>2</sub> sub-cycles. In previous reports, the RuO<sub>2</sub> sub-cycles consisted of two steps, RuO<sub>4</sub> feeding and Ar purge, while the modified deposition recipe included two additional steps, N<sub>2</sub>/H<sub>2</sub> feeding and Ar purge. The flow rate of bubbler Ar gas, purge Ar gas, O<sub>2</sub> gas and H<sub>2</sub> gas were 400sccm, 600sccm, 75sccm, and 100sccm, respectively. The detailed deposition parameters were reported in previous report. The scheme of deposition recipe is depicted in Fig.4.1. The areal density and cation composition were measured by X-ray fluorescence spectroscopy (XRF, Thermoscientific, ARL Quant'X), and the crystallinity of SRO films were investigated by glancing angle mode X-ray diffraction (GAXRD, PANalytical, X'pert Pro). The X-ray Photoemission Spectroscopy (XPS, SIGMA PROBE, VG) method was used to identify the chemical state of SRO films. The atomic depth profile of SRO films was investigated by Auger Electron Spectroscopy (AES), and the sheet resistance of films was measured by four-point probe

(4pp). SrRuO<sub>3</sub>/SrTiO<sub>3</sub>/Pt structure MIM capacitors were fabricated to investigate electric properties. SrTiO<sub>3</sub> (STO) dielectric films were grown on SRO bottom electrodes by ALD method using Sr(<sup>i</sup>Pr<sub>3</sub>Cp)<sub>2</sub> and O<sub>3</sub>, Ti source and Ti(CpMe<sub>5</sub>)(OMe)<sub>3</sub> as precursor and reactant gas for SrO layer and TiO<sub>2</sub> layer, respectively<sup>[9]</sup>. The Pt top electrode was deposited by DC sputtering method using pure Pt target. The electric performance of MIM capacitors using SRO bottom electrode was measured by Hewlett-Packard 4140B and 4194A.

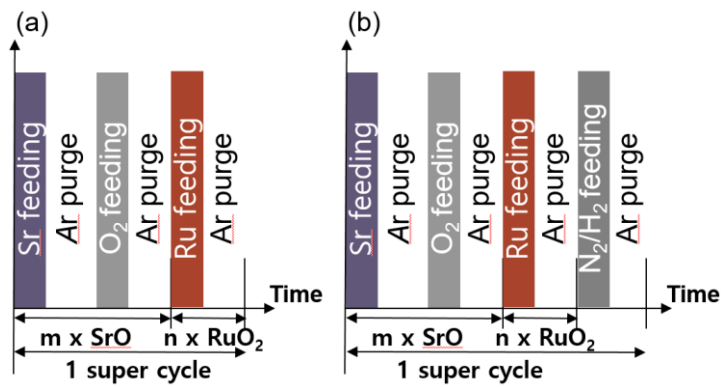


Figure 4.1 The deposition sequence of SrRuO<sub>3</sub> films in (a) original recipe (b) N<sub>2</sub>/H<sub>2</sub> injected (modified) recipe

### 4.3. Results and Discussions

The SrRuO<sub>3</sub> (SRO) films were grown via original sequence and N<sub>2</sub>/H<sub>2</sub> injected sequence (modified sequence). In modified sequence, the N<sub>2</sub>/H<sub>2</sub> purge time was fixed to 10s, and the N<sub>2</sub>/H<sub>2</sub> feeding time was varied from 1s to 10s. It was expected that the longer N<sub>2</sub>/H<sub>2</sub> feeding removed more oxygen atom from the RuO<sub>2</sub> layers. The variation of SrO layer density in SRO films with varying N<sub>2</sub>/H<sub>2</sub> feeding time was shown in figure 4.2. The SrO areal density decreased with increasing N<sub>2</sub>/H<sub>2</sub> feeding time, as expected, and saturated at certain level. It could be demonstrated that CVD-like growth behavior of SrO layer was suppressed by removing the oxygen atoms in RuO<sub>2</sub> layer. In the following experiments, the N<sub>2</sub>/H<sub>2</sub> feeding time was fixed to 3s.

The SrO : RuO<sub>2</sub> cycle ratio was varied and the SrO areal densities were measured in both recipes. In every cycle ratio, lower SrO areal densities were observed in modified sequence than original sequence due to the suppressed CVD-like growth behavior. Therefore, in original sequence without N<sub>2</sub>/H<sub>2</sub> injection, stoichiometric SRO film was grown at SrO : RuO<sub>2</sub> cycle ratio of 9:2, while more SrO cycles (12:2) were required to make stoichiometric SRO film in modified recipe. The variation of SrO areal density with cycle ratio was shown in figure 4.3.

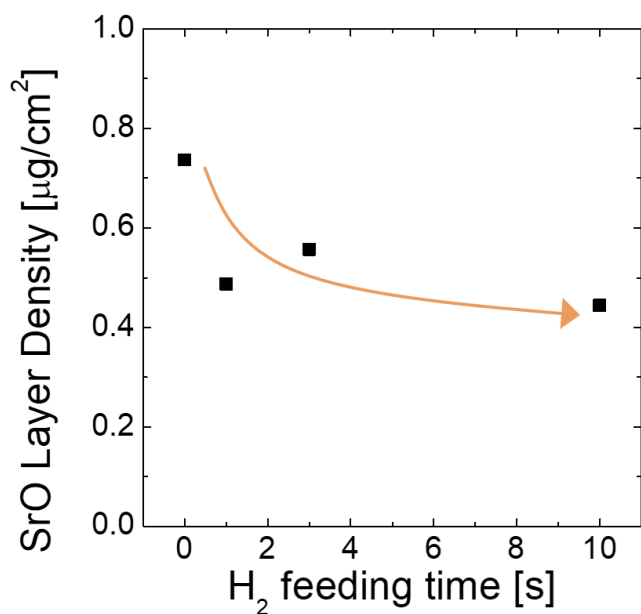


Figure 4.2 Variation of SrO areal density in SRO films as a function of  $\text{N}_2/\text{H}_2$  gas injection time

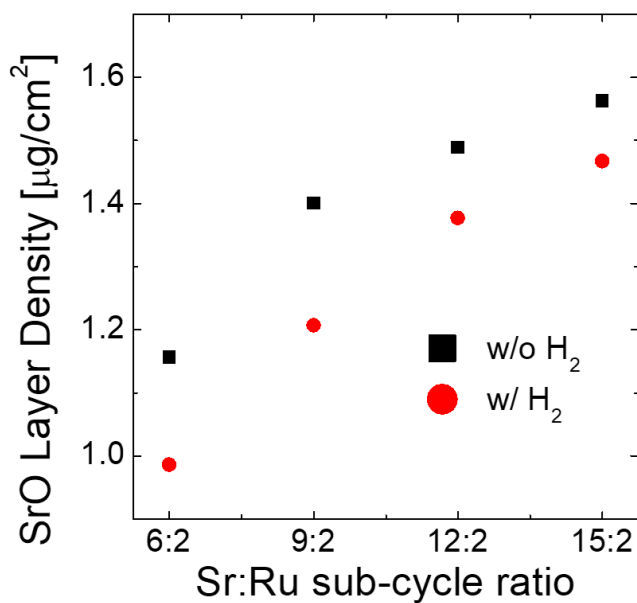


Figure 4.3 Variations of the SrO areal density in SRO films without or with  $\text{N}_2/\text{H}_2$  gas as a function of varying SrO : RuO<sub>2</sub> sub-cycle ratio

The atomic depth profile of SRO films in each recipe was investigated using SIMS analysis and the spectra were shown in Figure 4.4. The as-deposited SrRuO<sub>3</sub> films on RuO<sub>2</sub> substrates in each recipe were analyzed. The atomic concentration of Sr, Ru, and O atoms were constant through the entire SrRuO<sub>3</sub> films, which meant that the identical growth behavior was repeated in every cycle. In previous study of depositing SrTiO<sub>3</sub> films, the cation concentration was different in initial stage and steady-state stage since the CVD-like growth behavior was induced from the reaction of precursor and substrate. However, in SRO depositing process, the origin of CVD-like growth behavior was reaction of RuO<sub>2</sub> layer and following Sr precursors so that the cation concentration did not change through the depth.

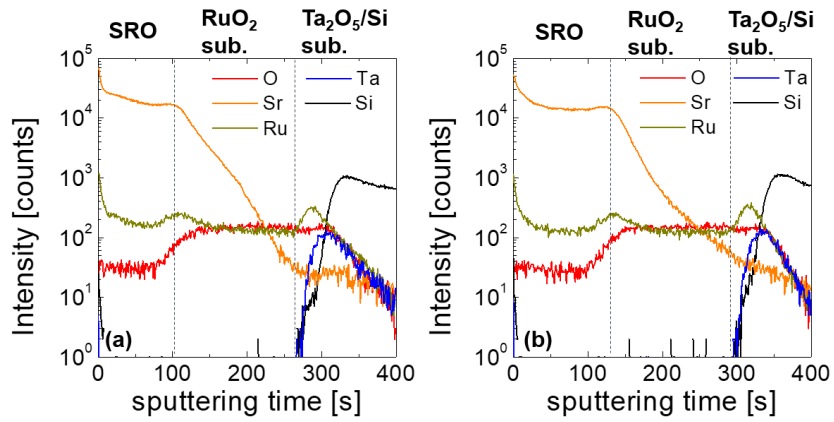


Figure 4.4 The SIMS depth profile of SRO films grown on RuO<sub>2</sub>/Ta<sub>2</sub>O<sub>5</sub>/Si substrate using (a) original recipe without H<sub>2</sub> (b) modified recipe with H<sub>2</sub>

The as-deposited SRO films on RuO<sub>2</sub> substrate were annealed (PDA) using conventional furnace, at 600 °C in N<sub>2</sub> atmosphere. The crystallization of SRO films in this condition was already reported in previous study<sup>[2]</sup>. The XRD spectra of SRO films in as-deposited state and annealed state, in both deposition recipes were shown in figure 4.5. Regardless of N<sub>2</sub>/H<sub>2</sub> injection, only peaks from RuO<sub>2</sub> substrate were shown in as-deposited state, and crystallized SRO (121) peak was observed at 32.2° after annealing process. The crystallographic property of SRO films was not affected on the deposition recipe.

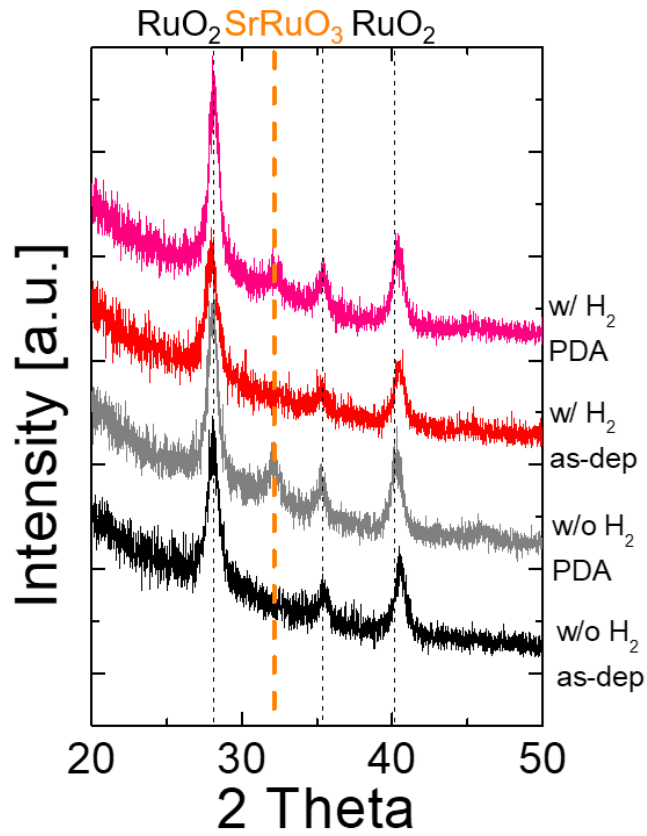


Figure 4.5 The GAXRD patterns of SRO films grown on RuO<sub>2</sub> substrate using recipes without or with H<sub>2</sub>, in as-deposited state and annealed state

Finally, the conformality of SRO films in both deposition sequence was investigated. As aforementioned, the CVD-like growth behavior in SRO film deteriorated the conformal growth of SRO films. It was not such problematic in planar films, but depositing conformal film was the first priority for DRAM capacitor. 15 nm-thick SRO films were deposited on trench hole structure with aspect ratio of 10:1, opening diameter of 100 nm. The SEM images of cross-section of trench hole were shown in figure 4.5 (a) and (b), in original sequence and modified sequence, respectively. In figure 4.5 (a), the thickness of SRO film on upper section was almost 15nm as intended, however, very thin SRO film ( $< 5\text{nm}$ ) was deposited on lower section. It could be thought that the Sr precursors did not transferred to lower section and the CVD-like growth occurred fluently on only upper section. In contrast, SRO film grown by  $\text{N}_2/\text{H}_2$  injected recipe showed better step coverage about 100%, in figure 4.5 (b). In upper section and lower section, the thickness of SRO film was both 15nm. It could be concluded that the CVD-like growth of Sr precursor was successively suppressed, and the Sr precursor moved to the bottom of the trench hole structure.

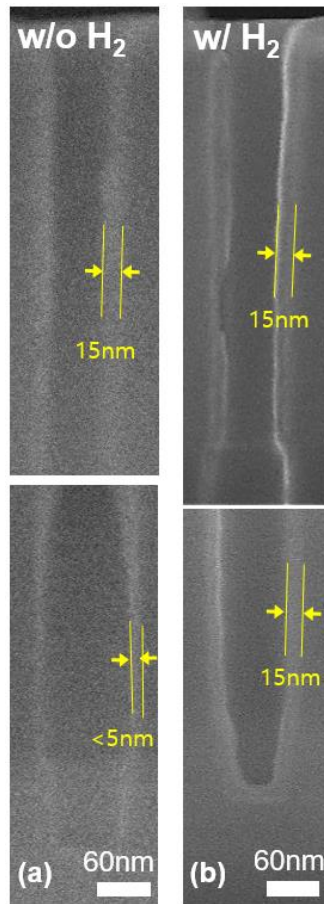


Figure 4.6 The cross-sectional SEM images of SRO films grown on trench hole structure using (a) original recipe without H<sub>2</sub> (b) modified recipe with H<sub>2</sub>. The aspect ratio and opening size of hole structure were 10:1 and 100 nm, respectively.

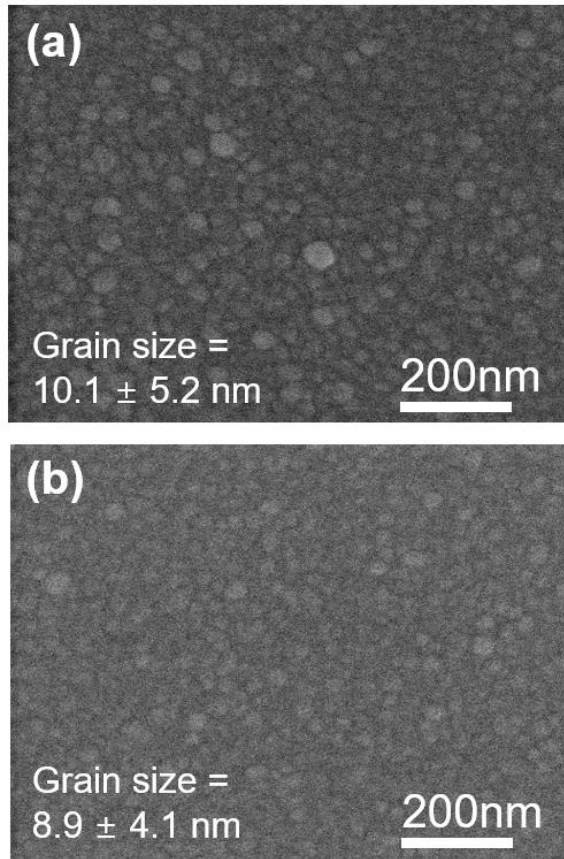


Figure 4.7 The plane view SEM images and the distribution of grain sizes of SRO films grown on RuO<sub>2</sub> substrate using (a) original recipe without H<sub>2</sub> (b) modified recipe with H<sub>2</sub>

The enhanced conformality could also be verified with the plane view SEM images of SRO films in each recipe. The grain sizes of SRO films were measured by the gwyddion software. In SRO film grown in original recipe, the CVD-like growth behavior resulted in the variation of grain size in wide range. ( $10.1 \pm 5.2$  nm) However, in  $N_2/H_2$  injected recipe, the grain sizes of SRO film were more constant. ( $8.9 \pm 4.1$  nm) It could be demonstrated that the suppressed CVD-like growth in modified recipe enabled the conformal growth.

The growth behavior, which was controlled by the  $N_2/H_2$  injection, was based on the removing oxygen from  $RuO_2$  layer so that the chemical state of SRO film should be investigated. In figure 4.7, the XP spectra of Ru 3d orbital of SRO films were investigated. The XP spectra of SRO films in as-deposited and annealed state were depicted. Since the  $N_2/H_2$  gas reduced the  $RuO_2$  layer and suppressed the CVD-like growth, the shrinkage of oxidized Ru phases was expected. However, the Ru 3d spectra of SRO films, in both as-deposited and annealed, were identical regardless of  $N_2/H_2$  injection. The identical Ru 3d spectra indicated that reduced  $RuO_2$  layers were oxidized again in following  $O_2$  injection step of SrO cycles. The peak deconvolution of each Ru 3d spectra was followed to identify the chemical state of SRO films in detail. In as-deposited state, almost Ru atoms were present in the form of Ru or  $RuO_2$  phases, and only little amount of SRO phase was detected. The amount of SRO phase was significantly increased through PDA process, which indicated that the SrO layers and  $RuO_2$  layers were mixed and SRO phase was formed.

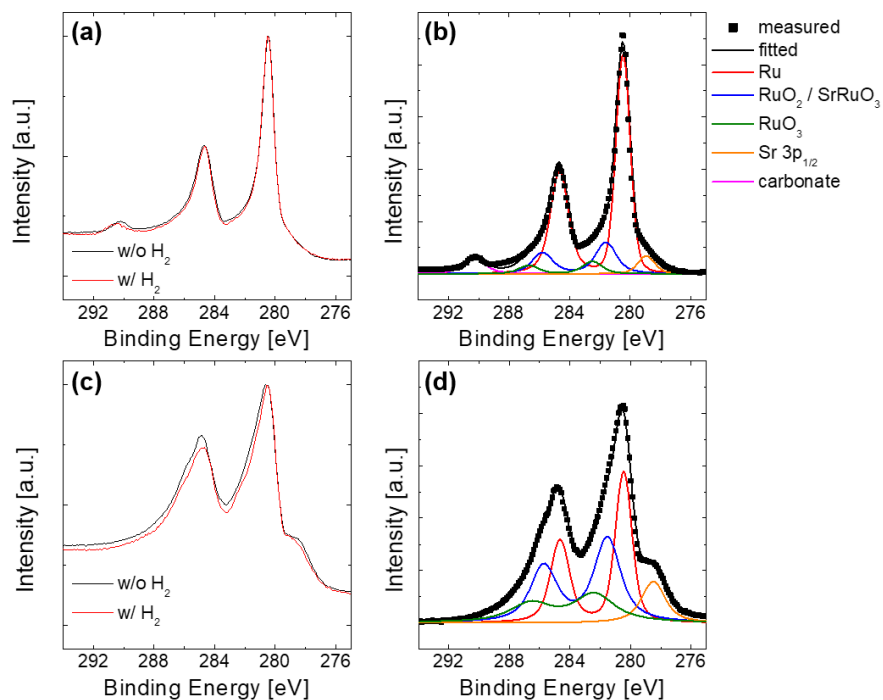


Figure 4.8 (a) The XP spectra of Ru 3d orbital of as-deposited SRO films grown by both recipes. (b) Peak deconvolution of XP spectra in (a). (c) The XP spectra of Ru 3d orbital of annealed SRO films grown by both recipes. (d) Peak deconvolution of XP spectra in (c).

The XP spectra of Sr 3d orbital of SRO films were also investigated and shown in figure 4.8. Significant difference with N<sub>2</sub>/H<sub>2</sub> injection gas was observed while Ru 3d XP spectra was identical in each deposition recipe. However, the trend that only Sr 3d XP spectra changed not Ru 3d XP spectra was not that interesting. Although the SrO layer itself was grown via ALD process, the growth behavior of SrO layer was based on the CVD-like growth. The SrO growth was dependent on the substrate so that the N<sub>2</sub>/H<sub>2</sub> injection on the RuO<sub>2</sub> layer could affect the chemical state of Sr atoms. In figure 4.8 (a) and (b), the XP spectra can be deconvoluted in two phases, SrO and amorphous SRO<sup>[4,10]</sup>. The amorphous SRO phase was Sr-Ru bond of uncrystallized form. The amorphous SRO peak was not present in pure SrO film so that it was induced from the CVD-like reaction of Sr precursor on RuO<sub>2</sub> layer. Therefore, the increase of SrO peak indicated that the CVD-like growth behavior was successfully suppressed by the N<sub>2</sub>/H<sub>2</sub> gas insertion. After the annealing, SrO peaks disappeared and crystalline SRO peaks were shown. It could indicate that every Sr atom was mixed into RuO<sub>2</sub> layers and crystallized to the SRO phase.

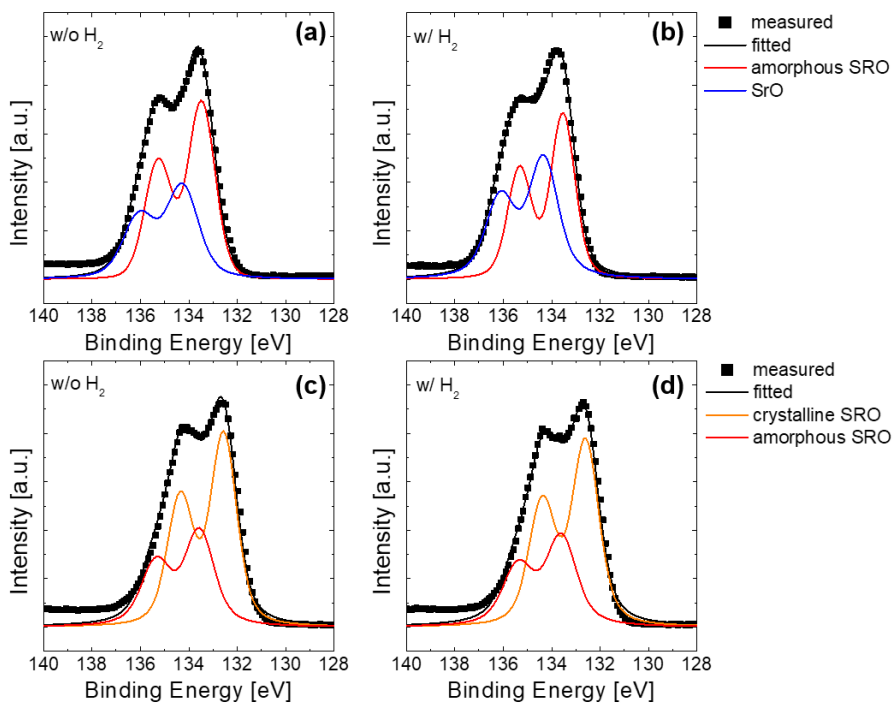


Figure 4.9 The XP spectra of Sr 3d orbital and peak deconvolution of (a) as-deposited SRO film grown by original recipe without H<sub>2</sub> (b) as-deposited SRO film grown by modified recipe with H<sub>2</sub> (c) annealed SRO film grown by original recipe without H<sub>2</sub> (d) annealed SRO film grown by modified recipe with H<sub>2</sub>

The SRO films were deposited on Pt substrate to fabricate bimetal electrode. The SrO : RuO<sub>2</sub> sub-cycle ratio was varied from 2:1 to 5:1, to deposit the stoichiometric SRO films. In figure 4.9, the variation of cation composition of SRO film on Pt substrate at various sub-cycle ratio was shown. Inset figures showed the SrO and Ru areal densities, respectively. Stoichiometric SRO film could be grown at sub-cycle ratio of 4:1, and the growth rate of SRO film on Pt substrate was 1.5 nm per supercycle. Various thickness of SRO films was deposited on Pt, and the surface roughness was investigated by the AFM. In figure 4.10, RMS roughness decreased with increasing SRO film thickness. It could indicate that the smoothly grown SRO film filled the valley between the Pt grain.

The SRO/Pt bimetal electrode was annealed using conventional furnace at N<sub>2</sub> atmosphere. In as-deposited state, peaks from Pt substrate were only detected. The films were not crystallized up to 600 °C, and crystallized SRO peak of 32° was observed at annealed temperature of 700 °C. In previous study, the decomposition of SRO films was already reported. The surface morphology of annealed 15 nm-SRO/Pt film was also measured and shown in figure 4.11 (b). The RMS roughness of film was 1.99 nm, increased with annealing but not that high.

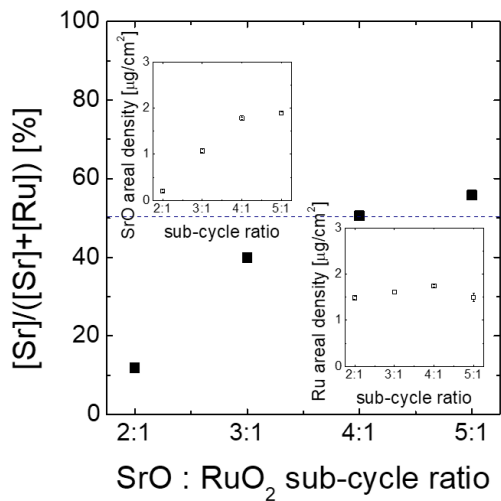


Figure 4.10 Variation of the Sr cation composition in SRO films as a function of SrO : RuO<sub>2</sub> sub-cycle ratio. Inset figures showed the variation of SrO and Ru areal densities as a function of sub-cycle ratio.

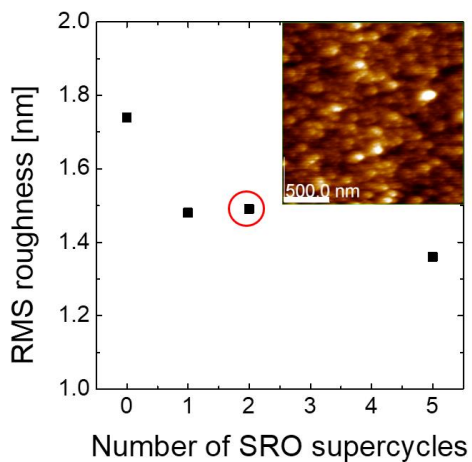


Figure 4.11 Variation of the RMS roughness of SRO films grown on Pt substrate as a function of the number of SRO supercycles. The inset figure showed the AFM image of the 2-supercycle SRO film grown on Pt substrate.

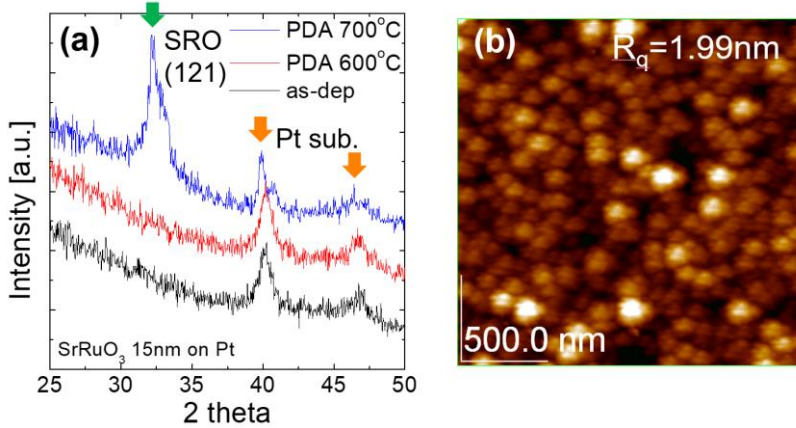


Figure 4.12 (a) The GAXRD patterns of SRO films grown on Pt substrate, in as-deposited and annealed at 600 °C or 700 °C. (b) The AFM image of the 15 nm-SRO/Pt annealed at 700 °C

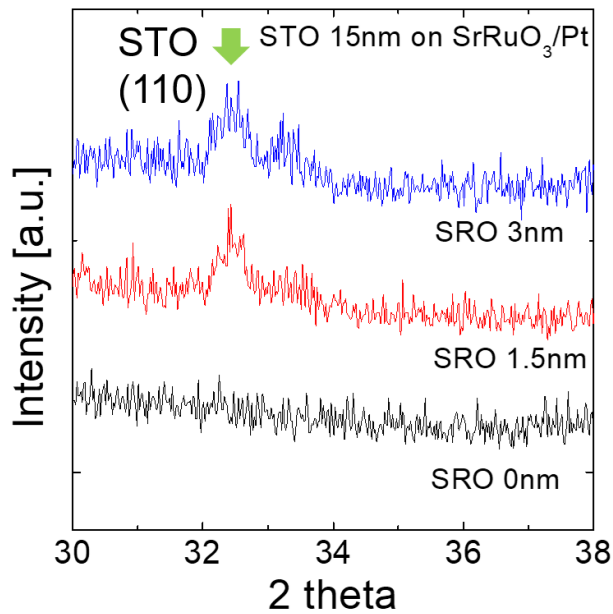


Figure 4.13 The GAXRD patterns of as-deposited STO on SRO/Pt bimetal electrodes. The thickness of SRO layer varied from 0 nm to 3 nm.

The STO dielectric films were grown on crystallized SRO/Pt bimetal electrode. The thickness of SRO films was varied from 0 nm to 3 nm, corresponding to 0 to 2 supercycles, and STO thickness was fixed to 15 nm. The detailed STO deposition condition was mentioned in experimental section. The GAXRD patterns of STO films on various thickness of SRO/Pt bimetal electrodes were shown in figure 4.12. STO film on pure Pt substrate did not in-situ crystallized, but crystallized STO peak at  $32^\circ$  was observed when STO was grown on SRO/Pt, even 1.5 nm thickness of SRO. Therefore, STO dielectric film could be in-situ crystallized with very thin SRO layer on Pt.

The variation of work function of SRO/Pt bimetal electrodes was measured by the UPS. As shown in figure 4.13, the work function of SRO/Pt bimetal electrode was lower than that of only Pt electrode. the 1.5 nm-SRO/Pt bimetal electrode had 0.3 eV lower work function than Pt, while 0.4 eV lower work function was measured at thicker SRO/Pt electrode. It could be demonstrated that the 3 nm-SRO film was sufficient to screen the work function of Pt electrode. Therefore, SRO/Pt bimetal electrode could have higher work function than only SRO electrode if adequate thickness of SRO was selected. The electrical characteristics of STO/SRO/Pt capacitors should be measured to determine the effect of bimetal electrode in detail, but it was not conducted in this study. The evaluation of electrical characteristics of STO dielectric film on SRO/Pt bimetal electrode would be a promising goal for another study.

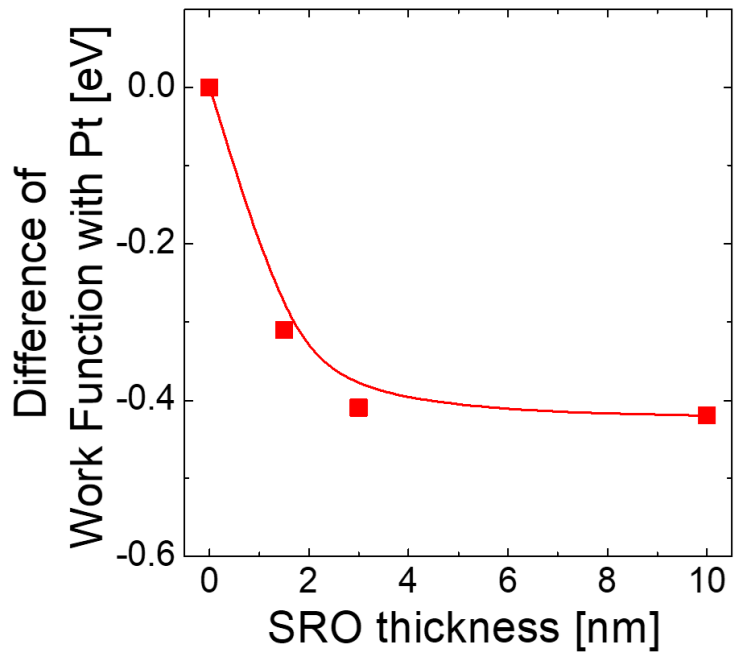


Figure 4.14 Variation of the difference of work function with only Pt substrate as a function of SRO thickness on Pt substrate.

## 4.4. Summary

In this study, SrRuO<sub>3</sub> (SRO) films were deposited via the modified deposition sequence which including the N<sub>2</sub>/H<sub>2</sub> gas injection step. The injected N<sub>2</sub>/H<sub>2</sub> gas removed the oxygen in RuO<sub>2</sub> layers which was origin of the CVD-like growth behavior of Sr precursor. The SrO areal density in SRO film grown with N<sub>2</sub>/H<sub>2</sub> gas was lower than that of SRO grown without N<sub>2</sub>/H<sub>2</sub> gas, and the higher SrO : RuO<sub>2</sub> sub-cycle ratio was required to obtain stoichiometric SRO films. The modification of deposition sequence did not affect the depth profile and crystallization of SRO films, but only improved the conformality of SRO films. The better step coverage of SRO films on trench hole structure and uniform grain sizes could be achieved from the modified sequence which successfully controlling CVD-like growth behavior. The chemical state of each Ru and Sr atoms were investigated by the XPS analysis, and the unexpected result that only Sr XP spectra was changed not Ru 3d spectra, was shown. It could be determined that RuO<sub>2</sub> layers were reduced by N<sub>2</sub>/H<sub>2</sub> and re-oxidized by following O<sub>2</sub> gas in SrO ALD cycles. In contrast, growth of SrO layers was affected by the substrate, the controlling growth behavior changed the bonding state of Sr atoms. Moreover, the SRO/Pt bimetal electrodes were fabricated to complement the defect of SRO electrode. Stoichiometric SRO films with smooth surface could be deposited on Pt substrate. SRO films on Pt substrate crystallized into perovskite structure at temperature of 700 °C, and SrTiO<sub>3</sub> dielectric film was also in-situ crystallized onto the SRO/Pt bimetal electrode.

Finally, the work function of SRO/Pt bimetal electrode varied with the thickness of SRO layers. Higher work function than only SRO electrodes could be achieved when SRO/Pt bimetal was fabricated with the adequate thickness of SRO layer.

## 4.5. Bibliography

1. J. -H. Ahn, J. -Y. Kim, J. -H. Kim, J. -S. Roh, S. -W. Kang, *Electrochem. Solid-State Lett.*, **2009**, 12, G5
2. J. H. Han, W. Lee, W. Jeon, S. W. Lee, C. S. Hwang, *Chem. Mater.*, **2012**, 12, 4686
3. S. Kupke, S. Knebel, U. Schroeder, S. Schmelzer, U. Bottger, T. Mikolajick, *IEEE EDL*, **2012**, 33, 1699
4. J. S. Sim, S. J. S. Zhao, H. J. Lee, K. Lee, G. W. Hwang, C. S. Hwang, *J. Electrochem. Soc.*, **2006**, 153, C777
5. D. Yang, X. Tang, R. Wei, Z. Hui, W. Song, X. Zhu, Y. Sun, *Journal of Alloys and Compounds*, **2016**, 682, 154
6. S. K. Singh, M. R. Lees, R. K. Singh, S. B. Palmer, *J. Phys. D: Appl. Phys.* **2002**, 35, 2243
7. G. -J. Choi, S. K. Kim, S. Y. Lee, W. Y. Park, M. Seo, B. J. Choi, C. S. Hwang, *J. Electrochem. Soc.*, **2009**, 156, G71
8. S. K. Kim, S. Han, W. Jeon, J. H. Yoon, J. H. Han, W. Lee, C. S. Hwang, *ACS Appl. Mater. Interfaces*, **2012**, 4, 4726
9. W. Lee, S. Yoo, W. Jeon, Y. W. Yoo, C. H. An, M. J. Chung, H. J. Kim, S.

W. Lee, C. S. Hwang, *Thin Solid Flms*, **2015**, 589, 723

10. A. Ito, H. Masumoto, T. Goto, *Mater. Trans.*, **2006**, 47, 2808

## 5. Conclusion

The introduction of Ru-based electrode materials for next-generation DRAM capacitor devices is inevitable since the scaling of the capacitor is such challenging due to its leakage current issue. The high work function of Ru-based electrodes could suppress the leakage current of DRAM capacitor so that depositing those materials via ALD-based process for the thin and conformal film is of interest. Many studies reported on the CVD or ALD methods of Ru-based materials using various kinds of Ru precursors. However, most studies used the MO precursors, which induced the carbon contamination or nucleation delay in the initial growth stage. Therefore, in this study, the growth and electrical characteristics of Ru-based electrode materials using RuO<sub>4</sub> precursor, which was not MO precursor, is investigated.

First, the ALD growth behavior of Ru metal films on metal-oxide substrates was investigated. Unlike general ALD behavior, the two step-saturation behavior versus N<sub>2</sub>/H<sub>2</sub> reductant gas injection time was observed when Ru metal films were deposited onto the Ta<sub>2</sub>O<sub>5</sub> substrate. Only pure Ru metal films were grown in each saturated step so that the extraordinary growth behavior was considered as the substrate-dependent mechanism, not the change of phases. The nucleation delay and growth rate of Ru metal films in each step were also affected by the N<sub>2</sub>/H<sub>2</sub> injection time. The possible mechanism based

on the reduction and diffusion of the Ta<sub>2</sub>O<sub>5</sub> substrate material was established to explain the growth behavior. The amount of hydroxyl group on Ta<sub>2</sub>O<sub>5</sub> surface and reduced amount of Ta<sub>2</sub>O<sub>5</sub> substrate were different at each N<sub>2</sub>/H<sub>2</sub> injection step. The reduced Ta<sub>2</sub>O<sub>5</sub> substrate, Ta metal, enhanced the adsorption of RuO<sub>4</sub> precursor and increased the growth rate. The unique growth mechanism did not change the physical and electrical characteristics of Ru metal films. The high step coverage about 100% was obtained at a trench hole structure with an aspect ratio of 20:1, opening size of 100 nm. Furthermore, the Ru metal thin film could be conformally deposited on the deeper hole structure, aspect ratio of 40:1 and opening size of 40 nm.

The developed Ru metal ALD process was adopted for the top electrode of the ZAZ/TiN capacitor. The patterning process of Ru top electrode film followed to measure the electrical characteristics since the ALD-grown Ru film fully covered the ZAZ surface. The sputter-grown TiN top electrode, which was conventional electrode material, was selected for comparison. The leakage current of the Ru/ZAZ/TiN capacitor was significantly improved than the TiN/ZAZ/TiN capacitor. The enhanced electrical characteristics resulted from not only the high work function of Ru metal than TiN, also the recovering oxygen vacancies in ZAZ dielectric film during Ru top electrode patterning process.

Finally, the SrRuO<sub>3</sub> electrode material was also investigated in two aspects. In the CVD/ALD combined deposition process of SRO electrode, the CVD-like growth behavior of SrO layers based on the oxygen atoms from the RuO<sub>2</sub> layer, was shown. To suppress the CVD-like growth behavior, N<sub>2</sub>/H<sub>2</sub> reduction gas injection step followed the RuO<sub>2</sub> layer deposition step, and it successfully controlled the CVD-like behavior. The conformality of SRO films was significantly improved via the modified deposition sequence, which removed the oxygen atoms in RuO<sub>2</sub> layers. The crystallinity of SRO film did not vary with N<sub>2</sub>/H<sub>2</sub> injection, but the chemical state of Sr atoms were changed not Ru atoms. SRO/Pt bimetal electrode was also fabricated by depositing SRO film on Pt substrate to compensate for the defect of the SRO electrode. Through the post deposition annealing process, SRO layer on Pt crystallized into perovskite structure and acted as a seed layer for in-situ crystallization of SrTiO<sub>3</sub> dielectric film. Moreover, the work function of the SRO/Pt bimetal electrode was higher than only SRO electrode so that the improvement of leakage current property would be expected.

# List of publications

---

## 1. Refereed Journal Articles (SCI)

### 1.1 Domestic

### 1.2. International

1. Woojin Jeon, Sang Ho Rha, Woongkyu Lee, Yeon Woo Yoo, **Cheol Hyun An**, Kwang Hwan Jung, Seong Keun Kim, and Cheol Seong Hwang, “Controlling the Al-Doping Profile and Accompanying Electrical Properties of Rutile-Phased TiO<sub>2</sub> Thin Films”, ACS Applied Materials and Interfaces, 6, 7910-7917 (2014)
2. Woojin Jeon, Woongkyu Lee, Yeon Woo Yoo, **Cheol Hyun An**, Jeong Hwan Han, Seong Keun Kim, and Cheol Seong Hwang, “Chemistry of active oxygen in RuO<sub>x</sub> and its influence on the atomic layer deposition of TiO<sub>2</sub> films”, Journal of Materials Chemistry C, 2, 9993-10001 (2014)
3. Woojin Jeon, Sijung Yoo, Hyo Kyeom Kim, Woongkyu Lee, **Cheol Hyun An**, Min Jung Chung, Cheol Jin Cho, Seong Keun Kim, and Cheol Seong Hwang, “Evaluating the Top Electrode Material for Achieving an Equivalent Oxide Thickness Smaller than 0.4nm from an Al-Doped TiO<sub>2</sub> Film”, ACS Applied Materials and Interfaces, 6, 21632-21367 (2014)

4. Yeon Woo Yoo, Woojin Jeon, Woongkyu Lee, **Cheol Hyun An**, Seong Keun Kim, and Cheol Seong Hwang, “Structure and Electrical Properties of Al-Doped HfO<sub>2</sub> and ZrO<sub>2</sub> Films Grown via Atomic Layer Deposition on Mo Electrodes”, ACS Applied Materials and Interfaces, 6, 22474-22482 (2014)
5. Woongkyu Lee, Woojin Jeon, **Cheol Hyun An**, Min Jung Chung, Han Joon Kim, Taeyong Eom, Sheby Mary George, Bo Keun Park, Jeong Hwan Han, Chang Gyoung Kim, Taek-Mo Chung, Sang Woon Lee, and Cheol Seong Hwang, “Improved Initial Growth Behavior of SrO and SrTiO<sub>3</sub> Films Grown by Atomic Layer Deposition Using {Sr(demamp)(tmhd)}<sub>2</sub> as Sr-Precursor”, Chemistry of Materials, 27, 3881-3891 (2015)
6. Woojin Jeon, Sang Ho Rha, Woongkyu Lee, **Cheol Hyun An**, Min Jung Chung, Sang Hyun Kim, Cheol Jin Cho, Seong Keun Kim, and Cheol Seong Hwang, “Asymmetry in electrical properties of Al-doped TiO<sub>2</sub> film with respect to bias voltage”, Physica Status Solidi R.R.L., 9, 410-413 (2015)
7. Woongkyu Lee, Sijung Yoo, Woojin Jeon, Yeon Woo Yoo, **Cheol Hyun An**, Min Jung Chung, Han Joon Kim, Sang Woon Lee, and Cheol Seong Hwang, “Reducing the nano-scale defect formation of atomic-layer-deposited SrTiO<sub>3</sub> films by adjusting the cooling rate of the crystallization annealing of the seed layer”, Thin Solid Films, 589, 723-729 (2015)

8. Yu Jin Kim, Hiroyuki Yamada, Taehwan Moon, Young Jae Kwon, **Cheol Hyun An**, Han Joon Kim, Keum Do Kim, Young Hwan Lee, Seung Dam Hyun, Min Hyuk Park, and Cheol Seong Hwang, “Time-Dependent Negative Capacitance Effects in  $\text{Al}_2\text{O}_3/\text{BaTiO}_3$  Bilayers”, *Nano Letters*, 16, 4375-4381 (2016)
9. Cheol Jin Cho, Myoung-Sub Noh, Woo Chul Lee, **Cheol Hyun An**, Chong-Yun Kang, Cheol Seong Hwang, and Seong Keun Kim, “Ta-Doped  $\text{SnO}_2$  as a reduction-resistant oxide electrode for DRAM capacitors”, *Journal of Materials Chemistry C*, 5, 9405-9411 (2017)
10. Woojin Jeon, Youngjin Kim, **Cheol Hyun An**, Cheol Seong Hwang, Patrice Gonon, and Christophe Vallée, “Demonstrating the Ultrathin Metal-Insulator-Metal Diode Using  $\text{TiN}/\text{ZrO}_2\text{-Al}_2\text{O}_3\text{-ZrO}_2$  Stack by Employing  $\text{RuO}_2$  Top Electrode”, *IEEE TRANSACTION ON ELECTRON DEVICES*, 65, 660-666 (2018)
11. Min Jung Chung, Woojin Jeon, **Cheol Hyun An**, Sang Hyeon Kim, Yoon Kyeong Lee, Woongkyu Lee, and Cheol Seong Hwang, “Quantitative Analysis of the Incorporation Behaviors of Sr and Ti Atoms During the Atomic Layer Deposition of  $\text{SrTiO}_3$  Thin Films”, *ACS Applied Materials and Interfaces*, 10, 8836-8844 (2018)
12. Woongkyu Lee, **Cheol Hyun An**, Sijung Yoo, Woojin Jeon, Min Jung Chung, Sang Hyeon Kim, and Cheol Seong Hwang, “Electrical Properties of  $\text{ZrO}_2/\text{Al}_2\text{O}_3/\text{ZrO}_2$ -Based Capacitors with TiN, Ru, and TiN/Ru Top Electrode Materials”, *Physica Status Solidi R.R.L.*, 12, 410-413 (2015)

13. Hyun Jae Lee, Taehwan Moon, **Cheol Hyun An**, and Cheol Seong Hwang, “2D Electron Gas at the Interface of Atomic-Layer-Deposited  $\text{Al}_2\text{O}_3/\text{TiO}_2$  on  $\text{SrTiO}_3$  Single Crystal Substrate”, *Advanced Electronic Materials*, 5, 1, 201800527 (2018)
14. Tae Hyung Park, Young Jae Kwon, Hae Jin Kim, Hyo Cheon Woo, Gil Seop Kim, **Cheol Hyun An**, Yumin Kim, Dae Eun Kwon, and Cheol Seong, “Balancing the Source and Sink of Oxygen Vacancies for the Resistive Switching Memory”, *ACS Applied Materials and Interfaces*, 10, 21445-21450 (2018)
15. **Cheol Hyun An**, Woongkyu Lee, Sang Hyeon Kim, Cheol Jin Cho, Dong-Gun Kim, Dae Seon Kwon, Seong Tak Cho, Soon Hyung Cha, Jun Il Lim, Woojin Jeon, and Cheol Seong Hwang, “Controlling the Electrical Characteristics of  $\text{ZrO}_2/\text{Al}_2\text{O}_3/\text{ZrO}_2$  Capacitors by Adopting a Ru Top Electrode Grown via Atomic Layer Deposition”, *Physica Status Solidi R.R.L.*, 1800454 (2018)
16. Sang Hyeon Kim<sup>†</sup>, Woongkyu Lee<sup>†</sup>, **Cheol Hyun An**, Dae Seon Kwon, Dong-Gun Kim, Soon Hyung Cha, Cheol Seong Hwang, “Effect of Growth Temperature During the Atomic Layer Deposition of the  $\text{SrTiO}_3$  Seed Layer on the Properties of  $\text{RuO}_2/\text{SrTiO}_3/\text{Ru}$  Capacitors for Dynamic Random Access Memory Applications”, *ACS Appl. Mater. Interfaces*, 10, 41544 (2018)

17. Sang Hyeon Kim, Woongkyu Lee, **Cheol Hyun An**, Dong-Gun Kim, Dae Seon Kwon, Seong Tak Cho, Soon Hyung Cha, Jun Il Lim, Cheol Seong Hwang, “Effect of Annealing Temperature of the Seed Layer on the Following Main Layer in the Atomic-Layer-Deposited SrTiO<sub>3</sub> Thin Films”, Phys. Status Solidi RRL, 18005557 (2019)
18. Yu Min Kim, Young Jae Kwon, Jihun Kim, **Cheol Hyun An**, Taegyun Park, Dae Eun Kwon, Hyo Cheon Woo, Hae Jin Kim, Jung Ho Yoon, Cheol Seong Hwang, “Novel Selector-Induced Current-Limiting Effect through Asymmetry Control for High-Density One-Selector-One-Resistor Crossbar Arrays”, Advanced Electronic Materials, 1800806 (2019).
19. Soon Hyung Cha<sup>#</sup>, **Cheol Hyun An**<sup>#</sup>, Seong Tak Cho, Dong-Gun Kim, Dae Seon Kwon, Jun Il Lim, Woojin Jeon, Cheol Seong Hwang, “Scaling the equivalent oxide thickness by employing a TiO<sub>2</sub> thin film on a ZrO<sub>2</sub>-Al<sub>2</sub>O<sub>3</sub>-based dielectric for the further scaling of the dynamic random access memory”, Phys. Status Solidi RRL, 1900282 (2019)

## **2. CONFERENCES**

### **2.1 Domestic**

1. Woojin Jeon, Woongkyu Lee, Yeon Woo Yoo, **Cheol Hyun An**, and Cheol Seong Hwang, “Evaluating the Change in Electrical Conduction Mechanism and Dielectric Properties of TiO<sub>2</sub> Thin-Film by Al Doping”, 제 21회 한국 반도체 학술대회, 한양대학교, 2014년 2월 24일-26일
2. **Cheol Hyun An**, Woojin Jeon, Woongkyu Lee, Yeon Woo Yoo, and Cheol Seong Hwang, “Improving Conformality of SrRuO<sub>3</sub> Film Grown by Combined ALD SrO and CVD RuO<sub>2</sub> or Ru Layers”, 제 21회 한국 반도체 학술대회, 한양대학교, 2014년 2월 24일-26일
3. Woongkyu Lee, Kyung Jean Yoon, Woojin Jeon, Yeon Woo Yoo, **Cheol Hyun An**, and Cheol Seong Hwang, “Bipolar Resistive Switching in Amorphous SrTiO<sub>3</sub> Films Grown by Atomic Layer Deposition”, 제 21회 한국 반도체 학술대회, 한양대학교, 2014년 2월 24일-26일
4. Woojin Jeon, Sijung Yoo, Hyo Kyeom Kim, Woongkyu Lee, **Cheol Hyun An**, Min Jung Chung, and Cheol Seong Hwang, “Evaluating the top electrode material for achieving an equivalent oxide thickness smaller than 0.4nm from an Al-doped TiO<sub>2</sub> film”, 제 22회 한국반도체학술대회, 인천 송도컨벤시아, 2015년 2월 10일-12일
5. **Cheol Hyun An**, Woongkyu Lee, Woojin Jeon, Min Jung Chung, and Cheol Seong Hwang, “ALD-like growth behavior of Ru thin film with RuO<sub>4</sub> precursor”, 제 22회 한국반도체학술대회, 인천 송도컨벤시아, 2015년 2월 10일-12일

6. Min Jung Chung, Woongkyu Lee, Woojin Jeon, **Cheol Hyun An**, and Cheol Seong Hwang, “Comparison of H<sub>2</sub>O and O<sub>3</sub> as oxidant in atomic layer deposition of STO films”, 제 22회 한국반도체학술대회, 인천 송도컨벤시아, 2015년 2월 10일-12일
7. Yu Jin Kim, Min Hyuk Park, Han Joon Kim, Taehwan Moon, Keum Do Kim, **Cheol Hyun An**, Young Hwan Lee, Seung Dam Hyun, and Cheol Seong Hwang, “Interface Charge Controlled Negative Capacitance in Dielectric/Ferroelectric Thin Films”, 제 23회 한국반도체학술대회, 강원도 하이원리조트, 2016년 2월 22일-24일
8. **Cheol Hyun An**, Woongkyu Lee, Min Jung Chung, Sang Hyeon Kim, Lansalot Clement, and Cheol Seong Hwang, “Atomic layer deposition of Ru thin film and its application to a capacitor electrode”, 제 23회 한국반도체학술대회, 강원도 하이원리조트, 2016년 2월 22일-24일
9. Yu Jin Kim, Hyeon woo Park, Hiroyuki Yamada, Taehwan Moon, Young Jae Kwon, **Cheol Hyun An**, Han Joon Kim, Keum Do Kim, Young Hwan Lee, Seung Dam Hyun, Min Hyuk Park, and Cheol Seong Hwang, “Non-hysteretic Negative Capacitance in Al<sub>2</sub>O<sub>3</sub>/BaTiO<sub>3</sub> Bilayers”, 제 24회 한국반도체학술대회, 강원도 대명비발디파크, 2017년 2월 13일-15일

10. Hoju Song, **Cheol Hyun An**, Younjin Jang, Jun Shik Kim, Dae Seon Kwon, Sang Hyeon Kim and Cheol Seong Hwang, “Evaluation of SnO<sub>2</sub> thin films to suppress reduction of RuO<sub>2</sub> electrode during atomic layer deposition of rutile structured TiO<sub>2</sub> films”, 제 24회 한국반도체학술대회, 강원도 대명비발디파크, 2017년 2월 13일-15일
11. **Cheol Hyun An**, Sang Hyeon Kim, Hoju Song, Dae Seon Kwon, and Cheol Seong Hwang, “Growth and electric characteristics of SrRuO<sub>3</sub>/Pt bimetal electrodes for SrTiO<sub>3</sub> dielectric layer”, 제 24회 한국반도체학술대회, 강원도 대명비발디파크, 2017년 2월 13일-15일
12. Dae Seon Kwon, **Cheol Hyun An**, Sang Hyeon Kim, Hoju Song, Seong Tak Cho, Soon Hyung Cha, Taishi Furukawa, Teppei Hayakawa, Kazuhisa Kawano and Cheol Seong Hwang, “Atomic layer deposition of Ru thin films using ‘Rudense’ as Ru precursor”, 제 25회 한국 반도체 학술대회, 강원 하이원리조트, 2018년 2월 5일-7일
13. **Cheol Hyun An**, Sang Hyeon Kim, Dae Seon Kwon, Soon Hyung Cha, Seong Tak Cho and Cheol Seong Hwang, “Atomic layer deposition of Ru thin film with enhanced growth rate on Ta<sub>2</sub>O<sub>5</sub>/Si substrate using RuO<sub>4</sub> precursor and H<sub>2</sub> gas”, 제 25회 한국 반도체 학술대회, 강원 하이원리조트, 2018년 2월 5일-7일
14. Seong Tak Cho, **Cheol Hyun An**, Sang Hyeon Kim, Dong gun Kim, Dae Seon Kwon, Soon Hyung Cha, and Cheol Seong Hwang, “MIM capacitor based on ZrO<sub>2</sub>/Y<sub>2</sub>O<sub>3</sub>/ZrO<sub>2</sub> dielectric for DRAM devices”, 제 25회 한국 반도체 학술대회, 강원 하이원리조트, 2018년 2월 5일-7일

15. Soon Hyung Cha, **Cheol Hyun An**, Sang Hyeon Kim, Dong gun Kim, Dae Seon Kwon, Seong Tak Cho and Cheol Seong Hwang, “MIM capacitor based on  $ZrO_2/Al_2O_3/TiO_2$  dielectric for DRAM devices”, 제 25회 한국 반도체 학술대회, 강원 하이원리조트, 2018년 2월 5일-7일

## **2.2 International**

1. Woojin Jeon, Woongkyu Lee, Yeon Woo Yoo, **Cheol Hyun An** and Cheol Seong Hwang, “Evaluating the Mechanism for Leakage Current Reduction of ALD  $TiO_2$  film by Al-doping”, ALD 2013, San Diego Marriott Marquis & Marina, San Diego, United States, July 28-31 (2013)
2. Woongkyu Lee, Woojin Jeon, Yeon Woo Yoo, **Cheol Hyun An** and Cheol Seong Hwang, “Reducing Micro-defect Formation in Atomic Layer Deposited  $SrTiO_3$  Films during Crystallization Annealing”, ALD 2013, San Diego Marriott Marquis & Marina, San Diego, United States, July 28-31 (2013)
3. Yeon Woo Yoo, Woongkyu Lee, Woojin Jeon, **Cheol Hyun An**, Won Seok Han and Cheol Seong Hwang, “Atomic Layer Deposited  $ZrO_2$  Films on Various Substrates with New Zr Precursor”, ALD 2013, San Diego Marriott Marquis & Marina, San Diego, United States, July 28-31 (2013)

4. **Cheol Hyun An**, Woojin Jeon, Woongkyu Lee, Yeon Woo Yoo and Cheol Seong Hwang, “Improving step coverage of SrRuO<sub>3</sub> film grown by combining ALD SrO and CVD RuO<sub>2</sub> or Ru layers” ALD 2013, San Diego Marriott Marquis & Marina, San Diego, United States, July 28-31 (2013)
5. Woojin Jeon, Woongkyu Lee, Yeon Woo Yoo, **Cheol Hyun An** and Cheol Seong Hwang, “Understanding the variations in leakage conduction mechanism of ALD TiO<sub>2</sub> film by Al-doping”, CECAM-Workshop Functional oxides for emerging technologies, Bremen University, Bremen, Germany, October 14-18 (2013)
6. Woongkyu Lee, Woojin Jeon, Yeon Woo Yoo, **Cheol Hyun An**, Cheol Seong Hwang, “Formation of micro-defects in atomic layer deposited SrTiO<sub>3</sub>films by rapid thermal annealing”, CECAM-Workshop Functional oxides for emerging technologies, Bremen University, Bremen, Germany, October 14-18 (2013)
7. Yeon Woo Yoo, Woongkyu Lee, Woojin Jeon, **Cheol Hyun An**, Cheol Seong Hwang, “Properties of atomic layer deposited ZrO<sub>2</sub> films on various substrates with new Zr precursor”, CECAM-Workshop Functional oxides for emerging technologies, Bremen University, Bremen, Germany, October 14-18 (2013)
8. Woojin Jeon, Woongkyu Lee, Yeon Woo Yoo, **Cheol Hyun An**, and Cheol Seong Hwang, “Initial Growth Behavior of Atomic Layer Deposited TiO<sub>2</sub> Film on RuO<sub>x</sub>(x=0~2) Substrate”, ALD 2014, Granvia Hotel, Kyoto, Japan, June 15-18 (2014)

9. Woongkyu Lee, Woojin Jeon, Yeon Woo Yoo, **Cheol Hyun An**, Min Jung Chung, Taek-Mo Chung, Chang Gyoung Kim, Bo Keun Park, Sheby M. George, and Cheol Seong Hwang, “Atomic Layer Deposition of SrTiO<sub>3</sub> Films with Sr(demamp)(tmhd) as Sr-precursor”, ALD 2014, Granvia Hotel, Kyoto, Japan, June 15-18 (2014)
10. **Cheol Hyun An**, Woojin Jeon, Woongkyu Lee, Yeon Woo Yoo, and Cheol Seong Hwang, “Pursuit of ALD possibility of Ru Thin Film with RuO<sub>4</sub> Precursor”, ALD 2014, Granvia Hotel, Kyoto, Japan, June 15-18 (2014)
11. Woongkyu Lee, Woojin Jeon, Yeon Woo Yoo, **Cheol Hyun An**, Min Jung Chung, Taek-Mo Chung, Bo Keun Park, Sheby M. George, Chang Gyoung Kim, and Cheol Seong Hwang, “Improved Initial Growth Behavior of Atomic Layer Deposited SrTiO<sub>3</sub> Films with [Sr(demamp)(tmhd)]<sub>2</sub> as Sr-precursor”, PacSurf 2014, Hapuna Beach Prince Hotel, Kohala Coast, Hawaii, US, December 7-11 (2014)
12. Woojin Jeon, Woongkyu Lee, **Cheol Hyun An**, Min Jung Chung, Cheol Seong Hwang, “Chemistry of Active Oxygen in RuO<sub>x</sub> and Its Influence on the Atomic Layer Deposition of TiO<sub>2</sub> Films”, PacSurf 2014, Hapuna Beach Prince Hotel, Kohala Coast, Hawaii, US, December 7-11 (2014)
13. Woongkyu Lee, Woojin Jeon, **Cheol Hyun An**, Min Jung Chung and Cheol Seong Hwang, “Capacitor dielectric and electrodes for DRAM with sub-20nm design rule”, ALD 2015, Hilton Hotel, Portland, USA, June 28 - July 1 (2015)

14. Woongkyu Lee, Woojin Jeon, **Cheol Hyun An**, Min Jung Chung and Cheol Seong Hwang, “Atomic Layer Deposition of SrTiO<sub>3</sub> Films with {Sr(demamp)(tmhd)}<sub>2</sub> for DRAM Capacitor Application”, ALD 2015, Hilton Hotel, Portland, USA, June 28 - July 1 (2015)
15. **Cheol Hyun An**, Woojin Jeon, Woongkyu Lee, Min Jung Chung, Lansalot Clement and Cheol Seong Hwang, “ALD growth of Ru thin films and application as a capacitor electrode”, ALD 2015, Hilton Hotel, Portland, USA, June 28 - July 1 (2015)
16. **Cheol Hyun An**, Woongkyu Lee, Min Jung Chung, Sang Hyeon Kim, and Cheol Seong Hwang, “Application of Ru thin film grown by ALD method as a DRAM capacitor electrode material”, 1st International Symposium on Emerging Functional Materials, 송도 컨벤시아, November 4-6 (2015)
17. Sang Hyeon Kim, Woongkyu Lee, **Cheol Hyun An**, Min Jung Chung, Hoju Song and Cheol Seong Hwang, “Atomic layer deposition of SrTiO<sub>3</sub> films with cyclopentadienyl-based precursors for DRAM capacitor application”, ALD 2016, Dublin Ireland, July 24-27 (2016)
18. Hoju Song, **Cheol Hyun An**, Younjin Jang, Sang Hyeon Kim, Min Jung Chung and Cheol Seong Hwang, “Adoption of SnO<sub>2</sub> thin films to prevent reduction RuO<sub>2</sub> to Ru during atomic layer deposition of TiO<sub>2</sub> films for DRAM Capacitor”, ALD 2016, Dublin Ireland, July 24-27 (2016)

19. **Cheol Hyun An**, Woongkyu Lee, Sang Hyeon Kim, Hoju Song and Cheol Seong Hwang, “Growth and electric characteristics of SrRuO<sub>3</sub>/Pt bimetal electrodes for SrTiO<sub>3</sub> dielectric layer”, ALD 2016, Dublin Ireland, July 24-27 (2016)
20. Hyeon Woo Park, Yu Jin Kim, Hiroyuki Itoi, Taehwan Moon, Young Jae Kwon, **Cheol Hyun An**, Han Joon Kim, Keum Do Kim, Young Hwan Lee, Seung Dam Hyun, Min Hyuk Park, Young Bin Lee, and Cheol Seong Hwang, “Study on Hysteresis of Negative Capacitance in Al<sub>2</sub>O<sub>3</sub>/BaTiO<sub>3</sub> Bilayers” Novel high-k Application Workshop 2017, Dresden, Germany, March 9 (2017)
21. Sang Hyeon Kim, Woongkyu Lee, **Cheol Hyun An**, Hoju Song, Dae Seon Kwon, and Cheol Seong Hwang, “Seed layer thickness effects of atomic layer deposited SrTiO<sub>3</sub> thin film”, E-MRS(European materials research society) spring meeting 2017, Strasbourg, France, May 22-26 (2017)
22. Dae Seon Kwon, **Cheol Hyun An**, Sang Hyeon Kim, Hoju Song, Seong Tak Cho, Soon Hyung Cha and Cheol Seong Hwang, “Atomic layer deposition of Ru thin films using new Ru precursor”, E-MRS 2017, Warsaw(Poland), September 18-21 (2017)
23. Sang Hyeon Kim, **Cheol Hyun An**, Dae Seon Kwon, and Cheol Seong Hwang, “The leakage current reduction in atomic layer deposition of Al<sub>2</sub>O<sub>3</sub>-inserted SrTiO<sub>3</sub> films for metal-insulator-metal capacitors” AVS 64th INTERNATIONAL SYMPOSIUM & EXHIBITION, Tampa, FL, October 29 - November 3 (2017)

24. Cheol Jin Cho, Myoung-Sub Noh, Woo Chul Lee, **Cheol Hyun An**, Chong-Yun Kang, Cheol Seong Hwang and Seong Keun Kim, “Development of a reduction-resistant oxide electrode for dynamic random access memory capacitor”, AVS 64th INTERNATIONAL SYMPOSIUM & EXHIBITION, Tampa, FL, October 29 - November 3 (2017)
25. **Cheol Hyun An**, Sang Hyeon Kim, Dae Seon Kwon, Soon Hyung Cha, Sung Tak Cho and Cheol Seong Hwang, “Atomic layer deposition(ALD) of Ru thin film on Ta<sub>2</sub>O<sub>5</sub>/Si substrate using RuO<sub>4</sub> precursor and H<sub>2</sub> gas”, IEEE EDTM 2018, Japan, March 13-16 (2018)
26. Sang Hyeon Kim, **Cheol Hyun An**, Dae Seon Kwon, Soon Hyung Cha, Seong Tak Cho and Cheol Seong Hwang, “Electrical Properties of Al-Doped SrTiO<sub>3</sub> films grown via Atomic Layer Deposition on Ru Electrodes”, 233rd ECS Meeting, Seattle, May 13-17 (2018)
27. Soon Hyung Cha, **Cheol Hyun An**, Sang Hyeon Kim, Dong Gun Kim, Dae Seon Kwon, Seong Tak Cho and Cheol Seong Hwang, “Structure and Electrical Properties of TiO<sub>2</sub>/Al<sub>2</sub>O<sub>3</sub>/ZrO<sub>2</sub> Films Grown via Atomic Layer Deposition on TiN Electrodes”, 233rd ECS Meeting, Seattle, May 13-17 (2018)
28. Seong Tak Cho, **Cheol Hyun An**, Sang Hyeon Kim, Dong Gun Kim, Dae Seon Kwon, Soon Hyung Cha and Cheol Seong Hwang, “Electrical and structural properties of ZrO<sub>2</sub>/Y<sub>2</sub>O<sub>3</sub>/ZrO<sub>2</sub> dielectric film for DRAM capacitor”, 233rd ECS Meeting, Seattle, May 13-17 (2018)

29. **Cheol Hyun An**, Woongkyu Lee, Sang Hyeon Kim, Dae Seon Kwon, Soon Hyung Cha, Seong Tak Cho, and Cheol Seong Hwang, “Atomic Layer Deposition of Ru Metal Thin Film with Substrate-Dependent Growth Behavior on Ta<sub>2</sub>O<sub>5</sub> Substrate”, 18th International Conference on Atomic Layer Deposition, Incheon, South Korea, July 29 - August 1 (2018)
30. Dae Seon Kwon, **Cheol Hyun An**, Sang Hyeon Kim, Hoju Song, Seong Tak Cho, Soon Hyung, Taishi Furukawa, Teppei Hayakawa, Kazuhisa Kawano and Cheol Seong Hwang, “Atomic Layer Deposition of Ru Thin Film using ‘Rudense’ as a Ru precursor and Oxygen gas as a Reactant”, 18th International Conference on Atomic Layer Deposition, Incheon, South Korea, July 29 - August 1 (2018)
31. Sang Hyeon Kim, **Cheol Hyun An**, Dae Seon Kwon, Seong Tak Cho, Soon Hyung Cha and Cheol Seong Hwang, “Electrical Properties of Al-doped SrTiO<sub>3</sub> Films Grown by Atomic Layer Deposition on Ru Electrodes”, 18th International Conference on Atomic Layer Deposition, Incheon, South Korea, July 29 - August 1 (2018)
32. Soon Hyung Cha, **Cheol Hyun An**, Sang Hyeon Kim, Dae Seon Kwon, Seong Tak Cho, and Cheol Seong Hwang, “Atomic Layer Deposition of ZrO<sub>2</sub>/Al<sub>2</sub>O<sub>3</sub>/TiO<sub>2</sub> thin films with high dielectric constant on TiN substrates for DRAM capacitors”, E-MRS 2018, Warsaw (Poland), Sep 17-20 (2018)

### **3. Patents**

1. 황철성, 안철현, “루세늄 박막 증착방법”, 대한민국, 10-1540881-0000, 2015.

08.06

## Abstract (in Korean)

---

현재 대부분의 전자 소자에 사용되는 DRAM 소자는 지속적인 소형화를 요구받고 있는데, 때문에 DRAM 소자의 구성 성분인 커패시터 역시 지속적인 소형화가 필요하다. 그러나 정상적인 DRAM 소자의 작동을 위해 약 25 fF 이상의 커패시턴스를 유지해야 하는데, 소형화에 따른 면적 감소 및 패터닝 기술의 한계 때문에 새로운 재료의 도입을 통한 재료적인 측면에서의 특성 개선이 요구되고 있다.

최근의 여러 연구들에서는 유전물질을 기존의  $\text{HfO}_2$ ,  $\text{ZrO}_2$  계열의 물질보다 높은 유전율을 가지는  $\text{TiO}_2$  혹은  $\text{SrTiO}_3$  를 이용하여 커패시터의 성능을 향상시킨 결과들이 보고되었다. 이런 고유전물질을 이용하여 커패시터의 등가산화막두께를 낮출 수 있었지만, 우수한 성능을 확보하기 위하여서는 적절한 전극 물질의 선택을 통하여 유전막의 결정성 향상 및 낮은 밴드갭 에너지에 필수적으로 수반되는 누설 전류 문제를 해결해야 한다.

$\text{Ru}$ ,  $\text{Ir}$ ,  $\text{Pt}$  등의 다양한 귀금속 계열 물질들이 차세대 DRAM 커패시터의 전극물질로써 각광받고 있는데, 그 중  $\text{Ru}$  은 높은 일함수 ( $\sim 4.7\text{eV}$ ), 낮은 비저항 ( $7\mu\text{ohm-cm}$ ), 높은 화학적 안정성 등의 우수한 특성을 가져 많은 연구가 진행되어 왔다. 대부분의  $\text{Ru}$  박막의 성장 공정은 유기금속 계열 전구체를 이용하였는데, 이런 전구체들은 큰 리간드 크기, 낮은 증기압과 반응성 등의 문제 때문에 DRAM 커패시터에 적용하기에는 어려움이 있다.

때문에 본 연구에서는 반응성과 증기압이 높은 전구체인 사산화루테늄 ( $\text{RuO}_4$ ) 을 전구체로 이용하여  $\text{Ru}$  계열 박막을 성장시키고 커패시터의 전기적 특성을 평가하는 연구를 진행하였다.  $\text{RuO}_4$  전구체를 이용하여  $\text{Ru}$ ,  $\text{RuO}_2$ ,  $\text{SrRuO}_3$  전극물질을 성장시키는 연구가 이미 진행된 바 있으나 이전 연구는 CVD 반응에 기반한

공정이기 때문에, 본 연구에서는 보다 우수한 특성을 위하여 ALD 반응에 기반한 박막의 성장 공정을 개발하였다.

먼저, RuO<sub>4</sub> 전구체와 환원 가스를 이용하여 Ru 금속 박막을 ALD 공정으로 성장시키는 공정을 연구하였다. 전구체의 열분해를 막기 위하여 기존에 보고된 CVD 공정보다 낮은 공정 온도에서 진행하였다. Ta<sub>2</sub>O<sub>5</sub>, ZrO<sub>2</sub>, TiO<sub>2</sub> 의 다양한 기판에서 Ru 금속막을 성장시킨 결과, ZrO<sub>2</sub> 와 TiO<sub>2</sub> 유전막 위에서는 일반적인 ALD 성장 거동을 나타낸 반면 Ta<sub>2</sub>O<sub>5</sub> 유전막 위에서는 반응 가스 주입 시간에 따라 2 단계의 자기 제한적 성장 거동을 보인다. 각 단계에서 성장시킨 박막의 물리적, 화학적 특성을 평가한 결과 RuO<sub>2</sub> 상의 형성 없이 순수한 Ru 금속을 성장시켰음을 확인했다. 추가적인 분석을 통하여, 이러한 특이 성장 거동을 설명할 수 있는 Ta<sub>2</sub>O<sub>5</sub> 기판 물질의 환원 및 확산에 기반한 메커니즘임을 제시하였다. 성장 거동과 무관하게 루테튬 박막은 낮은 표면 거칠기와 낮은 비저항, 낮은 불순물 농도를 가지며 우수한 단차피복성을 보인다. ZrO<sub>2</sub> 와 TiO<sub>2</sub> 기판 위에서도 Ru 금속막은 Ta<sub>2</sub>O<sub>5</sub> 기판 위에서의와 동일하게 우수한 특성을 보였다.

Ru 전극막은 높은 일함수로 인하여 유전막의 누설 전류 특성을 개선할 것으로 기대되기 때문에, 이를 상부전극으로 적용한 커패시터의 전기적 특성 개선을 확인하였다. 유전막으로는 ZAZ, 하부 전극으로는 TiN 물질을 이용하였고, 대조군으로써 TiN 상부 전극을 스퍼터 공정으로 성장시켰다. Ru 전극막을 ALD 공정으로 성장시키기 때문에 증착 이후 패터닝 공정이 요구되며, ALD 챔버 내에서 O<sub>3</sub> 를 주입하여 Ru 금속막을 에칭하였다. Ru/ZAZ/TiN 커패시터와 TiN/ZAZ/TiN 커패시터의 전기적 특성을 비교한 결과, 확연한 누설 전류 특성의 감소를 보였다. 누설전류 특성 개선에 의해 물리적 두께를 더 낮출 수 있어, 최종적으로 DRAM 커패시터에 요구되는 누설전류 수준인 10<sup>-7</sup> A/cm<sup>2</sup> 에서 등가산화막 두께를 75% 수준으로 낮추었다. 커패시터의 누설 전류 메커니즘을 분석한 결과, Ru 금속 자체의 높은 일함수로 인한 누설전류 개선뿐만 아니라 Ru 상부 전극막의 패터닝

공정에서 주입된 O 에 의하여 ZAZ 유전막 내의 oxygen vacancy 의 농도가 줄어들어 전체 누설전류 특성의 개선이 나타났음을 확인하였다.

마지막으로 SrRuO<sub>3</sub> 전극막의 증착 공정 변화를 통해 단차피복성을 개선하는 연구를 진행하였다. 기존에 보고된 SrRuO<sub>3</sub> 의 증착 공정은 ALD SrO 박막과 CVD RuO<sub>2</sub> 박막을 결합하는 방식인데, 이 때 나타나는 SrO 박막의 과잉 성장으로 인하여 단차피복성이 열화되는 문제가 있었다. 때문에 과잉 성장의 원인인 RuO<sub>2</sub> 층에서의 산소 흡수를 막기 위하여, RuO<sub>2</sub> 증착 이후에 환원 가스 주입 단계를 추가하여 SrO 박막이 흡수할 수 있는 산소의 양을 제어하였다. 최종적으로 박막 특성의 열화 없이 10:1 의 종횡비를 가지는 구조에서 단차피복성을 95% 수준으로 향상시켰으며 박막의 표면 거칠기도 기존 공정 대비 개선된 결과를 보였다.

---

**주요어:** 루테늄, 스트론튬 루테테이트, 루테늄 사산화물, DRAM, 원자층 증착법, 커패시터

**학번:** 2013-22478

안 철 현